NORTHWESTERN UNIVERSITY

Control of Soft Active Materials

A DISSERTATION

SUBMITTED TO THE GRADUATE SCHOOL
IN PARTIAL FULFILLMENT OF THE REQUIREMENTS

for the degree

DOCTOR OF PHILOSOPHY

Physics and Astronomy

By

Aaveg Aggarwal

EVANSTON, ILLINOIS

August 2022

ABSTRACT

Since the dawn of mankind, humans have used materials and tools to dominate the world. As our understanding of the fields physics, chemistry and engineering is growing, we are able to artificially create advanced materials with engineered responses. Next step would be to create ' smart' or intelligent materials capable of sensing their environment and change their material properties in response, similar to biological matter. Active matter systems and materials functionalized with active components can lead to such responsive materials. The work presented in this thesis focuses on theoretical and computational modeling of such active soft matter systems. Specifically, we studied and helped design responsive hydrogel systems capable of shape transformations and locomotion in response to various external fields and stimuli. We also studied the migration of ferrofluid droplets in external magnetic fields which exist in a liquid phase as opposed to the hydrogels which are elastic. We developed continuum models to study each system and solved these models using the finite element method. We worked closely with experimentalists to verify our models and theories. The work developed here will help better understand these active materials and will aid in the development of newer active soft matter systems.

ACKNOWLEDGEMENTS

First and foremost, I would like to express my deepest gratitude to my advisor Prof. Monica Olvera de la Cruz for her constant support and guidance. She is not only a great mentor but also a great human being. I sincerely thank her for patiently helping me find the research topics I truly enjoyed. When most graduate students suffer from 'imposter syndrome', her constant encouragements and compliments really helped with my self-confidence and it not only helped me become a better researcher but a better person in general. I remember seeing her for the first time in her office as a dejected fourth year graduate student looking to switch research groups. I can't thank her enough for believing in me and giving me an opportunity to continue my PhD. I would not have been able to finish this journey without her help. I would also like to thank my committee members Prof. John Marko and Prof. Michelle Driscoll, for taking the time out of their busy schedules to review my work and this thesis. Their expert knowledge is crucial for the fulfilment of the work presented here.

I am grateful to all the group members for creating a healthy and welcoming environment where we could freely talk to each other about our research and personal lives. I thank Dr. Felipe Jimenez Angeles for being an amazing office-mate. Our discussions in the office were always thought provoking and insightful. I was also fortunate enough to be able to collaborate with some of our brilliant group members and I would like to thank Dr. Hang Yuan, Dr. Eleftherios Kirkinis, Dr. Daniel Matoz-Fernandez, Dr. Siyu Li and Dr. Shuangping Liu for their valuable contribution to my research. I would also like to thank my collaborators Dr. Chuang Li, Dr. Garrett C. Lau, Doruk Cezan and Prof. Liam Palmer in Prof. Samuel Stupp's group for conducting the experimental work presented in this thesis.

Last but not the least, I would like to thank my family for their unconditional love and support.

TABLE OF CONTENTS

LIST OF FIGURES

LIST OF TABLES

CHAPTER 1

INTRODUCTION

1.1 Introduction and Motivation

The understanding of materials has played a very important role in the advancement of our society and culture. Materials have shaped our civilizations to such a large extent that historians have named entire periods of human history after the predominantly used materials i.e. the stone age, the bronze age and the iron age. Though historically, humans have always used materials to interact with the world, but our knowledge of them was largely empirical. However, our understanding of physics and chemistry has lead to a systematic study of the interdisciplinary field of material science.

In modern times, in the 19th and 20th century, the traditional 'hard' materials such as metals and semiconductors paved the way for industrial revolution and automation. Soon, we started developing newer and better materials that could replace traditional materials while being light weighted and easier to process. This lead to the focus on *soft matter*. The 'hardness' and 'softness' refers to a material's response to external stimuli. Unlike hard matter, soft materials are more compliant and easily deform under external stresses. This is because soft materials are made of large molecules or aggregates which have weak intermolecular interactions. Due to the nature of their composition, soft materials exhibit large morphological changes to external stimuli. Soft materials include liquids, colloids, polymers, liquid crystals, gels, etc. These materials have great industrial applications and have also become an important part of our daily lives.

The behavioral properties of soft materials can be altered by suitably functionalizing them with

active constituents that consume energy and dynamically alter their macroscopic responses. This energy can be provided by means of external fields and forces. In this work, we explored such active matter systems that undergo shape transformations and locomotion in response to various external stimuli. We studied two classes of soft materials, namely functionalized hydrogels and ferrofluids. Hydrogels are elastic materials made up of three-dimensional polymer networks permeated by solvent molecules. Hydrogels can drastically change their volume by absorbing large amounts of solvent. Stimuli responsive hydrogels have been shown to swell/shrink in response to cues such as light [1]–[3], heat [4], magnetic fields [5], [6], changes in chemistry [7], [8], etc. Ferrofluids on the other hand, are a colloidal suspension of magnetic nanoparticles that respond to external magnetic fields.

In this work, we analyzed the aforementioned active matter systems by means of theoretical modeling. We constructed continuum models to predict the behavior of these systems in the presence of external fields and solved them using the finite element method. Theoretical frameworks developed here will help better understand these active systems and will aid in the development of newer materials.

1.2 Mathematical background

Some of the basic theory in continuum mechanics is discussed here. The concepts, terminologies and mathematical framework introduced here will be used to analyze the active matter systems studied in the later chapters.

1.2.1 Coordinate frames

In order to describe the mechanical properties such as motion and deformation of a continuum body, we need a coordinate system. Two different coordinate frames are commonly employed to
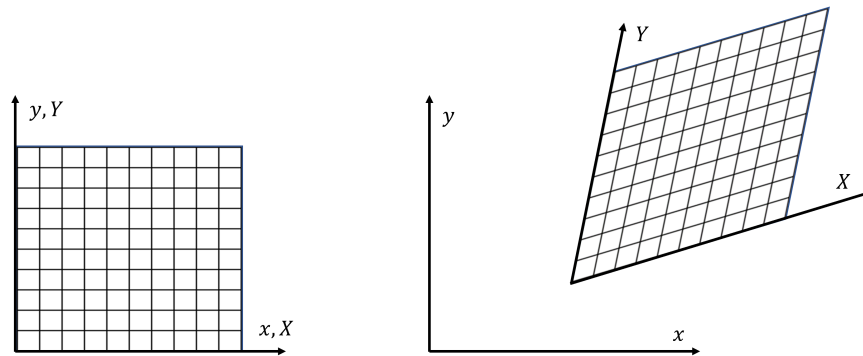
Figure 1.1: Schematic representation of the spatial and material coordinate frames denoted by (x, y and z) and (X, Y and Z) respectively.

describe continuum bodies and are listed as follows [9]:

- **Spatial coordinate frame** This is the lab frame which is fixed as the continuum body moves through the physical space. Position coordinates in the spatial frame are usually denoted by lower case letters i.e. x, y and z. The spatial coordinate frame is also known as the Eularian frame and the corresponding mechanical description of a continuum body is called the Eularian description. See figure 1.1.

- **Material coordinate frame** This is a coordinate frame that is attached to the continuum body and moves/deforms along with the body. As the material deforms, the position coordinates of the body in the material frame stay the same and usually denoted by upper case letters i.e. X, Y and Z. The material coordinate frame is also known as the Lagrangian frame or reference frame and the corresponding mechanical description of a continuum body is called the Lagrangian description. See figure 1.1.

Before the continuum body starts deforming the spatial and the material frames coincide in the

initial state. As the body deforms, a point particle on the surface of the body moves and follows a path given by

$$\mathbf{x} = \mathbf{x}(\boldsymbol{X}, t) \tag{1.1}$$

Here, $\mathbf{x}$ is the spatial coordinate and $\boldsymbol{X}$ is the material coordinate of the particle. For a simplified case where the $\mathbf{x}$ and $\boldsymbol{X}$ are measured with respect to the same coordinate system (as shown in fig. 1.2), we can describe the position $\mathbf{x}$ of the particle as

$$\mathbf{x} = \boldsymbol{X} + \boldsymbol{u}(\boldsymbol{X}, t) \tag{1.2}$$

where, $\boldsymbol{u}$ is the net displacement of the particle at reference position $\boldsymbol{X}$ at time t. An infinitesimal line element, $d\boldsymbol{X}$ in the reference frame, is mapped to the corresponding deformed line element $d\mathbf{x}$ by

$$d\mathbf{x} = \frac{\partial \mathbf{x}}{\partial \boldsymbol{X}} d\boldsymbol{X} = \boldsymbol{F} d\boldsymbol{X} \tag{1.3}$$

where $\boldsymbol{F}$ is called the *deformation gradient tensor* and can also be defined in terms of the displacement $\boldsymbol{u}$ as

$$\boldsymbol{F} = \frac{\partial \mathbf{x}}{\partial \boldsymbol{X}} = \boldsymbol{\nabla}_X \boldsymbol{u} + \boldsymbol{I} \tag{1.4}$$

where $\boldsymbol{\nabla}_X$ is the gradient with respect to the material coordinates i.e.

$$\boldsymbol{\nabla}_X = \left[\frac{\partial}{\partial X}, \frac{\partial}{\partial Y}, \frac{\partial}{\partial Z} \right] \tag{1.5}$$
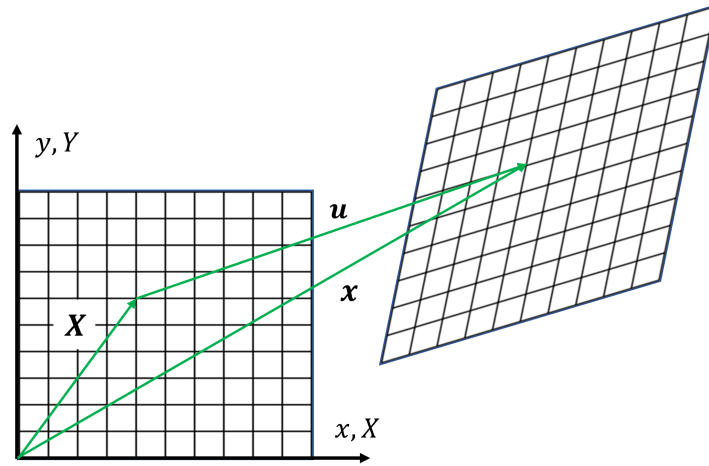
Figure 1.2: Schematic representation of the deformation of a continuum body.

1.2.2 Strain

The deformation gradient tensor $\boldsymbol{F}$ is an important quantity as it contains all the information of straining and rotation. It is sometimes required to only look at the deformation of a body ignoring the overall rotation, for example, the free energy of an elastic body is invariant under a rotation. Therefore, we can use the polar decomposition of $\boldsymbol{F}$ to separate the contributions of rotation and stretch. The right polar decomposition of $\boldsymbol{F}$ can be defined as

$$\mathbf{F} = \mathbf{RU} \tag{1.6}$$

where $\boldsymbol{R}$ is an orthogonal tensor ($det(\mathbf{R}) = 1$ and $\mathbf{R}^T = \mathbf{R}^{-1}$) and $\mathbf{U}$ is the stretch tensor given in the material frame. The tensor $\mathbf{R}$ describes the rotation of the body and $\mathbf{U}$ contains the information about stretch. To calculate the length of the line element $d\mathbf{x}$, we take [9]

$$ds^2 = d\mathbf{x} \cdot d\mathbf{x} = d\mathbf{X} \cdot (\mathbf{F}^T \mathbf{F}) \cdot d\mathbf{X} \tag{1.7}$$

Here we can define the *right Cauchy-Green deformation tensor* $\mathbf{C}$ as

$$\mathbf{C} = \mathbf{F}^T \mathbf{F} \quad \left(= \mathbf{U}^T \mathbf{R}^T \mathbf{R} \mathbf{U} = \mathbf{U}^T \mathbf{U}\right) \tag{1.8}$$

We can see here that the right Cauchy-Green tensor $\mathbf{C}$ does not depend on any rigid body motion i.e. rotations and translations as it only depends on the stretch tensor $\mathbf{U}$. Also from eq. 1.7 if $\mathbf{C} = \mathbf{F}^T \mathbf{F} = \mathbf{I}$, we get $ds^2 = dS^2$ where $dS^2 = d\mathbf{X} \cdot d\mathbf{X}$. Therefore, $\mathbf{C} = \mathbf{I}$ corresponds to a rigid body motion. Expanding $\mathbf{C}$ in terms of the displacement $\mathbf{u}$

$$\mathbf{C} = \mathbf{F}^T \mathbf{F} = \left(\mathbf{I} + \boldsymbol{\nabla}_{\mathbf{X}} \mathbf{u}\right)^T \left(\mathbf{I} + \boldsymbol{\nabla}_{\mathbf{X}} \mathbf{u}\right) = \mathbf{I} + \boldsymbol{\nabla}_{\mathbf{X}} \mathbf{u} + \left(\boldsymbol{\nabla}_{\mathbf{X}} \mathbf{u}\right)^T + \left(\boldsymbol{\nabla}_{\mathbf{X}} \mathbf{u}\right)^T \left(\boldsymbol{\nabla}_{\mathbf{X}} \mathbf{u}\right) \tag{1.9}$$

Here, we define the Green-Lagrange *finite* strain tensor $\mathbf{E}$ as

$$\mathbf{E} = \frac{1}{2} \left[\mathbf{C} - \mathbf{I}\right] = \frac{1}{2} \left[\boldsymbol{\nabla}_{\mathbf{X}} \mathbf{u} + \left(\boldsymbol{\nabla}_{\mathbf{X}} \mathbf{u}\right)^T + \left(\boldsymbol{\nabla}_{\mathbf{X}} \mathbf{u}\right)^T \left(\boldsymbol{\nabla}_{\mathbf{X}} \mathbf{u}\right)\right] \tag{1.10}$$

In index notation,

$$E_{ij} = \frac{1}{2} \left[\frac{\partial u_i}{\partial X_j} + \frac{\partial u_j}{\partial X_i} + \frac{\partial u_k}{\partial X_i} \frac{\partial u_k}{\partial X_j}\right] \tag{1.11}$$

For infinitesimal strains, we can ignore the second order term i.e. $\left(\boldsymbol{\nabla}_{\mathbf{X}} \mathbf{u}\right)^T \left(\boldsymbol{\nabla}_{\mathbf{X}} \mathbf{u}\right)$. Therefore, the infinitesimal strain tensor $\boldsymbol{\epsilon}$ commonly known as the engineering strain tensor is given by

$$\epsilon_{ij} = \frac{1}{2} \left[\frac{\partial u_i}{\partial X_j} + \frac{\partial u_j}{\partial X_i}\right] \tag{1.12}$$

1.2.3 Stresses

Stress is used to describe forces acting on a body and is defined as force per unit area. However, depending on the coordinate frame the quantities are measured, we can have different measures of stress on a body. The most commonly used measure of stress is the Cauchy stress also know as the true stress. Cauchy stress, σ measures the force acting on a continuum body per unit area measured in the deformed configuration or spatial frame. σ is also a symmetric tensor and it is a consequence conservation of angular momentum. However the symmetry of the stress tensor is no longer valid if there exists body moments per unit volume due to external or active stresses [9].

Other commonly used measures of stress on a continuum body are First and Second Piola-Kirchhoff stress tensors and are explained below:

- *First Piola-Kirchhoff stress tensor* (**P**) - is a measure of stress which relates the forces measured in the spatial frame to the areas measure in the material frame. Similar to the deformation gradient tensor **F**, **P** is a two-point tensor.

- *Second Piola-Kirchhoff stress tensor* (**S**) is a measure of stress where both the forces and areas are measured in the material frame. Just like the Cauchy stress tensor σ, the second Piola-Kirchhoff stress tensor, **S** is also symmetric.

The above mentioned three stress tensor relate to each other via the following transformations:

$$\mathbf{S} = \mathbf{F}^{-1}\mathbf{P} \tag{1.13}$$

$$\boldsymbol{\sigma} = J^{-1}\mathbf{P}\mathbf{F}^T = J^{-1}\mathbf{F}\mathbf{S}\mathbf{F}^T \tag{1.14}$$

where J is the determinant of the deformation gradient tensor **F** i.e. $J = det(\mathbf{F})$.

1.2.4 Equation of Motion

Given the internal stresses and external forces on a body, we can write down the equations of motion using the force balance equation i.e. Newton's second law of motion. For an arbitrary volume in undeformed reference frame V_0, the momentum conservation can be expressed in the integral form as:

$$\frac{\partial}{\partial t} \int_{V_0} \rho_0 \frac{\partial \mathbf{u}}{\partial t} dV = \int_{V_0} \boldsymbol{f_V} dV + \int_{\partial V_0} \boldsymbol{T} dA \tag{1.15}$$

where, ρ_0 is the mass density with respect to the volume in reference frame; $\boldsymbol{f_V}$ is the volume force acting on the body such as gravity per unit volume in reference frame; and $\boldsymbol{T}$ represents the traction forces acting on the surface of the body.

Taking $\boldsymbol{N}$ to be the surface normal in reference frame and using the definition of first Piola-Kirchhoff stress tensor $\mathbf{P}$, we can write

$$\int_{\partial V_0} T_i dA = \int_{\partial V_0} P_{iJ} N_J dA = \int_{V_0} \frac{P_{iJ}}{\partial X_J} dV \tag{1.16}$$

Plugging this back into eq. 1.15, we can write the equation of motion for our continuum body as follows:

$$\rho_0 \frac{\partial^2 \mathbf{u}}{\partial t^2} = \boldsymbol{f_V} + \boldsymbol{\nabla_X} \cdot \mathbf{P}^T \tag{1.17}$$

Similarly we can write the equation of motion with respect to volumes in spatial frame as

$$\rho \frac{\partial^2 \mathbf{u}}{\partial t^2} = \boldsymbol{f_v} + \boldsymbol{\nabla_x} \cdot \boldsymbol{\sigma}^T \tag{1.18}$$

where $\boldsymbol{f_v}$ is the volume force per unit volume in spatial frame and the operator $\boldsymbol{\nabla_x}$ is with

respect to the spatial coordinates **x**.

1.2.5 Material Models

The equations of motion are derived from Newton's second law and are true for all continuous media. However, they alone are not complete set of equations as they don't describe the properties of the material under study, for example, under an external load, the response of steel would be different from that of rubber. Therefore, in order to describe these material properties we need a *constitutive equation* that defines a relation between the stress and the strain i.e. $\boldsymbol{\sigma} = \boldsymbol{\sigma}(\boldsymbol{\epsilon})$. These constitutive equations/relations are material specific and fully describe their behaviour in response to external loads. These are also referred to as material models or constitutive models.

In this thesis, we will focus on the *elastic* properties of materials. Elasticity is the property due to which a material deforms under a distorting force and goes back to its original shape once the force is removed. Such material deformations are known as elastic deformations. Here, we will discuss two difference classes of material models used to describe elastic deformations in solids.

Linearly elastic material model

Most elastic materials under a small deformation exhibit linear elasticity. The stress-strain constitutive relation for a linearly elastic materials is known as the *Hooke's Law*. Hooke's Law is stated as

$$\sigma_{ij} = C_{ijkl}\epsilon_{kl} \tag{1.19}$$

where, C_{ijkl} is the 4th order elasticity tensor. For homogeneous and isotropic material, the elasticity tensor reduces to two independent parameters i.e. the bulk modulus K and the shear modulus

μ and can be written as

$$C_{ijkl} = K\delta_{ij}\delta_{kl} + \mu \left(\delta_{ik}\delta_{jl} + \delta_{il}\delta_{jk} - \frac{2}{3}\delta_{ij}\delta_{kl} \right) \tag{1.20}$$

Therefore, the constitutive relation eq. 1.19 can be written as [9], [10]

$$\sigma_{ij} = \lambda\delta_{ij}\epsilon_{kk} + 2\mu\epsilon_{ij} \tag{1.21}$$

where, λ and μ are known as Lamé parameters and the first Lamé parameter relates to the bulk modulus K via the relation $K = \lambda + \frac{2}{3}\mu$. The strain tensor ϵ used here is the infinitesimal strain tensor (eq. 1.12).

Hyperelastic material model

Unlike Hooke's law, the stress-strain constitutive relation for a hyperelastic material may not necessarily be linear. For many materials, the linear Hooke's law does not accurately predict their behaviour and also as the strain on the material grows, they start deviating from a linear stress strain relation. In order to accurately model such materials and strains, we need hyperelastic material models. Their constitutive equation is derived from a strain energy density function W_s which is a function of the deformation gradient tensor i.e. $W_s = W_s(\mathbf{F})$. With the strain energy density defined, we can calculate the stress on the system using

$$\mathbf{P} = \frac{\partial W(\mathbf{F})}{\partial \mathbf{F}} \quad \text{or} \quad P_{iJ} = \frac{\partial W}{\partial F_{iJ}} \tag{1.22}$$

We can also define the 1st Piola-Kirchhoff stress tensor $\mathbf{P}$ in terms of the Green-Lagrange strain tensor $\mathbf{E}$ as

$$\mathbf{P} = \mathbf{F} \cdot \frac{\partial W}{\partial \mathbf{E}} \quad \text{or} \quad P_{iJ} = F_{iK} \frac{\partial W}{\partial E_{KJ}} \tag{1.23}$$

1.3 Polymer Hydrogel Model

The free energy of a polymeric hydrogel come from two processes: elasticity of the polymer network and the mixing of the polymer mesh with the surrounding solvent. The free energy of the hydrogel is therefore assumed to be [11]–[13]:

$$U_{gel} = U_{elastic} + U_{mix} \tag{1.24}$$

where, the elastic energy density $U_{elastic}$ is given by the affine network model

$$U_{elastic} = \frac{1}{2} \frac{k_B T}{v_m N_x} \left(\sum_i \lambda_i^2 - 3 \right) \tag{1.25}$$

Here v_m is the volume of the gel monomer; N_x is the average number of segments between two crosslinking junctions of the polymer network i.e. larger the N_x, softer the gel; and λ_is are the principal stretches of the system;

The mixing energy U_{mix} is a function of the polymer volume fraction ϕ only. The polymers of the hydrogel when not crosslinked form a solution with the solvent molecules, and the free energy density of mixing of this polymer-solvent solution is given by the Flory Huggins model:

$$U_{mix} = \frac{k_B T}{v_m} \left[\left(\frac{1-\phi}{\phi} \right) ln(1-\phi) + \chi(1-\phi) \right] \tag{1.26}$$

where, χ is a temperature dependent parameter $(\chi(T))$ that describes the interaction between the gel monomers and solvent molecules. If χ increases, the solvent molecules are expelled from the gel causing the gel to shrink and if χ decrease the the solvent molecules are absorbed by the gel causing the gel to swell.

Note: The expressions for $U_{elastic}$ (eq. 1.25) and U_{mix} (eq. 1.26) represent the energy values per unit volume in the *reference frame*.

A hydrogel in equilibrium with the surrounding solvent will satisfy the no stress condition i.e. $\partial U_{gel}/\partial \phi = 0$ [12]. Also, for an isotropic free swelling gel, λ_is will all be equal and will satisfy $\lambda_1 = \lambda_2 = \lambda_3 = \phi^{-1/3}$. The equilibrium condition for an isotropically freely swelling gel can be written as:

$$\frac{\partial}{\partial \phi}\left[\frac{3}{2N_x}\phi^{-2/3} + \left(\frac{1-\phi}{\phi}\right)ln(1-\phi) + \chi(1-\phi)\right]\bigg|_{\phi=\phi_{eq}} = 0 \qquad (1.27)$$

Equation 1.27 can be evaluated to calculate an expression for χ in terms of the equilibrium polymer volume fraction ϕ_{eq} i.e.

$$\chi = -\frac{\phi_{eq}^{-5/3}}{N_x} - \frac{log\,(1-\phi_{eq})}{\phi_{eq}^2} - \frac{1}{\phi_{eq}} \qquad (1.28)$$

1.4 Finite Element Implementation

1.4.1 The reference state

In solving the hyperelastic model of the hydrogel numerically, the choice of a suitable reference state becomes critical. The term $U_{elastic}$ (eq. 1.25) assumes the reference state to be a dry polymer state with no solvent i.e. $\lambda_i = 1$ in the dry state for all i. However, the dry polymer state can cause infinities in the numerical implementation of the mixing energy U_{mix} (eq. 1.26). This is because
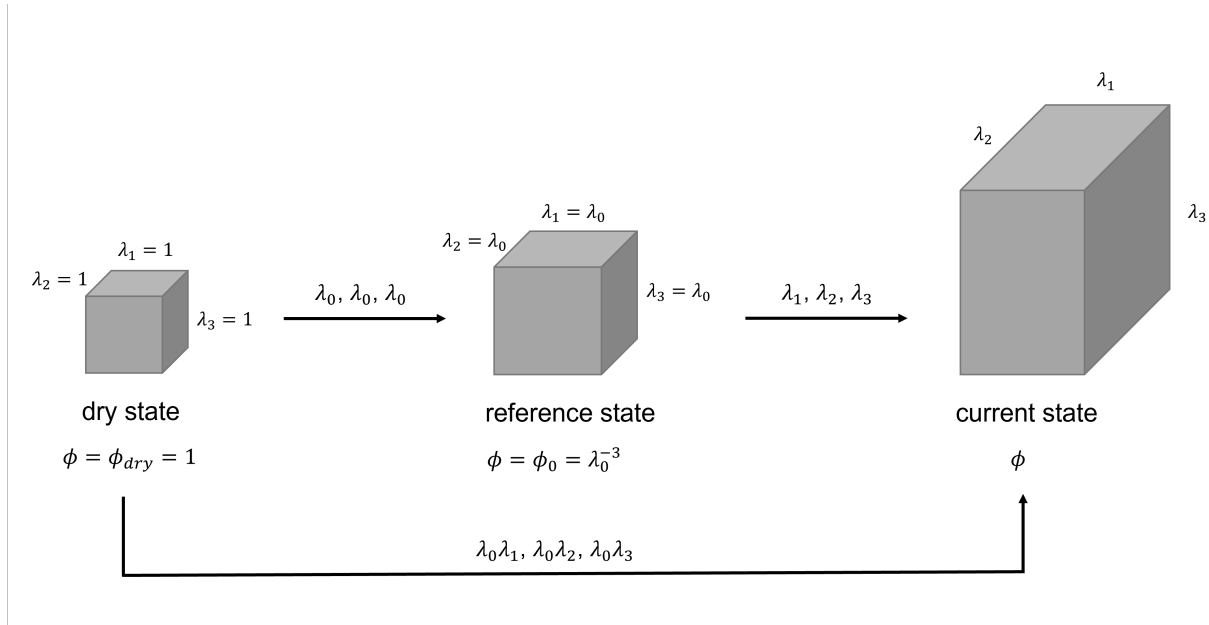
Figure 1.3: Illustration of the reference state used for numerical calculations

of the presence of the $log(1 - \phi)$ term in the expression as $\phi = 1$ for the dry state. In order to circumvent this problem, we have to choose a reference state that is not dry and therefore rewrite eqs. 1.25 and 1.26 with respect to a new reference state for the numerical implementation of the hydrogel.

One option is to choose an isotropically swollen gel state with $\lambda_1 = \lambda_2 = \lambda_3 = \lambda_0 = \phi_0^{-1/3}$ where ϕ_0 is the polymer volume fraction of the hydrogel in the reference state ($\phi_0 < 1$). Therefore, for the purpose of the numerical simulations, the stretches λ_1, λ_2 and λ_3 in the current state are written with respect to this isotropically swollen reference state. This concept can be visualized with the help of fig. 1.3. The total stretch in the current state is $\lambda_0\lambda_1$, $\lambda_0\lambda_2$ and $\lambda_0\lambda_3$ with respect to the dry state. Additionally, since $U_{elastic}$ and U_{mix} are energy '*densities*', we require

$$\int_V U_{dry}dV_{dry} = \int_V U_{ref}dV_{ref} \tag{1.29}$$

where U_{dry} and U_{ref} are any arbitrary energy '*densities*' written with respect to volume in dry state (V_{dry}) and reference state (V_{ref}) respectively. Since $dV_{dry} = \phi_0 dV_{ref}$ (by definition), we have $U_{ref} = \phi_0 U_{dry}$. Therefore, using eq. 1.25 for the elastic energy density and rewriting it with respect to the new reference state, we get:

$$
\begin{aligned}
U_{elastic} &= \frac{1}{2}\frac{k_B T}{v_m N_x}\phi_0 \left(\sum_i \lambda_0^2 \lambda_i^2 - 3 \right) \\
&= \frac{1}{2}\frac{k_B T}{v_m N_x}\phi_0 \left(\phi_0^{-2/3} \sum_i \lambda_i^2 - 3 \right)
\end{aligned}
\tag{1.30}
$$

Using this equation (eq. 1.30) will ensure correct calculations of the elastic energy while writing the stretches with respect the reference state. Similarly, now we have to rewrite the mixing energy U_{mix}. First, we see that the polymer volume fraction $\phi_{dry-to-current} = \frac{1}{\lambda_0^3 \lambda_1 \lambda_2 \lambda_3} = \phi_0 \phi$. Therefore, using equation 1.26, we can write the mixing free energy to be:

$$
U_{mix} = \frac{k_B T}{v_m}\phi_0 \left[\left(\frac{1 - \phi_0 \phi}{\phi_0 \phi} \right) ln(1 - \phi_0 \phi) + \chi(1 - \phi_0 \phi) \right]
\tag{1.31}
$$

Here you can see that we no longer run into the the problem of getting infinities from the log term in the mixing energy U_{mix}. This is because when $\phi = 1$, our current state coincides with the reference state instead of the dry state and we get finite results for both the elastic energy and the mixing energy.

Note: In order to perform numerical calculations, a similar treatment of changing the reference frames should be done for any additional terms that one may add to the hyperelastic model of the hydrogel (discussed in later chapters).

The hydrogel model is then solved using a commercial finite element software COMSOL [14]. We use COMSOL's solid mechanics module which has an option to create user-defined hyperelastic material models. [15]

1.5 Outline

The mathematical framework of continuum mechanics introduced in the previous section will act as the foundation for all the work discussed later in this thesis. The research projects undertaken are listed as individual chapters starting from chapter 2 where we developed a material model used to describe a photo-responsive hydrogel system. Using this material we designed multi-component hydrogel sheets that fold into origami inspired patterns in the presence of light.

In chapter 3, we discuss the model we developed for understanding the dynamics of pattern formation in a BZ-hydrogel undergoing chemically induced mechanical oscillations.

In chapter 4, we constructed a magnetically driven soft robotic system capable of walking underwater. The walking behavior of the robot could be tuned with the help of an external light source. Here we discuss the continuum model developed to understand the motion of such a robotic system. We also provide synthesis details of the robot's material as it is critical for the development of the its constitutive model.

In chapter 5, we constructed another hydrogel robot that can be actuated using light and magnetic fields. However, this robot is capable of swimming underwater in addition to just walking. We modeled the interaction of the swimmer with the surrounding fluid to demonstrate the swimming behavior of the robot. Due to the unique chemical nature of the developed material, the constructed swimming robots exhibit phototactic properties.

In chapter 6, we analyze an active matter system that is in a liquid state as opposed to the solid hydrogel systems analyzed in the other chapters. In this work we study the motion of a ferrofluid droplet moving under the influence of a rotating magnetic field.

Lastly, chapter 7 will conclude this thesis by summarizing the work presented here.

CHAPTER 2

CONTROLLING THE SHAPE MORPHOLOGY OF ORIGAMI-INSPIRED

PHOTORESPONSIVE HYDROGELS

2.1 Abstract

The concept of origami has influenced the development of responsive materials that can mimic complex functions performed by living organisms. An ultimate goal is to discover and design soft materials that can be remotely actuated into diverse structures. To achieve this goal, we design and synthesize here a light-responsive spiropyran hydrogel system that can display dynamic shape changes upon irradiation with local light. We use a continuum polymer model to analyze the behavior of the constructed photoactive hydrogel, which is in good agreement with the experimental results. We explore different buckling modalities and patterns in a different range of parameters. The synthesis and fabrication of these materials demonstrate that the theoretical model can be used to drive the development of responsive photoactive systems.

2.2 Introduction

Many biological species can alter their shape in response to changes in the external environment. These remarkable properties evolved to allow species to better survive in nature. Synthetic active materials with similar shape-morphing capabilities can prove to be extremely useful in soft

---

This chapter is primarily based on the published work [16] of Aaveg Aggarwal, Chuang Li, Samuel I. Stupp and Monica Olvera de la Cruz, with extended and modified details. Experimental work was conducted by Dr. Li and Prof. Stupp.

robotics [8] [6] [5], biosensors [17], and drug delivery [18] [19] applications to name a few. Stimuli-responsive materials that deform in response to environmental cues such as chemical [8] [7], thermal [4], light [6] [1] [2] [20], and magnetic fields [6] [21] [5], have become exemplary materials for such endeavours. Light-responsive materials are of particular interest as light can be delivered remotely and precisely for local actuation of the material. Recent examples of light-responsive materials include polymer films containing cis-trans azobenzene switches [22] and hydrogels based on spiropyran chemistry [23] [2] [3] or molecular motors [24] [25]. Among these systems, spiropyran-based hydrogels have attracted significant attention. Due to the high-water content and similarity to extracellular matrix, hydrogels offer the possibility of functioning in water and have the potential to exchange fluids with aqueous environments compared to other solid actuating materials.

The design of materials coupled with active actuation mechanisms plays a vital role in determining their applicability and performance. Recently, origami, the art of paper folding, has inspired the design of various technologies including deployable structures for aerospace applications [26] and stents for biomedical applications [27] [28]. The shape transformations of flat two-dimensional sheets into folded three-dimensional origami structures have resulted in materials that exhibit exotic mechanical properties [29] [30]. Origami also provides a bottom-up approach for the fabrication of 3D structures that would otherwise be difficult to manufacture [31]. In the field of soft robotics, origami has inspired the design of various transformable robots [32] [33] [34]. Previously, bilayered or multilayered designs have been used to create origami structures [35] [36] [37] [38] where the structures fold due to differential swelling between the layers. This strategy can make the fabrication process complex and, more importantly, the shape changes of layered origami are restricted to predesigned shapes since the swelling ratio of each layer is fixed. Single layered spiropyran hydrogels can overcome these drawbacks since the light naturally decays in-

side the material and creates a gradient of hydrophobicity, which induces curvature, and switching the light off allows the material to relax to its original flat geometry [39]. This folding-unfolding process is highly reversible, and the actuation dynamics depend on the environmental irradiation conditions. In this work, we design and fabricate a reversibly folding origami sheet actuated by light using a single layer film prepared from a spiropyran hydrogel. We exploit composites of photoactive and photoinactive hydrogels to create active fold patterns for the origami sheets. Using a theoretical description of active hydrogels, we simulate and predict the response of these origami sheets to various control parameters. Furthermore, we demonstrate different modalities of buckling that produce diverse patterns such as concave-convex buckled membranes.

2.3   Results and Discussion

2.3.1   Photoactive hydrogels

The photoactive hydrogels were created using copolymerization of a polymerizable spiropyran photoswitch with N-isopropylacrylamide (NIPAM) monomer and N,N'-methylenebisacrylamide (MBAAm) crosslinker (See [16, Appendix A] for details). These photoswitches display a protonated and charged ring-opening form (merocyanine) in the dark under acidic environments and isomerized to a non-charged hydrophobic ring-closed form (spiropyran) upon irradiation, which was verified by UV-Vis spectroscopy [16, Appendix A Fig.6]. We used rheological measurements to test the mechanical properties of the formed hydrogels. [16, Appendix A Fig.7] shows that the storage modulus is as high as 2000 Pa, demonstrating the mechanical robustness of the hydrogel, which is critical for the thereafter actuation and robotic functions. The prepared hydrogel sheet (10.0 mm long, 10.0 mm wide, 0.5 mm thick) contracted to 83% of its original size upon irradiation with white light ($470 mW/cm^2$, see [16, Appendix A] for details). The hydrogel sheet recovered the original swelling state in the dark, and the contraction-expansion process was found

to be highly reversible by alternately switching the light on and off [16, Appendix A Fig.8]. The chemical equation for the spiropyran conversion can be written as shown below where MCH⁺, the hydrophilic moiety of the spiropyran gets converted to SP, the hydrophobic moiety in the presence of light.

Merocyanine (MCH⁺)   **Spiropyran (SP)**
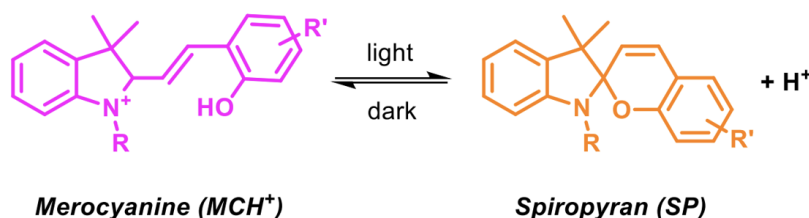
For a quantitative description of the reaction, we write the chemical kinetic rate equation for the conversion of spiropyran from MCH⁺ to SP as follows:

$$\frac{\partial r_{sp}}{\partial t} = k_L(I(\mathbf{x}))r_{mch} - k_D r_{sp} \tag{2.1}$$

where r_{mch} and r_{sp} are the fractions of spiropyrans in MCH⁺ and SP moieties respectively ($r_{mch} + r_{sp} = 1$); k_D is the backward reaction rate coefficient which is a constant at a given substituent, temperature, and pH; and k_L is the forward reaction rate coefficient, which depends on the intensity of light (I). For a unidirectional and monochromatic [40] light source with frequency ν, $k_L(I)$ can be written as:

$$k_L = \frac{\Psi_{\nu,mch}}{h\nu}\epsilon_I\nu, mch \tag{2.2}$$

where $\Psi_{\nu,mch}$ is the quantum yield of the MCH⁺ moiety which is defined as the number of reactions per photon, $\epsilon_{\nu,mch}$ is the molar absorptivity of MCH⁺ moiety and h is Planck's constant. Light triggers the chemical reaction which makes the hydrogel more hydrophobic and bending

of the photoactive hydrogel is determined by the propagation of light in the material. As light propagates through the material thickness, its intensity decays and creates a spatial gradient in the distribution of the hydrophilic and hydrophobic moieties within the hydrogel. This creates a gradient in the water concentration, which in turn leads to a mechanical deformation of the material.

The decay in the light intensity is primarily attributed to the absorption caused by the photochemical reaction itself, where the absorptivity of the material changes as the chemical reaction progresses. The propagation of light in the material is deeply coupled with the chemical reaction because of their interdependent relation. This process can be described by the Beer-Lambert law with the total absorption $A = \epsilon_{mch} c_{mch}$, where ϵ_{mch} and c_{mch} are the molar absorptivity and the molar concentration of the MCH$^+$ chromophore (note the difference between c_{mch} and r_{mch}), respectively. Therefore, the intensity of light propagating in the z-direction can be calculated using the differential equation:

$$\frac{\partial I}{\partial z} + AI = 0 \tag{2.3}$$

The molar concentration c_{mch} can be written in terms of r_{mch} using the equation:

$$c_{mch} = r_{mch} \frac{f\phi}{v_m N_A} \tag{2.4}$$

Here, f is the fraction of monomers in the hydrogel that are chromophores; ϕ is the volume fraction of the polymer; v_m is the volume of a single monomer of the hydrogel; and N_A is the Avogadro's number. Therefore, we can rewrite equation 2.3 as below:

$$\frac{\partial I}{\partial z} + \left(\epsilon_{mch} r_{mch} \frac{f\phi}{v_m N_A} \right) I = 0 \tag{2.5}$$
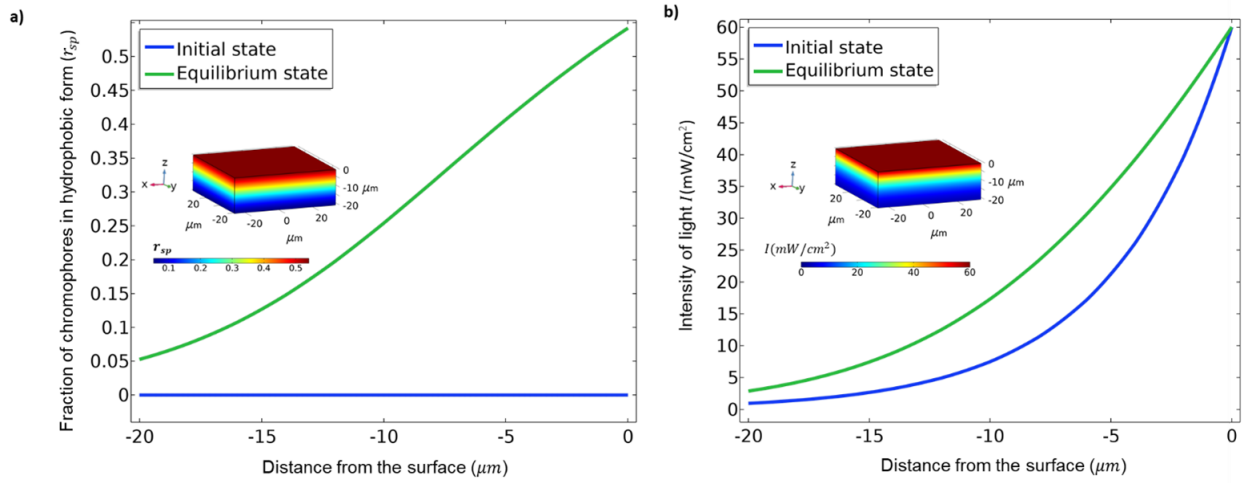
Figure 2.1: Light induced gradients - Finite Element calculation for a block of spiropyran-NiPAAm system in the presence of light (propagating in -z direction) at $60mW/cm^2$. a) Plot showing fraction of SP moiety, r_{sp} induced due to light as a function of distance from the (light receiving) surface in the initial state (time = 0) and the equilibrium state. Inset shows the corresponding 3D plot of r_{sp} in the hydrogel in equilibrium state. b) Plot showing the intensity of light as it decays through the thickness of the hydrogel in the initial and equilibrium states. Inset shows the corresponding 3D plot of light intensity in the hydrogel in equilibrium state. Note: The induced deformation is not considered in these calculations

Equations 2.1 and 2.5 determine the distribution of MCH[+] and SP species in the hydrogel. Figure 2.1 shows finite element calculations for the r_{sp} and the light intensity I within a block of the photoactive hydrogel irradiated at $60mW/cm^2$ under initial ($r_{sp} = 0$) and equilibrium conditions ($\partial r_{sp}/\partial t = 0$). The 1D plots show the dependence of r_{sp} and I as a function of the distance from the light receiving surface of the hydrogel. Here, the light is propagating in the -z direction.

The deformation induced by the light can be calculated using the free energy density of the hydrogel (see chapter 1 section 1.3) [13] [11]. The energy density for the spiropyran-NiPAAm system can be written as a sum of three terms: $U_{elastic}$ accounts for the elasticity of the hydrogel's polymer matrix, U_{mix} accounts for the interaction between the solvent and the polymer network

and U_{photo} accounts for the interaction of the hydrogel with light,

$$U_{total} = U_{elastic} + U_{mix} + U_{photo} \tag{2.6}$$

where $U_{elastic}$ and U_{mix} are given by eq. 1.25 and eq. 1.26 respectively. To describe the photo-induced effects on the free energy of the hydrogel, the term U_{photo} is added to the free energy of the hydrogel given by [41]

$$U_{photo} = \frac{k_B T}{v_m} \alpha r_{sp} (1 - \phi) \tag{2.7}$$

Note: eq. 2.7 describes the energy density with respect to a dry polymer state. For the purpose of numerical simulations/calculations rewrite U_{photo} with respect to a partially swollen reference state (with $\phi = \phi_0$) as described in chapter 1 section 1.4.1 i.e. $U_{photo}(\phi) \rightarrow \phi_0 U_{photo}(\phi_0 \phi)$.

Here, the parameter α is given by

$$\alpha = \frac{zf}{k_B T}(u_{ss} - u_{ms}) \tag{2.8}$$

where u_{ss} and u_{ms} are the interaction energies of the SP and MCH$^+$ moieties with the solvent, respectively; z is the coordination number of the lattice; and f is the fraction of monomers in the hydrogel that are chromophores. Since the interaction energies in equation 2.8 are not known, α is used as a fitting parameter. We know, SP moiety is more hydrophobic than MCH$^+$, therefore, α has a positive value. Recently, Li, Iscen, Palmer, *et al.* [3] showed that spiropyran molecules can be also chemically altered to become more hydrophilic upon light irradiation, in which case, α would attain a negative value. We note that the same theoretical description can be used for positive or negative α.

The hyperelastic model of the photoresponsive hydrogel was solved using the solid mechanics

module of the finite element software, COMSOL [14] along with the coupled chemical reaction and light propagation equations. The list of all the parameters used in the finite element calculation is given in Tab. 2.3.1. The quantum yield Ψ (eq. 2.2), is arbitrarily chosen but this parameter does not affect the physics of the problem. This is because any transformation of the following type leaves the full set of equations invariant:

$$\Psi \to c\Psi \text{ and } I \to I/c$$

where I is the intensity of the incident light and c is an arbitrary scaling factor. Therefore, we can choose any arbitrary value for ψ and sweep the light intensity, I to tune the geometry to the required shape. We choose the value of Ψ to be equal to 0.01916 to match the scale of theoretical values of light intensities to the experimentally used intensity values.

In the absence of light, the hydrogel can freely swell and equilibrate with the surrounding solvent. The total stress on the material in this state is zero. This condition can be used to calculate the relation between the initial polymer volume fraction ϕ_0 and the interaction parameter χ. Using the no-stress condition, $\frac{\partial U/\phi}{\partial \phi} = 0$, we get [12]

$$\chi = -\frac{\phi_0^{-5/3}}{N_x} - \frac{log\left(1 - \phi_0\right)}{\phi_0^2} - \frac{1}{\phi_0} \tag{2.9}$$

This is the same expression as eq. 1.28 except the equilibrium volume fraction ϕ_{eq} in eq. 1.28 is the initial volume fraction ϕ_0 for the purpose of this model.

The First Piola-Kirchhoff stress tensor, **P** is calculated using the equation:

$$P_{ij} = \frac{\partial U(F_{ij})}{\partial F_{ij}} \tag{2.10}$$

Here, U is the free energy density of the hydrogel in the reference configuration and F_{ij} is the deformation gradient tensor. In the absence of any external force, the following force balance

Parameter	Description	Value
$\epsilon_{\nu,mch}$	Absorption coefficient of MCH$^+$	$10^6 L/mole.m$
f	Fraction of chromophores to the total number of monomers in the gel	0.05
ν	Wavelength of light absorbed by the gel	$410nm$
$\Psi_{\nu,mch}$	Quantum yield of the chromophores	0.01916
k_d	Backward reaction rate coefficient	$0.05s^{-1}$
α	Light interaction parameter	0.0925
T	Temperature	$298K$
v_m	Volume of a monomer	$3 \times 10^{-29}m^3$
ϕ_0	Volume fraction in absence of light	0.05
N_x	Mean number of monomers between neighbouring crosslink junctions in the polymer mesh	25000

Table 2.1: The table of values for all the relevant parameters used in the theory

equation can be used to calculate the equilibrium deformation of the hydrogel in the presence of light.

$$\frac{\partial P_{ij}}{\partial X_j} = 0 \tag{2.11}$$

2.3.2 Light-induced buckling

Any light-exposed volume of the hydrogel becomes hydrophobic and expels water, thereby shrinking isotropically. However, due to the gradient of hydrophobicity set up by the light (fig.2.1a (inset)), the isotropy in the z-direction is broken as the face of the hydrogel closer to the light shrinks more compared to the face of the hydrogel further away from the light. For small intensities of light, the deformation in the light-facing side is small and the material maintains its isotropy in the x-y plane as it bends towards the light. As the light intensity increases, the decay in the intensity causes a larger difference in the shrinking ratios between the light-facing side and the light-opposing side. This creates an increase in the elastic stress that leads to the buckling of
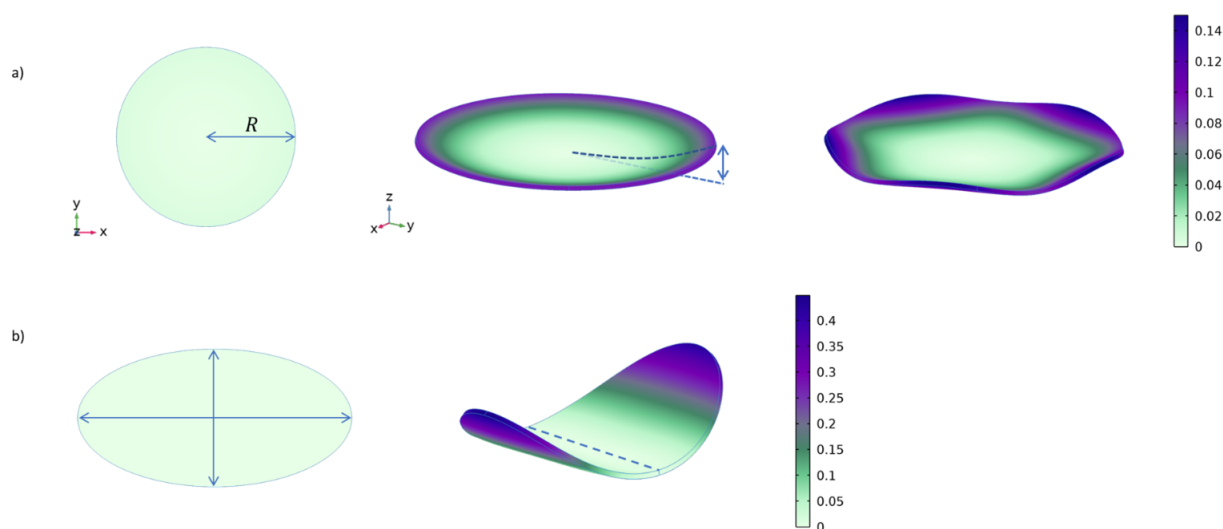
Figure 2.2: Light induced deformation - a) A photoresponsive hydrogel disk in the undeformed state (left) undergoing deformation under light exposure (light propagating in -z direction). At low light intensities the disk deforms into a dome shape (middle) but as the intensity increases, the internal stress causes the disk to buckle, and we find that undulations form around the rim (right). The colour bar represents the displacement of the disk with respect to initial shape in units of the radius, R. b) An ellipse in the undeformed state (left) and buckled state (right). The colour bar represents the displacement with respect to the initial shape in units of semi-major axis.

the material beyond a critical light intensity. To characterize the buckling behavior, we solve the continuum model under equilibrium conditions using finite element analysis. Figure 2.2 shows the calculated buckled states of a hydrogel sheet for two different geometries. Fig 2.2a shows the case of a circular hydrogel disk. At low light intensity, the disk bends into a dome shape, whereas above a critical intensity, the disk buckles to form undulations along its circumference, breaking its radial symmetry. The number of undulations depends on the mode of buckling (see supplementary information section 2.5). However, the behaviour is very different for a geometry such as an ellipse. The ellipse unlike a disk has a preferred direction of buckling. The ellipse prefers to buckle about the semi-minor axis as shown in Fig. 2.2b since the geometry has the smallest bending stiffness

along the long axis. This demonstrates that the shape of the material plays a vital role in determining its post-buckling state. However, the material can also be forced to buckle about any arbitrary axis using the two different methods described below.

1. Reinforcement. Photoactive hydrogels reinforced with nanowires have been shown to bend about the direction of the nanowires [6] (the reinforcement model will be described in more detail in chapter 4). These nanowires create an anisotropic elastic response in the material. The elasticity of the material is different in the direction of the fiber compared to the direction perpendicular to the fiber. Therefore, by designing the material reinforcement, the hydrogel can be forced to buckle about any desired axis. A similar reinforcement-like effect can also be induced using a photo-inactive gel in combination with a photoactive hydrogel. These composites can drastically change the natural buckling behavior of photoactive hydrogels.

2. Photo-active-inactive hydrogel composites. The bending behavior of a photoactive hydrogel can be modified by combining it with a blank hydrogel (photo-inactive). Figure 2.3 shows the case of a rectangular strip of photoactive hydrogel where the light is shone from above (propagating in $-z$ direction). The hydrogel strip would ideally bend about the shorter edge as demonstrated in Fig.2.3a but due to the presence of the blank gel, the photoactive strip instead bends about the long edge. This happens because it is energetically favourable for the blank hydrogel to maintain its initial flat state as it is not affected by the light. The blank gel essentially works as a reinforcement for the photoactive hydrogel strip. As a result, it forces the photoactive strip to change its bending direction.

2.3.3 Photoactive origami

The photo-active-inactive hydrogel composites can be used to create films that fold in the desired manner upon light irradiation. Fig.2.3a shows the construction of a simple origami fold. The
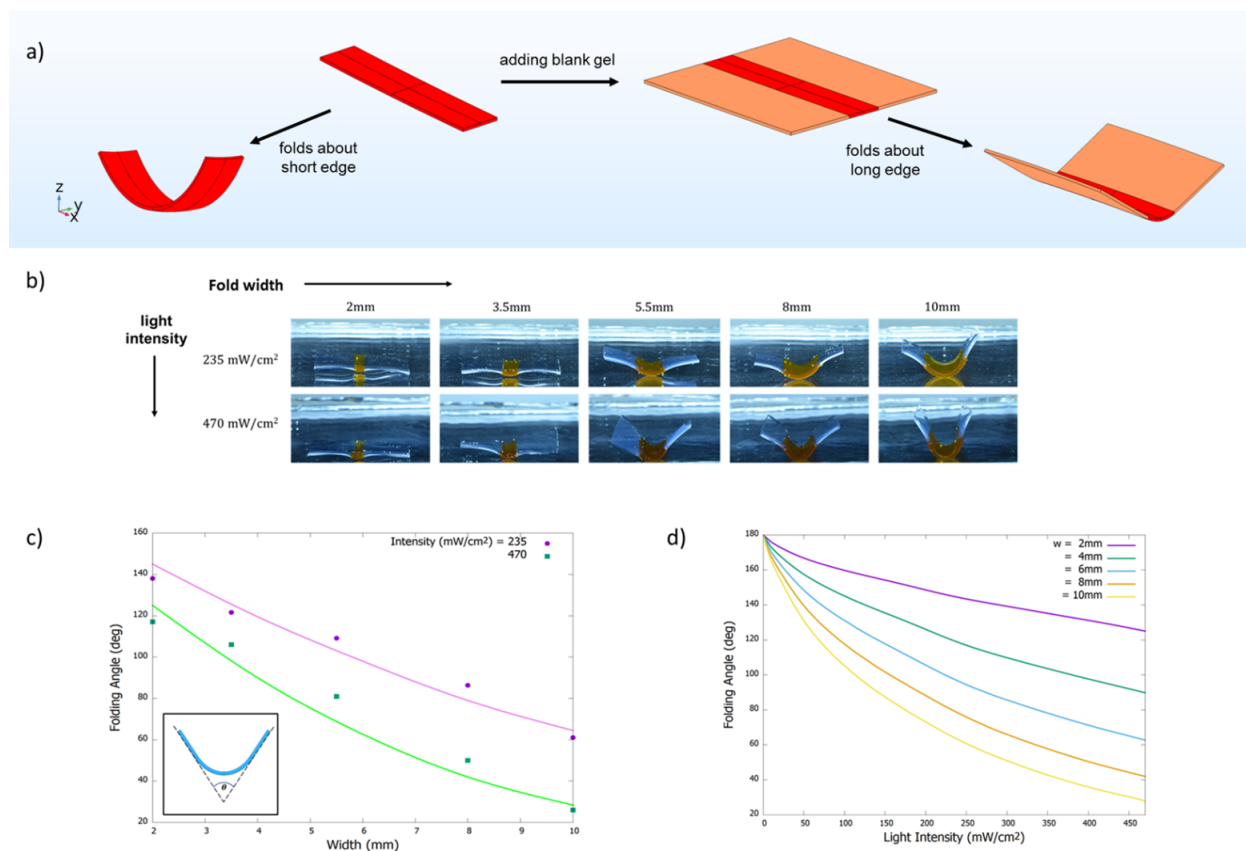
Figure 2.3: Photo-active fold line - a) FE calculation demonstrating the change in the bending direction due to the presence of photo-inactive (blank) hydrogel. The hydrogel strip bends about the shorter edge upon being irradiated with light but bends about the longer edge after adding the blank gel. b) Photographs of samples with single photoactive fold-lines of varying widths after irradiating with different light intensities for 30 min. The photographs show the dependence of folding angle on the linewidth and the light intensity. c) Plot of folding angle with respect to the width of the photoactive line. The symbols represent the experimental values for two different light intensities and the solid curves represent the corresponding theoretical fits attained using the continuum model. (inset) shows the definition of the folding angle used. d) Theoretical plot of the folding angle with respect to the light intensity, I for various widths of photoactive fold-line calculated using FE analysis.

embedded photo-active strip in a blank hydrogel sheet acts like a fold-line that can be controlled using light. Each fold-line in the origami sheet can be individually controlled. The folding angle of a fold-line depends on both fixed parameters and controllable parameters. Fixed parameters include both the chemical parameters such as the spiropyran doping ratio, gel elasticity, and solvent interaction parameter of the hydrogel, while the geometry-dependent factors include the width of the active fold-line. While it is possible to tune the chemical composition of the material, this may not be the easiest way to control the final shape of the origami structure. Therefore, designing the origami with the appropriate fold width is a simple way to achieve the desired structures. As shown in fig.2.3b, we constructed hydrogel sheets of dimensions $20mm \times 10mm \times 0.5mm$ with a photoactive fold-line in the middle. By changing the width of the fold-line, we can control the angle of the fold. Fig.2.3b demonstrates the change in the folding angle for different values of line widths and light intensities in different samples. We modeled this system with parameters derived from the experiments. The list of all parameters used is given in Tab.2.3.1. In Fig. 2.3c, we plot the folding angle of the hydrogel sheet as a function of changing the width of the photoactive fold-line under equilibrium conditions. Here, the folding angle is defined as the angle formed between the two legs of the fold as shown in Fig. 2.3c (inset). The two curves correspond to the intensity values of $235mW/cm^2$ and $470mW/cm^2$. The symbols in Fig. 2.3c represent the experimental data and the solid curves represent the corresponding theoretical fits from the finite element analysis.

Unlike the aforementioned fixed parameters, the intensity of the external light source is a controllable parameter as it can be used to reversibly change the shape of the structures. Fig 2.3d plots the folding angle of the hydrogel sheet as a function of the light intensity calculated for various fold widths using the finite element analysis. Therefore, by appropriately tuning the intensity of the light source, we can allow our pre-designed structures to fold into the desired shapes on the fly. Another advantage of such a system over conventional origami materials is that it is a single-layer
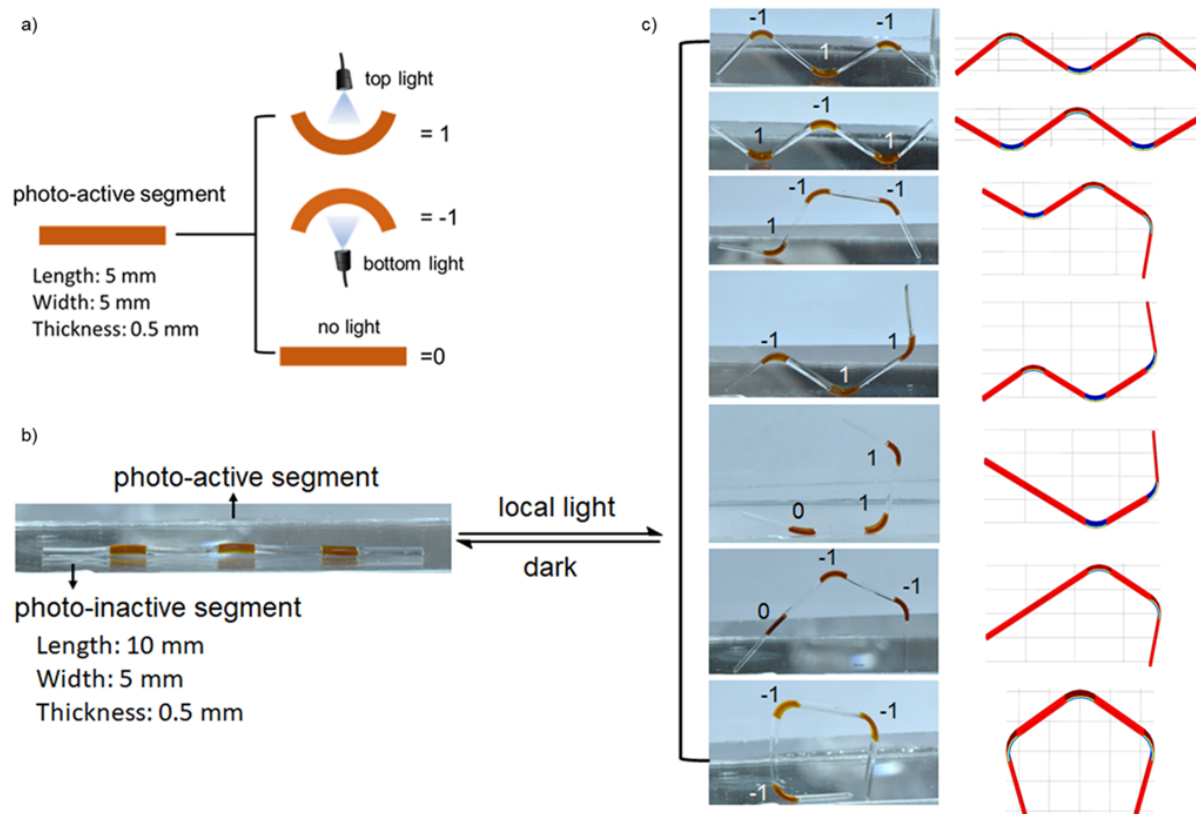
Figure 2.4: Controlling geometry by locally actuating each fold – a) A schematic representation of a photo-active fold-line which can exist in one of three states +1, -1 or 0 which represents light shone from above, light shone from below or no light shone, respectively. b) A photograph of a hydrogel segment with 3 active fold-lines and can fold into 27 possible configurations. c) Photographs and FE calculations of 7 of 27 possible configurations attained by locally actuating each fold independently. In the experiments, it requires 30 min irradiation for the gel samples to reach the final shapes and 1 h to relax in the dark to recover their initial states.

material which makes it easier to fabricate. Furthermore, these origami sheets can fold in either direction depending upon the direction of light, thereby creating both mountain and valley folds.

To demonstrate the functionality, we constructed a structure with three active fold lines (see [16, Appendix A1.6] for synthesis details). As shown in Fig.2.4a, any photoactive segment can have three possible states depending upon the state of the external light source: light shone from

the top labeled as +1 state, light shone from below labeled as -1 state, and no light shone labeled as 0 state. The advantage light offers here is that using light we can independently actuate each fold-line. For a strip with three active fold-lines (Fig. 2.4b), there can be 27 possible configurations and they can dynamically go from one state to another. Fig. 2.4c shows seven of the possible attainable shapes and their corresponding numerical predictions. Please note that all these folding shapes come from the same object, and it is the light sequence that was applied to the object which induced the differences in folding geometries. This result highlights the reconfigurability and versatility of our material, which is different from the bilayered spiropyran hydrogel system previously reported by Li, Xue, Han, *et al.* [38]. The relative ease of fabrication of these devices along with the high accuracy of numerical predictions can help us in creating advanced active materials with a large variety of applications.

2.3.4   Exploring different modalities

The hydrogel sheet buckles into a folded structure due to the reinforcement from the blank gel. As discussed before, the resistance of the blank gel to bending leads to the buckling of the hydrogel sheets. However, the bending stiffness of a sheet can be controlled by changing its elastic modulus or/and its thickness. Here we discuss the changes in the buckling pattern as the hydrogel sheet is miniaturized; thereby decreasing the bending rigidity of the blank gel. As the blank gel is made thinner, we see a mode where the photoactive region begins to develop a negative Gaussian curvature profile. Fig.2.5 shows a $400\mu m \times 300\mu m$ rectangular sheet with a photoactive region with a width of $80\mu m$. Fig.2.5a shows the case where we gradually decrease the thickness of this sheet from $10\mu m$ to $4\mu m$ in steps of $2\mu m$. We see the emergence of a negative Gaussian curvature profile with decreasing thickness. However, this new mode disappears as we increase the elastic modulus of the blank gel as shown in fig.2.5b. This demonstrates the role of blank gel's bending
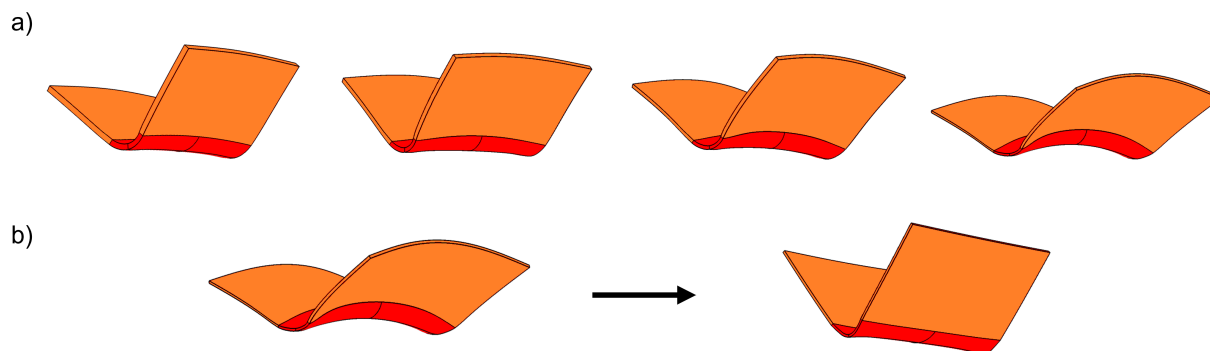
Figure 2.5: Bending rigidity of the blank gel - a) The emergence of negative Gaussian curvature with decreasing thickness of the sheet of dimensions $400 \times 300\mu m$. Starting from left the thicknesses used are $10\mu m$, $8\mu m$, $6\mu m$ and $4\mu m$. b) The negative Gaussian curvature profile (left) disappears by increasing the elastic modulus of the blank gel (right). Thickness of the gel is $4\mu m$. (The light is propagating in $-z$ direction).

stiffness in the buckling of these hydrogel structures. Furthermore, the blank gel can be entirely replaced with a set of boundary conditions and new patterns can emerge. For instance, recently Xiong and Kuksenok [42] showed the emergence of wave-like patterns in an active hydrogel sheet with constrained edges.

2.4   Conclusion

This paper focuses on the design of a light-responsive spiropyran hydrogel system that can display various dynamic shape changes using a single material upon irradiation with local light. The origami patterned created could be erased in the dark and the materials could be re-used by applying a second irradiation sequence to create other origami shapes. This high dynamic property makes our hydrogel different from previous systems. We design structures that display specific buckling modes and discuss the synthesis details of these photoactive hydrogel structures. We use a continuum polymer model to analyse the hydrogel behaviour by implementing polymer gel elasticity theory and the hydrogel response to the light in the finite element software COMSOL.
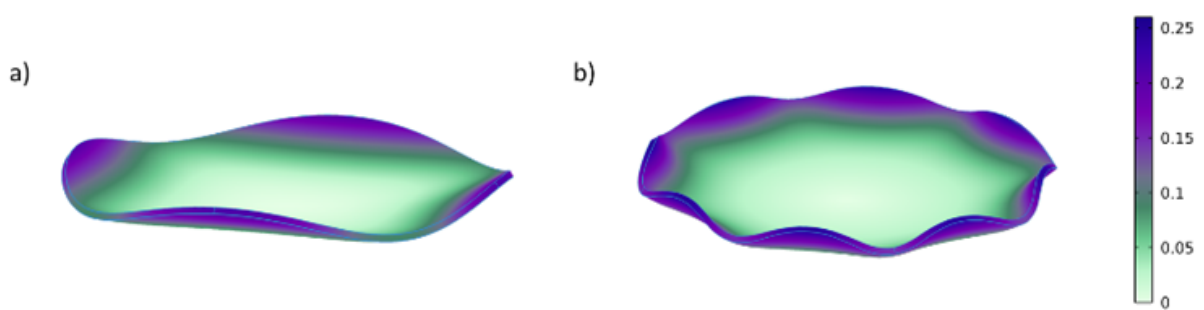
Figure 2.6: Some of the buckling modes of a disk. a) 4-fold symmetric structure and b) 8-fold symmetric structure. The colour bar represents the displacement of the disk in units of its radius, R.

We verify our theoretical predictions against experimental results. Our modelling approach allows us to explore various possible patterns in light-responsive hydrogels in different parameter-space regimes. The photoactive hydrogel system and the theoretical model developed here provide the guidelines to aid the development of more complex structures and devices.

2.5   Supplementary Information

Buckling modes of a circular disk

A full study of buckling modes of a disk is beyond the scope of this article. However, we did a post-buckling analysis by ramping up the light intensity at different rates and got different modes in which the disk can buckle. Figure 2.6 shows two of the many different modes that the disk can buckle into. Fig. 2.6a shows the emergence of a 4-fold symmetric structure and fig. 2.6b shows an 8-fold symmetric structure.

CHAPTER 3

CHEMICALLY CONTROLLED PATTERN FORMATION IN SELF-OSCILLATING ELASTIC SHELLS

3.1 Abstract

Patterns and morphology develop in living systems such as embryos in response to chemical signals. To understand and exploit the interplay of chemical reactions with mechanical transformations, chemo-mechanical polymer systems have been synthesized by attaching chemicals into hydrogels. In this work, we design autonomous responsive elastic shells that undergo morphological changes induced by chemical reactions. We couple the local mechanical response of the gel with the chemical processes on the shell. This causes swelling and deswelling of the gel, generating diverse morphological changes, including periodic oscillations. We further introduce a mechanical instability and observe buckling-unbuckling dynamics with a response time delay. Moreover, we investigate the mechanical feedback on the chemical reaction and demonstrate the dynamic patterns triggered by an initial deformation. We show the chemical characteristics that account for the shell morphology and discuss the future designs for autonomous responsive materials.

3.2 Introduction

Chemical reactions are key components in morphogenesis and are essential to assemble mechano-responsive materials with self-healing and adaptive properties [43]–[46]. In particular, the coupling of chemical reactions with responsive gels has offered the possibility to create autonomous materials that convert chemical energy into mechanical energy [47]–[51] that resemble heart beating dynamics. The design and synthesis of materials with biological functions is a challenge that involves a delicate balance between structural shape and physiological function. During embryonic development, for example, flat sheets of embryonic cells morph through a series of folds into intricate three-dimensional structures such as branches, tubes, and furrows that build blocks for organs that enable their proper function. Such shape-forming processes are driven by controlling chemical and mechanical signaling events.

Man-made chemo-morph systems, however, are less common than the biological counterpart. Only recently, reconfigurable soft robots have been proposed [52]–[54]. One of the main advantages of soft materials is that they do not need mechanical parts; the motion is driven by external chemophysical signals. Rhythmic swelling and contractions in response to chemical changes have been observed [55]–[59]. The synergy between chemical interactions and locally directed forces lead to selection rules for sizes and shapes that autonomously generate motion [8].

In chemo-responsive soft materials, the complex nature of microscopic interaction contributes to a macroscopic morphology [3], [60]. The diffusion of reactants, for example, can in principle elicit different responses due to mechanical deformation. As in morphogenetic processes, the flow of information is complex and relies on the interplay among all components. That is, chemically generated stresses induce material deformation that influences the chemical regulators in a close feedback loop [61]–[63]. Here, we introduce a model to study the shape dynamics triggered by au-

tonomous chemical reactions in closed elastic shells. We focus on chemical changes that introduce periodical hydration changes that prompt gel swelling.

We study autonomous gel membrane dynamics triggered by periodic reduction-oxidation reactions that generate membrane hydration heterogeneities. Instead of considering two-dimensional elastic models for mechanically heterogeneous crystalline small shells that buckled into polyhedral [64], we consider thin membranes elasticity models that generate wrinkling by imposing the metric [65], [66]. That is, in order to include the response to the chemical field on the membrane we integrate the chemical field on a non-Euclidean shell elasticity models [67], [68] and in such way investigate the local hydration impact on membrane morphological changes. We simultaneously incorporate the chemical dilution due to stretching and dynamics associated with the deformed gel and study the mechano-chemical feedback loop. We report a wide variety of morphologies and oscillation behavior that indicates a robust mechanism for the future design of chemo-responsive gels with desired functionality.

3.3   Chemical activated surfaces

We consider a chemo-responsive polymeric thin elastic shell of radius R and thickness $h \ll L$, which is represented by a two-dimensional mid-surface smooth function with no overhangs. The elastic response of the material is modeled using linear elasticity [69] and the chemically induced swelling/shrinking is modeled using the so called 'target metric' approach [70]. The target metric approach models the swelling/shrinking behaviour of a 2D surface by changing its assigned metric from an initial metric to a final or 'target' metric. Under such a transformation, the total free energy of the system does not change, which is consistent with the model of the hydrogels presented in chapter 2 since a freely swelling hydrogel stays at a zero stress state. Fig. 3.1 shows a schematic representation of this approach by demonstrating the case of a 2D square element that undergoes
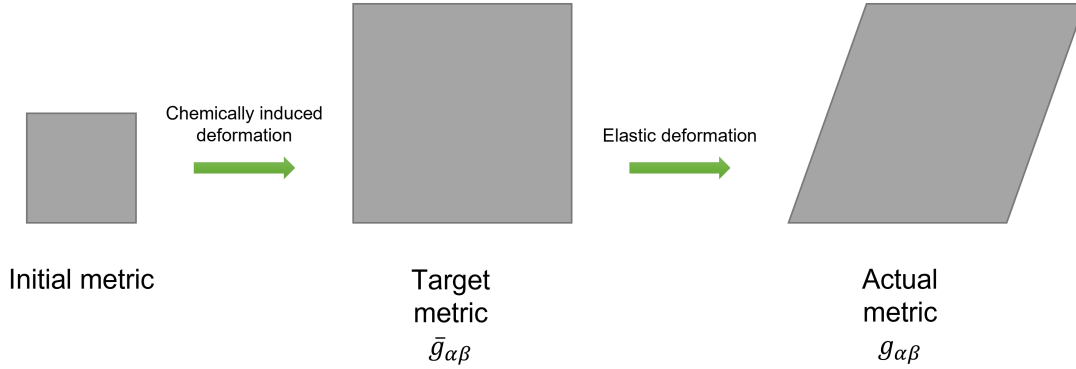
Figure 3.1: Schematic representation of the target metric approach by demonstrating the case of a 2D square element that undergoes a chemically induced deformation followed by an elastic deformation.

a chemically induced deformation followed by an elastic deformation. The elastic energy is only associated with the difference between the target metric and the actual metric (and *not* between the initial metric and the target metric).

The elastic energy associated with the deformation of the mid-surface of the shell can be expressed as [67], [71],

$$
\begin{aligned}
E_{elastic}(g_{\alpha\beta}, \bar{g}_{\alpha\beta}) = \frac{1}{2} \int d\bar{A} \, \mathcal{A}^{ijkl} u_{ij} u_{kl} \\
+ \frac{1}{2} \int d\bar{A} \, \left(\kappa \left(H - 2H_0 \right)^2 + 2\kappa_g G \right).
\end{aligned}
\tag{3.1}
$$

The first term in Eq. (3.1) represents the stretching energy, where $u_{\alpha\beta} = \frac{1}{2} \left(g_{\alpha\beta} - \bar{g}_{\alpha\beta} \right)$ is the strain tensor, $g_{\alpha\beta}$ ($\bar{g}_{\alpha\beta}$) is the actual (target) metric tensor, $d\bar{A} = \sqrt{\det \bar{g}} dx dy$ is the target area element, $\mathcal{A}^{\alpha\beta\gamma\delta}$ is the elastic tensor, and summation over pairs of repeated indices is assumed. For an isotropic material, $\mathcal{A}^{\alpha\beta\gamma\delta} == \frac{Eh}{1-\nu^2}(\nu \bar{g}^{ij} \bar{g}^{kl} + (1-\nu)\bar{g}^{ik} \bar{g}^{jl})$, where E is the Young's modulus and

ν is the Poisson ratio and $\overline{g}^{\alpha\gamma}\overline{g}_{\gamma\beta} = \delta^{\alpha}_{\beta}$. Moreover, the second term accounts for bending energy with the mean curvature H, spontaneous curvature H_0 and the Gaussian curvature G associated with $\kappa = Eh^3/12(1-\nu^2)$ and $\kappa_g = (\nu-1)\kappa$ denote the bending and Gaussian rigidity respectively.

3.3.1 Autonomous oscillatory chemical reactions

Pattern formation is widespread in nature and our daily life, from the formation of animal skin patterns to the design of material and robotics [72]–[75]. In particular, chemical pattern formation is an important process in biology since it ensures the correct placement and development of tissues within a body [76]. In general, pattern-forming systems can be classified into non-autonomous and autonomous (self-organized) patterns. Non-autonomous systems respond to environmental clues and signaling such as chemical gradients. Autonomous chemical patterns, on the other hand, are formed by a complex reaction-diffusion system that involves an activator (autocatalytic chemical) and an inhibitor that slows down the production of the chemicals, which are coupled via a diffusion mechanism for both species [77].

One of the most paradigmatic cases of oscillating pattern formation in gels is the Belousov-Zhabotinsky (BZ) reaction [47], [56], [78]. The BZ reaction is a catalytic oxidation reaction of organic acid by bromate anion. The particular choice of the acid, the organic species or the catalyst give rise to diverse variations of the BZ reaction that involves numerous elementary steps. In the simplest form, the diffusion-reaction system consists of five coupled reactions with both an autocatalytic and a negative feedback loop steps that can be accurately modeled by the time-space Oregonator model [79], [80] (See section 3.6.1 Eqs. 3.5 - 3.7).

$$\frac{du}{dt} = \epsilon D_u \Delta_M u + u - u^2 + fv\frac{q-u}{q+u}$$
$$\frac{dv}{dt} = \epsilon(u - v), \tag{3.2}$$

where u is the activator, denoting the concentration of the reactant and and v is the oxidized form of the catalyst; and the dimensionless variables ϵ, q are defined through the rate constants and the reservoir concentration. In addition, stoichiometric factor f depends on the organic chemistry involved. Moreover, to ensure the existence of oscillations its value has to be in a certain range. Finally, D_u is the bromous acid diffusion coefficient (see Table 3.2). Note that we have taken into account that oxidized catalyst v is moving together with the polymer gel [81].

3.3.2 Mechano-chemical shell dynamics

Following Ref. [66] we discretize equation (3.1) by triangulating the shell surface. We assume overdamped Langevin dynamics and solve the set of first-order equations for the position of each vertex $\mathbf{r}_i$ and discrete metric of each triangle $g_{\alpha\beta}$,

$$\gamma\dot{\mathbf{r}}_i = -\nabla_{\mathbf{r}_i} E_{elastic}\left(g_{\alpha\beta}, \bar{g}_{\alpha\beta}\right) + \boldsymbol{\eta}_i\left(t\right), \tag{3.3}$$

$\boldsymbol{\eta}_i\left(t\right) \in \mathbb{R}^3$ is random noise obeying $\langle\boldsymbol{\eta}_i\rangle = 0$ and $\left\langle\eta_i^m\left(t\right)\eta_j^n\left(t'\right)\right\rangle = \sqrt{2\gamma k_B T}\delta_{ij}\delta_{mn}\delta\left(t - t'\right)$ with $m, n \in \{x, y, z\}$. Here, T is the temperature and γ is the friction coefficient, which we assume to be constant. All the mechano-chemical coupling is modeled through the target metric $\bar{g}_{\alpha\beta}$, that depends on the chemicals (v) embedded in the shell. Equation (3.3) is integrated numeri-

cally using standard first-order Euler-Maruyama discretization scheme keeping connectivity of the triangulation fixed. Finally, equations (3.2) are integrated numerically using discrete exterior calculus operators in space for triangular meshes and explicit discretization in time (see section 3.6, Eq. 3.11).

3.4 Dynamic shell morphology by active-chemical growth

Active structural remodeling   To understand how shell morphology is affected by chemical-induced stresses we first investigate mechanical pattern formation given by a conformal active remodeling step,

$$\bar{g}_{\alpha\beta} = M \bar{g}_{\alpha\beta, t=0}, \tag{3.4}$$

where M is the growth ratio (Fig. 3.2); in this way, the strain field is generated on the shell and it buckles when the shell volume is kept constant. For small M, the shells have spherical shapes with no apparent morphological changes. As the target area increases, however, the shells are under extensive compression where the elastic energy is accumulated until the symmetry is broken and the residual stresses are released by the formation of folds and wrinkles [66], [82]. The undulation wavelength is proportional to the thickness, which scales as the ratio of bending rigidity to stretching rigidity.

Oscillatory mechano-chemical coupling.   The previous example provides a clear path of how to control morphological changes by induced strain fields. In chemo-responsive polymeric shells, such changes are autonomously controlled by the covalent nature of the catalyst v bound to the polymer gel [47], [51], [56]. As the chemical process changes v, the free energy of the hydrogel changes instantaneously, thereby creating an instantaneous stress on the material. This chemically induced stress is then gradually released by the surrounding solvent as the solvent molecules are
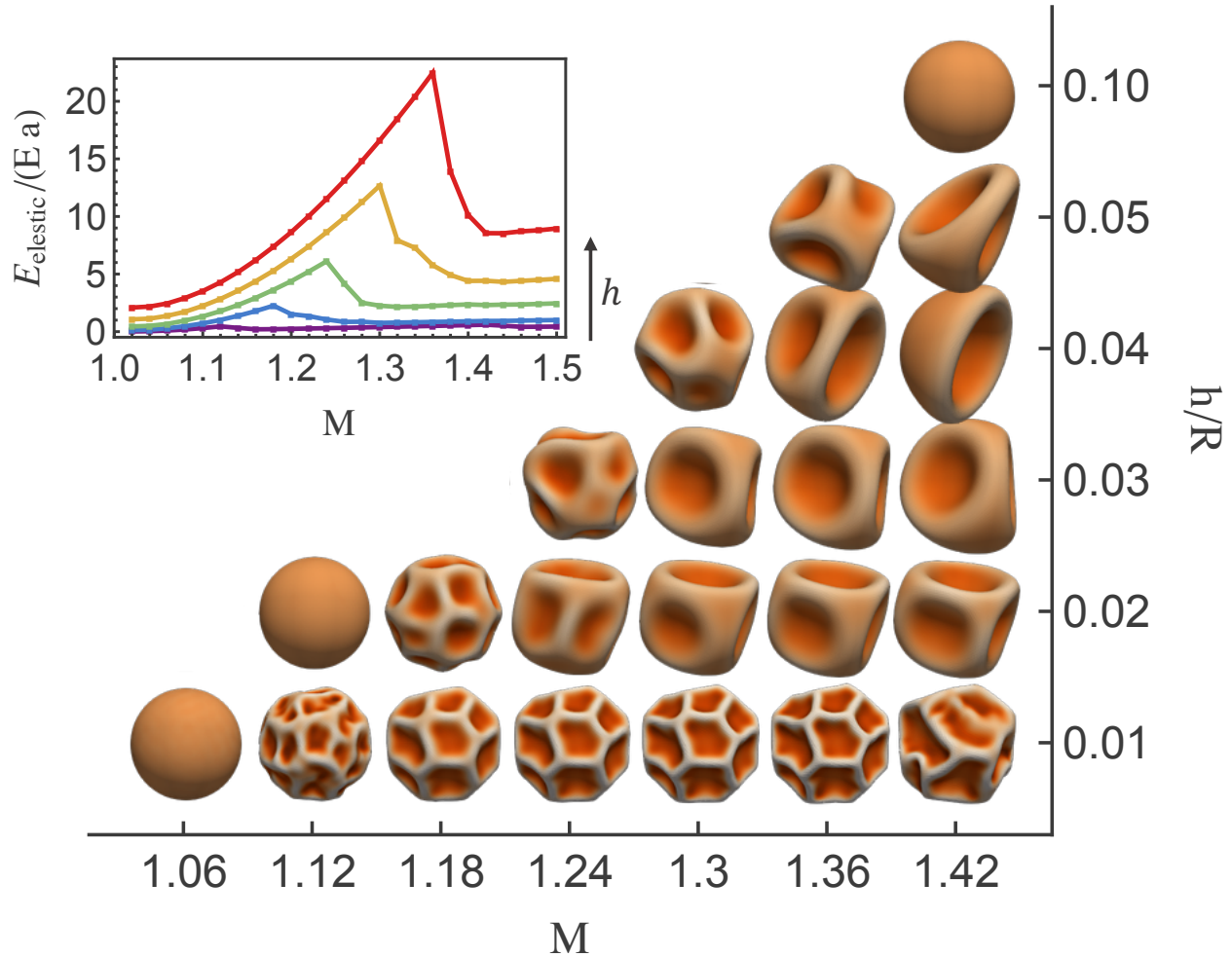
Figure 3.2: An illustration of morphologies a spherical shell of thickness h and radius R as a function of the growth ratio, M (Eq. 3.4). The morphologies are minimum energy (Eq. 1) configurations that are calculated by gradually increasing M while keeping the total volume fixed. For small M, the shells maintain their spherical shape, however, as the growth ratio M increases, the accumulated elastic energy of the shell (inset figure) is released and the shell buckles to form wrinkles on its surface. The color scheme of the plots represents the local mean curvature with negative value on the concave faces and positive on the polyhedron edges. The inset figure plots total elastic energy, E_{elastic} as a function of M for various shell thicknesses. The sharp kink in the plot represents the buckling point.
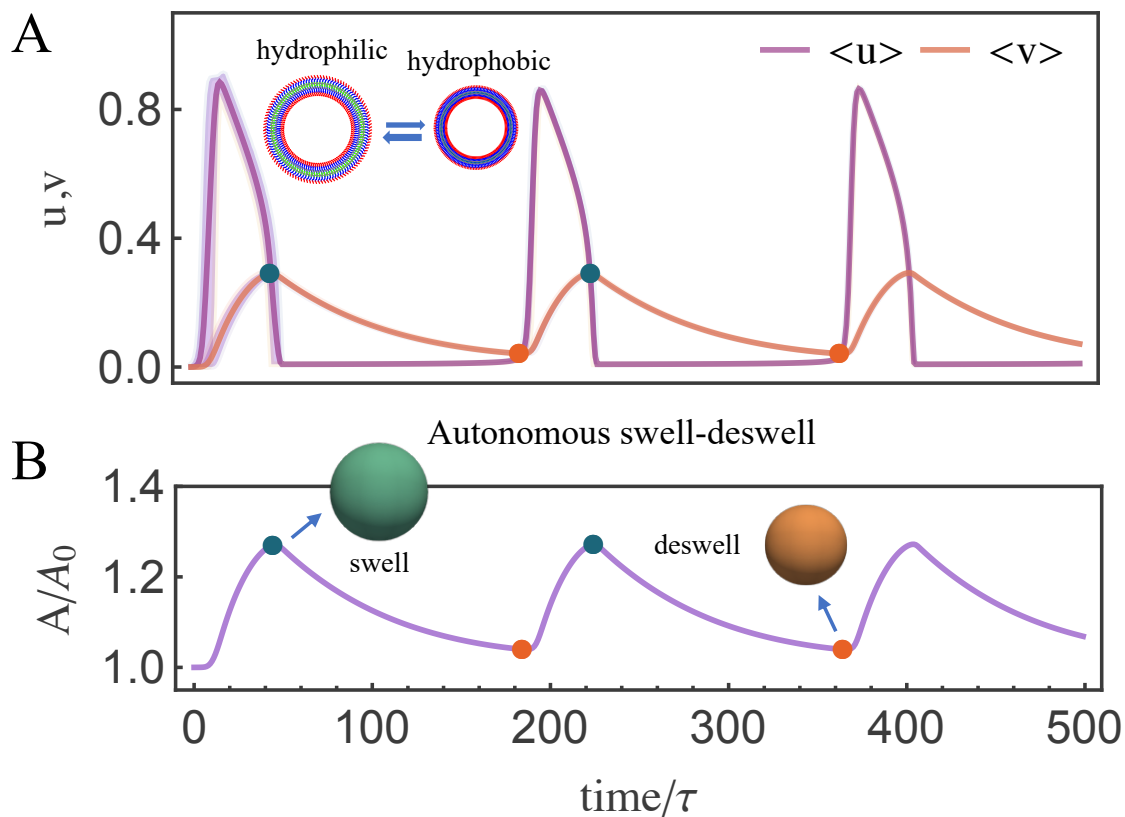
Figure 3.3: A. The plot of the average chemical concentration of reactants u and v on the shell as a function of time. The shell becomes more hydrophilic with an increasing value of v, which leads to swelling of the material. Similarly decreasing the value of v leads to deswelling. B. Plot of the shell area (A/A_0) as a function of time. The plot depicts the direct correspondence between the area ratios and the concentration v.
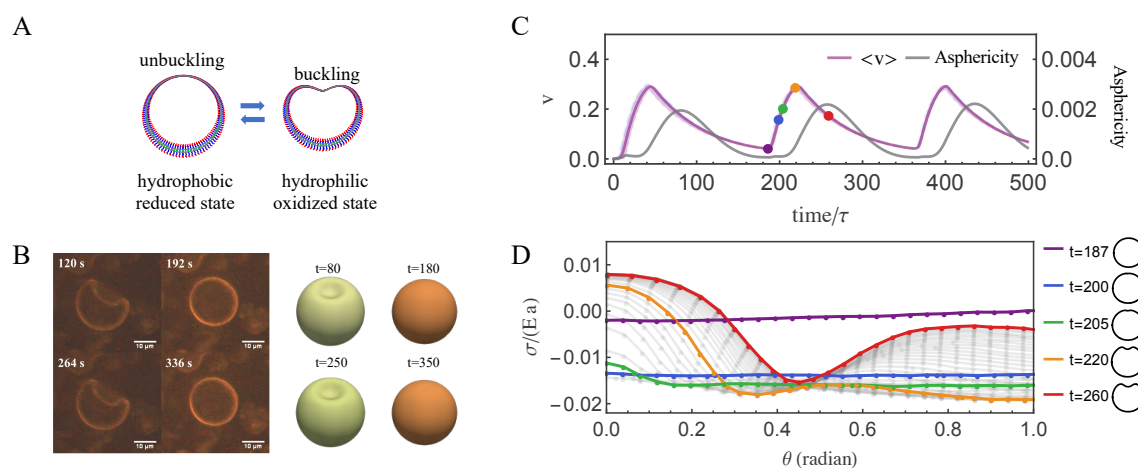
Figure 3.4: Heterogeneous shell dynamics with fast diffusive chemical reaction. A. Schematic polymeric shell with non-uniform thickness h. The spherical shell buckles inward as the polymers become more hydrophilic. B. A comparison of buckling observed experimentally (left, pictures obtained from Ref. [56]) with simulation results (right). The colors of the shell denote the value of catalyst concentration, where yellow means oxidized state and orange represents reduced state [56]. C. Plot of the catalyst concentration (v) and shell asphericity ($\langle \Delta R^2 \rangle / \langle R \rangle^2$) as a function of time. The plot demonstrates the time delay between the increase in v and the mechanical buckling. D. A representation of stress distribution as a function of the polar angle. The shell is under compression with negative stress and tensile with positive stress. The grey lines denote the stresses from time $t = 200$ to $t = 260$ with increment $dt = 2$, and the colored lines are representatives of the second cycle undergoing the buckling transition.

sucked into/out of the material. This leads to changes in the volume of the active gel. Upon solving the model for an unconstrained hydrogel disk we find that for small variations of the catalyst v the changes in the target metric can be expressed as an affine transformation where the growth ratio $M(t) = 1 + \alpha v(t)$ with α a material constant that accounts for the intrinsic properties of the hydrogel such as its cross-link density and the interaction energy of the catalyst v with the solvent (see section 3.6.2). This comparison with the results of a hydrogel modeled as in references [47]–[49], reveals that the linear approximation for the growth ratio M holds for gels with Young's modulus $E \gtrsim 10\text{kPa}$ (see Fig. 3.7). For the purpose of simulations, this exercise allows us to remodel the physics of chemically active polymer gels as an affine transformation. Therefore, this method allows us to study complex systems with relative ease.
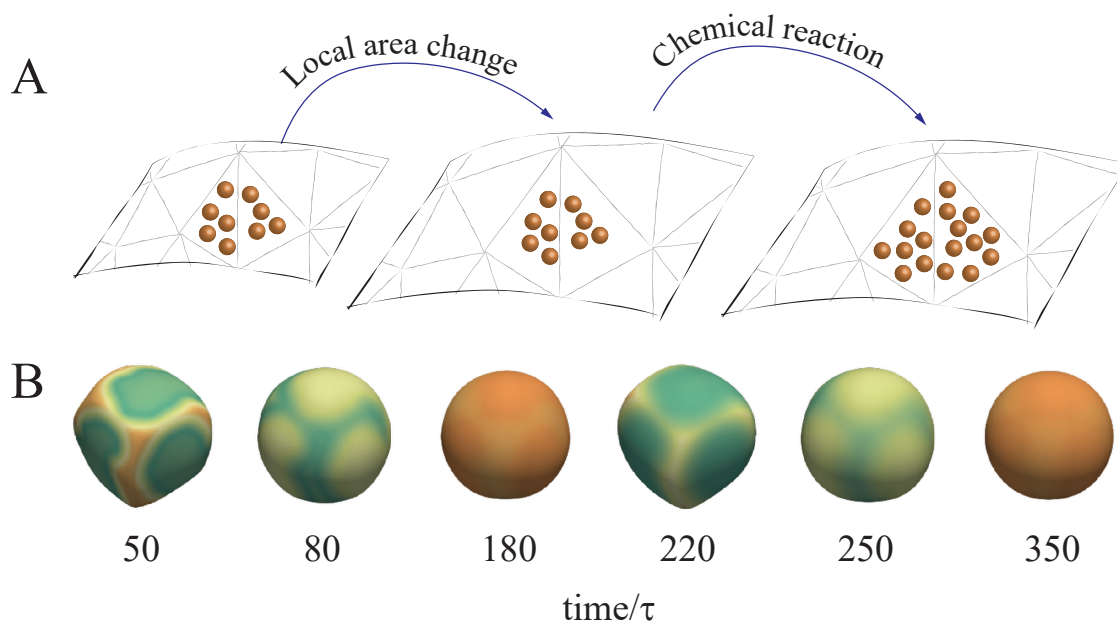
Figure 3.5: Geometrical feedback from local changes in the area. A. If the number of molecules remains fix N, but the area increases, then the chemical concentration gets diluted, given that $c = N/Area$. Deviation from the steady-state of the chemicals can trigger the mechanism of reaction in the Oreganator model. B. Even random deformations can give rise to oscillatory patterns for a close shell due to local area changes.

Similarly to actomyosin contraction in cardiac muscles driven by calcium oscillations [83], [84], BZ reactions can induce swelling-deswelling beating by periodic oxidation and reduction of catalyst. The average u, v concentration profiles as a function of time are plotted in Fig. 3.3A, where the concentration of reactant u and catalyst v periodically oscillate around their stable value u^* and v^*. By coupling the target metric with v, we find in the oxidized state, the shell hydrates due to an increase in the catalyst net charge [50]. Conversely, when the catalyst v is reduced, the shell starts to shrink inducing swelling-deswelling beating waves, see Fig. 3.3B. Note that the shell is subject to a volume penalty (see [7, SI Appendix, section S3C]) to account for the low solvent permeability of the shell.

Interestingly, recent experiments have found swell/deswell and buckling/unbuckling oscillations in synthesized polymersomes, which are cross-linked polymeric shell composed of the catalyst segment and the hydrophilic segment [56]. It is clear that stresses generated by chemical remodeling in a uniform shell are not enough to explain autonomous buckling/unbuckling oscillations shown in the chemo-responsive experiments [56]. Here, we propose that heterogeneities in the shell thickness can justify such behavior. To prove our hypothesis, we spatially varied the shell thickness (Fig. 3.4A) to account for shell design imperfections in real experiments. In agreement with polymersome experiments [56], we observe buckling-unbuckling oscillations consistent with changes in the catalyst concentration (Fig. 3.4B). The shape oscillations can be understood as follows. As the catalyst concentration increases from its minimal values ($t = 187 \rightarrow 200$, Fig. 3.4C) a strain field generated by changes in the degree of hydration and the shell starts to build-up residual stresses (Fig. 3.4D). For values of the catalyst larger than $v = 0.16$ the degree of hydration is such that the shell swells releasing the residual stresses built and consequently buckles (Fig. 3.4D in red). In addition to the morphology with a single buckling point (Fig. 3.4B), we also find multiple buckling seeds as we increase the thinnest thickness of the shell. In this case, two concave

buckling sites are observed in the first cycle, which slowly converge to one buckling point (see [7, SI Appendix, Fig. S2]). The result is consistent with the recent colloidosome experiment, where multiple buckling and moving buckling points are observed analogous to biological cells [85]. Compared to the equilibrium case, we find the moving buckling points are likely introduced in the deformation pathway as a kinetic process, where the relaxation time is not sufficient to release the internal stress.

Geometrical feedback In addition, shell deformations give rise to fluctuations in the catalyst concentration (Fig. 3.5) which can be understood by two main contributions: changes in the local area and the curvature. Changes in the local area modify the chemical concentration (Note that concentration c is defined by $c = N/Area$, where N is the number of molecules) as illustrated in Fig. 3.5A. As the local area grows, the chemical concentration (v) is diluted below the steady value (v^*) and the chemical reaction is triggered hereon. To test this geometrical feedback, we introduce a small random force on the shell and investigate how area changes give rise to chemical patterns (Fig. 3.5B). We observe that even the smallest amount of changes in the area can trigger significant deviation from v^*, provoking the onset of the chemical reactions. Since our approach is based on approximations for thin sheets, the chemical dilution due to the changes of thickness is not considered here. However, other curvature effects (such as the mean curvature) are considered within the Laplace operator in curved spaces [86]. We note, however, the feedback from the curvature is small compared to the contribution from area changes.

Material design through mechano-chemical coupling

Now that we have established the foundation for mechano-chemical coupling in polymer shells, we focus on possible material design [87]. With that intent, in this section, we explore the possibility
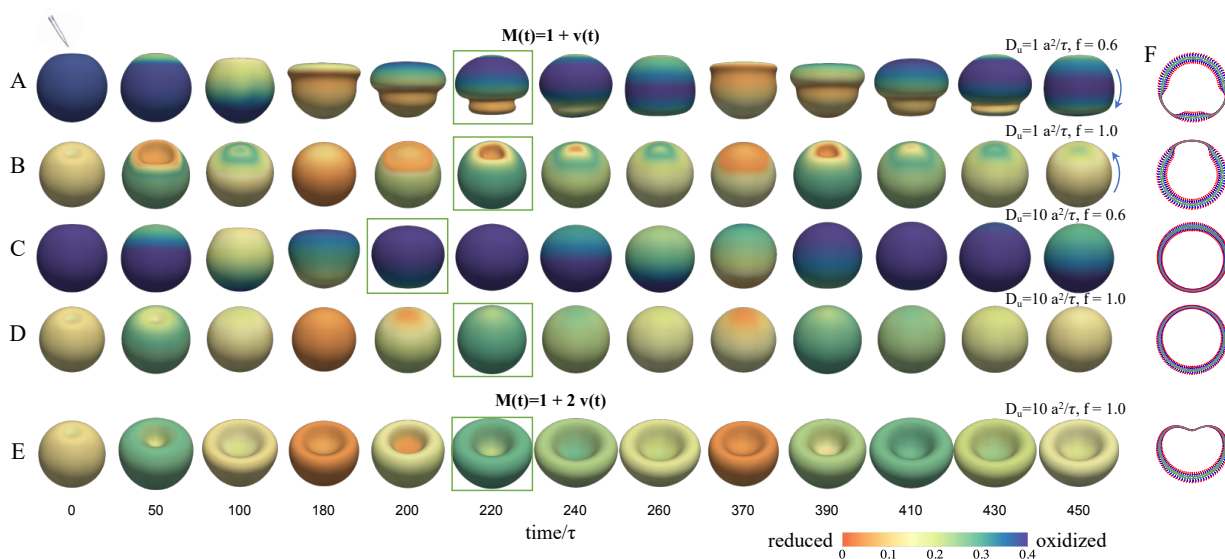
Figure 3.6: A-E. The shell morphology dynamics with different diffusion coefficients and stoichiometric factor f. The colors represent the catalyst concentration: blue when the polymer is oxidized and orange in a reduced state. The shell is first relaxed with respect to a stable value of catalyst concentration v^*, followed by a mechanical press. The initial deformation of the shell causes the chemical dilution and generates the reduction wave from the top and the oxidization wave from the bottom. The overall wave directions are opposite for $f = 0.6$ and $f = 1.0$, leading to a mushroom shape or exocytosis dynamics. The patterns in the boxes periodically appear with schematic illustrations of the thickness shown on the right. F. The schematic figures to illustrate the thickness distribution of the shells marked in the green boxes.

of multi-responsive materials as a mechanism for generating functional morphological shapes. We consider an in silico material with chemical thickness response of the form $h(r, t) = h_0 + \zeta \, v(r, t)$, where h_0 and ζ are chosen so the minimum thickness of the polymer shell is $h_{min} = 0.1a$ and the maximum $h_{max} = 1.0a$, with a the length unit.

First, we investigate the possibility of generating self-adapting materials by exploring how the shell can mobilize the reactants. We find that the best way to do it is by mass-transfer effects, that is, by changing the ratio of bromide ion to the catalyst ions during the malonic acid oxidation step; or by changing how fast the bromous acid is replaced via the diffusion process. In other words, by changing the stoichiometric factor f or the diffusion coefficient D_u in the reduced system of equations given in Eq. 3.2.

The computational experiment starts by establishing a stable chemical concentration of v^*. Then we introduce a local shell deformation by pipette-pressing the shell, $t = 0$ in Fig. 3.6. The local mechanical changes of the shell generate a chemical concentration gradient in the north and south poles of the shell due to a dilution introduced by the expansion of the material.

As the reaction evolves, two primary waves are generated, a reduction wave from the north pole and an oxidization wave from the south pole. The two waves travel oppositely and meet at a counter-line (Fig. 3.6A). For $f = 0.6$, the reduction wave out-speeds the oxidation wave ($t = 100$), and the combined wave moves downwards until the whole shell is under a reduced state ($t = 180$). Immediately after, the shell rapidly develops an oxidization wavefront generating local thickness gradients, inducing a mushroom-like morphology with negative Gaussian curvature ($t = 220$). As the wavefront approaches the south pole the shell is compressed accumulating a large concentration of chemicals that generates a quick wave response that moves the deformation to the north pole ($t = 370$). As f increases (Fig. 3.6B) the oxidization wave out-competes the reduction wave and pushes the counter-line upwards. The overall wave moves oppositely from bottom to top, forming

a periodic exocytosis morphology. As the diffusive mass-transfer effect increases (Fig. 3.6C-D) the deformation weakens for both $f = 0.6$ and $f = 1.0$, increasing the resistance to hydration effects and therefore its adaptability. At even larger $D_u = 100a^2/\tau$, the mechanical relaxation time is longer than the diffusion time scale, and the shells converge to the homogeneous state.

Lastly, we investigate the coupling strength (α) on the shell morphology. For large values of α a bowl-like shape is observed throughout the chemical cycles without recovering its initial spherical morphology. We hypothesize that this is due to the high penalty of volume change assigned to the shell. As the shell swells, larger pores are expected that can temporarily increase the shell permeability to the solvent [88]. However, due to the complexity of the problem, the changes in permeability are not considered in this work.

3.5   Discussion

In this article, we study autonomous gel membrane dynamics in closed shells triggered by periodic reduction-oxidation reactions. In particular, we focus on autonomous reduction-oxidation reactions where one of the components is immobilized into the shell modifying the microenvironment allowing for swelling and deswelling responses.

Our model is an extension of the reference metric remodeling approach used for thin elastic plates [65], [66] to account for chemo-mechanical feedback-loops. Using the two-fluid model approach [47]–[49] we relate the target metric changes to the response of polymer gels to chemical reactions. Using this approach we find that experiments in polymeric shells [56] can be explained by a small variation in the gel thickness (Fig. 3.4). In addition, we incorporate the chemical concentration changes due to mechanical deformations. We note that this approach differs from other thin shell models [89], [90] that do not account for the geometrical feedback into the chemical response. However, the three-dimensional (3D) membrane gel model does consider mechanical

feedback in hydrogels [91], [92]. We find that mechano-chemical feedback loops are important to generate autonomous patterns (Fig. 3.5).

Lastly, we investigate future material design by coupling the material properties to the chemicals. We find that in silico multi-responsive materials can generate a wide variety of shapes in response to mechanical perturbations through changes in the chemical concentrations (Fig. 3.6C-D). Our work inspires the design of mechanical stimulated materials [93], [94] and responsive shells to enhance the functionality of micrompartements [95] and of nanoreactors [96] that enhance catalytic activity. For example, one could in principle design catalytic microcompartments that can expand and contract to absorb or release components at a specific frequency that is favorable for processes that happen inside of the microcompartment.

3.6 Supplementary Information

3.6.1 BZ reaction

The kinetics of the BZ reaction can be understood by the mechanism of Field, Koros, and Noyes [97] (FKN) model with tens of essential steps responsible for the oscillation. Field and Noyes have reduced the reactions to five essential steps, called Oregonator model which can be written as [79], [80]

$$BrO_3^- + Br^- \xrightarrow{k_1} HBrO_2 + HOBr$$

$$HBrO_2 + Br^- \xrightarrow{k_2} 2\,HOBr$$

$$BrO_3^- + HBrO_2 \xrightarrow{k_3} HBrO_2 + 2\,Ru(bpy)_3^{3+}$$

$$2\,HBrO_2 + Ru(bpy)_3^{3+} \xrightarrow{k_4} BrO_3^- + HOBr$$

$$BrMA + Ru(bpy)_3^{3+} \xrightarrow{k_5} fBr^-,$$
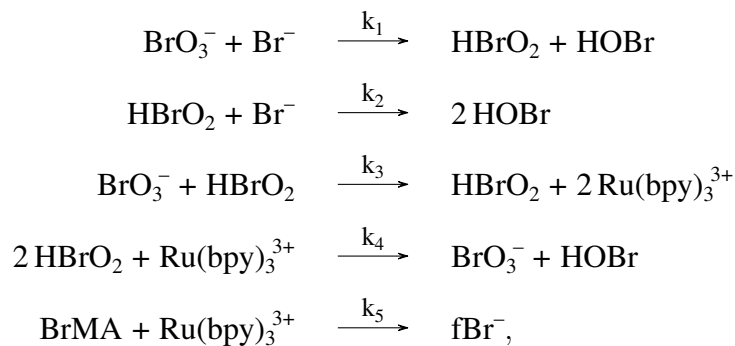
where k_1-k_5 are the rate constants with value described in Table 3.1 [98], [99]. The dimensionless rate equations can thus be written as [80]

$$\epsilon \frac{du}{dt} = qw - uw + u - u^2 \tag{3.5}$$

$$\frac{dv}{dt} = u - v \tag{3.6}$$

$$\epsilon' \frac{dw}{dt} = -qw - uw + fv, \tag{3.7}$$

where u, v and w are the dimensionless variables denoting the concentration of the reactant $[\text{HBrO}_2]$, the oxidized catalyst $[\text{Ru(bpy)}_3^{3+}]$ and the bromide $[\text{Br}^-]$. The dimensionless variables ϵ, q are defined through rate constants and reservoir concentration $q = \frac{2k_1k_4}{k_2k_3}$, $\epsilon = \frac{k_5[B]}{k_3[A]}$, where [A] and [B] are the concentration of bromate $[\text{BrO}_3^-]$ and organic species $[\text{BrMA}]$ respectively, and f is the stoichiometric factor lies in the region $(0.5, 1.0)$. Due to the short time scale of Eq. 3.7, w can be replaced by its stable value with $w = \frac{fv}{q+u}$, and thus the Eqs. 3.5-3.7 can be further simplified as shown in eq. 3.2 where we have included the diffusion of u on the two dimensional manifold; the diffusion of v is not considered based on the fact that catalysts are anchored on the polymeric shell. In the simulations, we chose $[\text{H}^+]$ = 0.7M, [A] = 0.2M, [B] = 0.025M based on recent experiments [56], [81], which defines the parameters $\epsilon = 0.018$ and $q = 0.0008$. We note that in our simulations we used $q = 0.008$ instead due to the high-cost of computing time, where the morphology dynamics remains unchanged.

3.6.2   Target area growth calculation

The total free energy density of a chemically active polymer hydrogel is given by $U_{tot} = U_{elastic} + U_{mix} + U_{chem}$. Terms $U_{elastic}$ and U_{mix} are given by eq. 1.25 and eq. 1.26 respectively. The term

Table 3.1: Rate constants in BZ reaction.

Rate Constant	Value
k_1	$2\,\mathrm{M}^{-3} \cdot \mathrm{s}^{-1} \cdot [\mathrm{H}^+]^2$
k_2	$10^6\,\mathrm{M}^{-2} \cdot \mathrm{s}^{-1} \cdot [\mathrm{H}^+]$
k_3	$10\,\mathrm{M}^{-2} \cdot \mathrm{s}^{-1} \cdot [\mathrm{H}^+]$
k_4	$2 \times 10^3\,\mathrm{M}^{-1} \cdot \mathrm{s}^{-1}$
k_5	$1\,\mathrm{M}^{-1} \cdot \mathrm{s}^{-1}$

U_{chem} that models the chemical process is essentially the same as U_{photo} described in chapter 2 but for the sake of clarity U_{chem} is defined here again as [47]–[49]

$$U_{chem} = \frac{k_B T}{v_m} \left[\lambda v_c \left(1 - \phi \right) \right], \tag{3.8}$$

where λ is a coupling coefficient and determines the extent of swelling/shrinking caused due to the chemical reaction. A positive value of λ causes the hydrogel to shrink and a negative value leads to swelling. v_c is the normalized concentration of the chemical species that changes the hydrophobicity/hydrophilicity of the hydrogel.

The constitutive model was solved using COMSOL's hyperelastic material module. To understand the growth of the material with changing v_c, we plotted the growth ratio (M) of a hydrogel disk as a function of increasing chemical concentration v_c for various values of gel's elastic stiffness (Fig. 3.7). We initialized our hydrogel disk (at $v_c = 0$) to be in equilibrium with the solvent bath and then gradually increased v_c while tracking the steady state volume of the swelling disk. The λ parameter in the U_{chem} term is held constant for the finite element calculation.

It can be seen from Fig. 3.7 that for the comparatively stiffer gels, the growth ratio M becomes more linear with respect to increasing v_c. Therefore, for small changes in v_c, the growth ratio M can be assumed to be a linear function of v_c, that is, $M = 1 + \alpha\, v_c$ and the slope α changes as the stiffness of the material changes. Similarly, α also differs for different values of the λ parameter.
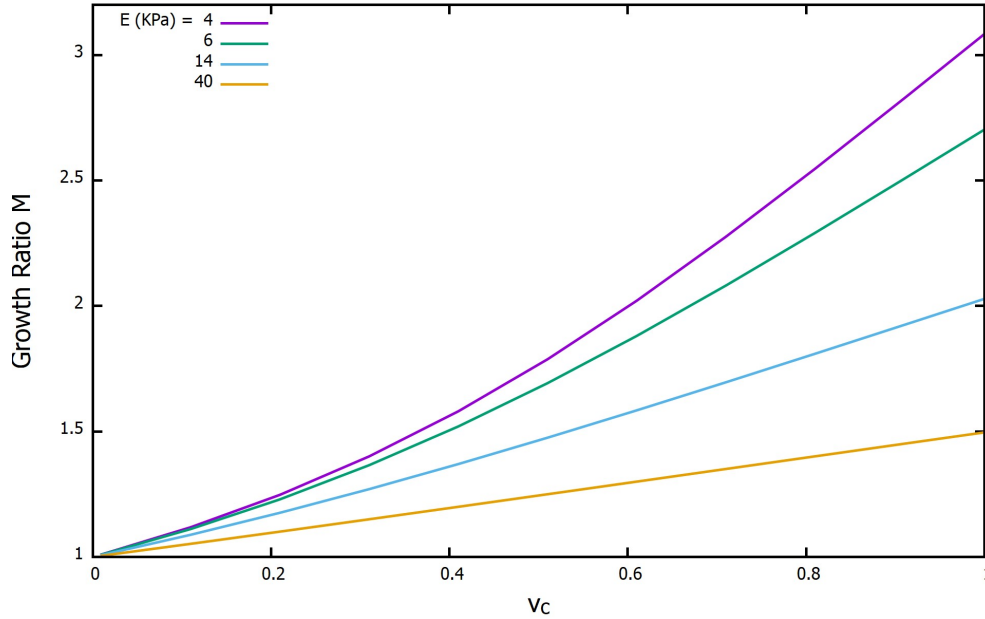
Figure 3.7: Plot of the growth ratio M as a function of v_c. The plot demonstrates that for small variations in v_c the growth is almost linear especially for gels with Young's modulus E $\gtrsim 10\,\mathrm{kPa}$

.

The finite element calculations can be used to quantitatively calculate the dependence of α on the intrinsic parameters of the hydrogel.

For the purpose of the simulations (Fig. 3.7), we chose the value of $\lambda = 0.02$ and $N_x = 10^5$ ($E = 4\,\mathrm{kPa}$), 7×10^4 ($E = 6\,\mathrm{kPa}$), 3×10^4 ($E = 14\,\mathrm{kPa}$) and 10^4 ($E = 40\,\mathrm{kPa}$). The value of the Flory-Huggins interaction parameter χ was calculated using the equation 2.9 where we used a value of $\phi_0 = 0.05$. We note that in the main text simulations we choose $\alpha = 1.0$ for $\lambda = 0.15$ and Young's Modulus $E = 1\,\mathrm{MPa}$, where thermal fluctuation effects on the shell morphology are minimal. In the case of soft gels, we find that thermal fluctuations are important when the diffusion coefficient of the chemical reaction is small such as the values used in figs. 3.6A and 3.6B.

3.6.3 Discretization

Discrete model of thin shell elasticity

We discretize the shell to triangular lattice with the stretching energy written as

$$E_s = \frac{1}{8} \sum_T \frac{Eh}{1 - \nu^2} \sqrt{\bar{g}} \left[\left(Tr[\bar{g}^{-1}g - I] \right)^2 + 2(\nu - 1) \det[\bar{g}^{-1}g - I] \right], \tag{3.9}$$

where $\bar{g}$ (g) is the target (actual) metric of the discretized triangle and I is the identity matrix. E and h are the 3D Young's modulus and thickness of the shell, respectively, and $\nu = \frac{1}{3}$ is the Poisson ratio. For a homogeneous growing shell, the stretching energy and force can be estimated with the mesh triangle angles preserved where $E_s^h = \frac{1}{4} \frac{Eh}{1-\nu} \sum_T \frac{\Delta A^2}{A_g}$ and $F_s^h = \frac{Eh}{\nu-1} \frac{4\pi}{N_v} \frac{r^2 - r_g^2}{r_g^2} \overrightarrow{\mathbf{r}}$, with N_v the total mesh vertex number, and r (r_g) the actual (target) radius of shell (see [7, SI Appendix, section S3A]). With stretching energy dominant, the shell is relaxed to release the stress with relaxation time $\frac{(1-v)\gamma N_v}{8\pi Eh}$, which is inversely proportional to the Young's modulus.

The bending energy can be discretized using Itzykson discretization [100], with

$$E_b = \sum_j \left(\frac{1}{2} \kappa_j \left(H_j - 2H_0 \right)^2 + \kappa_j^g G_j \right) A_j, \tag{3.10}$$

where $H_j = \frac{\text{sign}}{A_j} \left| \frac{1}{2} \sum_T \left(\cot\theta_l \mathbf{r}_{jk} + \cot\theta_k \mathbf{r}_{jl} \right) \right|$ and $G_j = \frac{1}{A_i} (2\pi - \sum_T \theta_i)$ are the mean curvature and gaussian curvature of vertex j, respectively. $A_j = \frac{1}{8} \sum_T \left(\cot\theta_l r_{jk}^2 + \cot\theta_k r_{jl}^2 \right)$ is the dual-lattice area of vertex j, $\kappa = \frac{1}{12} \frac{Eh^3}{1-\nu^2}$ and $\kappa^g = (\nu - 1)\kappa$ are the bending rigidity and gaussian bending rigidity correspondingly. T is the neighbor triangles of vertex j and θ_j is the angle of vertex j on triangle T.

Chemical reaction

The chemical reactions (Eq. 3.2) are evolved on the shell by explicit time integration following the procedure

$$U^{n+1} = A_c(U^n + dtD_U\Delta_M U^n + dtF(U^n)), \tag{3.11}$$

where the Laplace-Beltrami operator (Δ_M) is implemented through DEC method [101] and the chemical concentration is rescaled by the vertex area fraction $A_c = \sqrt{g}^n/\sqrt{g}^{n+1}$ [102], see [7, SI Appendix, section S2] for more details. D_U is the diffusion coefficient of chemical U. At each time step, we couple the target metric to the catalyst concentration (v) with $\bar{g}_{\alpha\beta} = (1 + \alpha\, v(r,t))\bar{g}_{\alpha\beta,t=0}$ following the fact that the target metric is modified subject to the hydrophilicity change of polymers, where α is the coupling coefficient depending on the intrinsic properties of the hydrogel. A detailed discussion about the growth ratio is shown in section 3.6.2 using gel theory, which is linearly dependent on the catalyst concentration at a small amount of chemicals changes.

In the simulation system, the BZ chemical reaction is measured in units of $\tau = 1/(k_3[A])$ where k_3 is a rate constant and $[A]$ is the concentration of a chemical substrate. The thickness and radius of the shell are measured in units of a and the elastic relaxation has time unit $\tau_{elastic} = \gamma/(Ea)$, which is significantly small compared to the chemical reaction. The quantity and units of the other parameters are shown in table 3.2.

Table 3.2: Quantities used in the simulations

Symbol	Description	Value in real units
a	system length unit	$1\,\mu\text{m}$
h	shell thickness	$0.1\,\mu\text{m}$
R	shell radius	$10\,\mu\text{m}$
E	3D Young's Modulus	$1\,\text{MPa} = 2.433 \times 10^8\,\text{k}_\text{B}\text{T}/\mu\text{m}^3$
γ	friction coefficient	$0.02\,\text{Pa}\,\mu\text{m}\,\text{s} = 4.866\,\text{k}_\text{B}\text{T} \cdot \text{s}/\mu\text{m}^2$
τ	chemical time unit $\left(\frac{1}{k_3[A]}\right)$	$1.4\,\text{s}$
$\tau_{elastic}$	elastic time unit $\left(\frac{\gamma}{Ea}\right)$	$2 \times 10^{-8}\,\text{s}$
T	temperature	$298\,\text{K}$
D_u	diffusion coefficient of chemical u	$1 \times 10^3\,\mu\text{m}^2/\text{s}$

CHAPTER 4

FAST AND PROGRAMMABLE LOCOMOTION OF HYDROGEL-METAL HYBRIDS UNDER LIGHT AND MAGNETIC FIELDS

4.1 Abstract

An enormous challenge for science is the design of soft matter in which internal fuels or an external energy input can generate locomotion and shape transformations observed in living organisms. Such materials could assist in productive functions that may range from robotics to smart management of chemical reactions and communication with cells. In this context, hydrated matter that can function in aqueous media would be of great interest. We report here on the design of hydrogels containing a scaffold of high aspect-ratio ferromagnetic nanowires with nematic order dispersed in a polymer network that change shape in response to light and experience torques in rotating magnetic fields. The synergistic response enables fast walking motion of macroscopic objects in water on either flat or inclined surfaces and also guides delivery of cargo through rolling motion and light-driven shape changes. The theoretical description of the response to the external energy input allowed us to program specific trajectories of hydrogel objects that were verified experimentally.

4.2 Introduction

The design of hydrated soft matter that responds to external stimuli with motion and shape changes inspired by living organisms remains an enormous scientific challenge. Design of hydrated structures and mechanisms to achieve this objective may be eventually useful for the development of materials with locomotive capacity for novel aqueous chemistry or to augment the functions of living systems [53], [103], [104]. Pursuing this objective with magnetically actuated soft matter is particularly attractive since magnetic fields can safely penetrate most materials, including biological matter. In previous work it has been shown that magnetic fields can remotely bend metallic backbones and induce walking [105], activate locomotion of particle filaments [106], [107], and induce motion of elastomeric materials that contain ferromagnetic components [5], [21], [108]–[110]. In these elastomeric materials, specific patterns of magnetization and object geometry were generated by various fabrication techniques. However, once these samples have been prepared, the responsive magnetization profile is static and cannot be reconfigured in the absence of a magnetic field. The magnetic components widely used in previous work were spherical and irregularly shaped magnetic particles (such as iron oxide and NdFeB) that lack magnetic anisotropy [5], [21], [109], [110], and thus require a high loading of magnetic material or the use of strong fields to activate significantconsiderable responsiveness. The matrices used to embed these particles have been hydrophobic polymers [111], elastomers [5], [21], or particles were supported on rigid silicon nitride membranes [108]. Hydrogels offer the possibility to function in water and also have the capacity to exchange fluids with aqueous environments [112]. Previous work on macroscopic hydrogels has shown bending, walking or swimming behavior activated by light [1]–[3], thermal [4], chemical [8] or electrochemical stimuli [113], but all of these systems display slow actuation kinetics for locomotion unless they were scaled down to the micrometer scale [114]. Incorporation

of functional nanoscale components into hydrogels provides a powerful strategy to generate emergent properties and performance [115]–[117]. By incorporating high aspect-ratio Ni nanowires into a photoactive hydrogel, we report here on the development of anisotropic hydrogel–metal hybrid materials that are actuated by magnetic fields after exposure to light that also remain reconfigurable by light to alter their magnetic response. We theoretically predict the response of the hybrid objects to light and magnetic fields enabling the programming of their trajectories under water and gait on the fly.

In addition to magnetically driven actuation described above, light as a stimulus is also useful since it can be delivered to synthetic matter remotely and potentially in localized fashion [118]. Previous investigators have incorporated different photoactive components such as photothermal agents [111] and molecular photoswitches [119] into hydrogels to fine-tune their chemical and physical properties. Molecular photoswitches are unique because they can be wavelength-selective and reversibly reconfigure conformations upon irradiation. Recent examples of light responsive materials include polymer films containing cis-trans azobenzene switches [22] and hydrogels based on spiropyran chemistry [2], [3], [23], [39] or molecular motors [24], [25]. Soft materials capable of responding to both light and magnetic fields can initiate the exploration in soft matter of the multisensory interactions we observe in living organisms [111]. In this work we designed and synthesized hydrogel objects that perform distinct tasks with remote control over geometry, stiffness, and magnetization using a combination of light and magnetic fields. The samples are prepared by incorporating aligned high-aspect-ratio ferromagnetic nanowires into a photoactive hydrogel matrix that is capable of changing shape in response to light. Macroscopic bending of the hydrogel upon light irradiation deforms existing magnetization profiles which results in complex three-dimensional magnetization that leads to programmable actuation. These hydrogels can perform functions such as walking, steering, climbing, and delivering cargo under the control of

an external magnetic field and light. Furthermore, small changes in the chemical structure of these systems change the kinetics of light response and thus provide access to a broader range of actuating behaviors.

4.3 Design of the dual-responsive hydrogel-metal hybrid

4.3.1 Synthesis

To synthesize the hydrogel–metal samples, nickel (Ni) nanowires were added to a solution containing monomers, crosslinking agents, initiators and a polymerizable photo-switching spiropyran monomer in order to create a light-responsive crosslinked network (figs. 4.1A and see [6, fig. S2 and methods] for synthetic details). Under dark and acidic conditions, the photoswitch contains a hydrophilic protonated merocyanine (MCH$^+$) moiety that isomerizes to a hydrophobic spiropyran (SP) form upon exposure to visible light. This isomerization with light exposure results in contraction of the hydrogel due to dehydration, followed by expansion under dark conditions. The ferromagnetic nanowires were aligned under a static magnetic field and then fixed in this configuration by free-radical photopolymerization of the light-responsive hydrogel (fig. 4.1A, 4.1B and [6, figs. S3-4]). Small angle x-ray scattering (SAXS) confirmed the alignment of the nanowires, as shown by the radial integration of a 2D scattering intensity plot (fig. 4.1C). We measured a remnant magnetization of $260emu/cm^3$ parallel to the alignment of the nanowires and the coercive magnetic field required to reverse the magnetization of the sample was found to be $25mT$ (fig. 4.1D). This is a 1.9-fold enhancement in the coercivity over bulk nickel (13 mT) [120], highlighting the utility of the shape anisotropy derived from the nanowire architecture ($\sim 8\mu m$ long on average and 200 nm in diameter). In comparison, magnetization loops measured perpendicular to the alignment direction were noisy and exhibited a much lower magnetization, demonstrating the magnetic anisotropy of the composite material. Samples containing randomly oriented Ni

nanowires did not show any macroscopic magnetic anisotropy [6, fig. S5]. Also, when spherical Ni nanoparticles formed chained clusters during photopolymerization under a magnetic field, we did not detect any anisotropy since each individual particle can rotate to align its magnetization with the field [6, fig. S6]. The magnetic anisotropy of the Ni nanowires was also confirmed by superconducting quantum interference device (SQUID) magnetometry with a rotating stage [6, fig. S7]. This indicates that the shape of Ni nanowires is a critical structural feature responsible for the anisotropic magnetic properties of the Ni-hydrogel composites.

4.3.2   Response to light

The as-prepared hydrogel materials were soaked in acidic water for 40 min to obtain an equilibrated swollen state prior to photo-actuation experiments in a large water bath ($\sim$ 100 mL) that contained 5 mM HCl. Upon light exposure, this swollen state underwent a shrinkage to 84% of its original volume [6, fig. S8]. Since the actuation occurs in acidic water, the SP1 hydrogel is capable of sequential actuation cycles that did not require additional HCl preconditioning. We found that the flat hydrogel object bends towards the light source upon irradiation from one side and recovers its original flat geometry in the dark. This bending–flattening process is highly reversible, and the hydrogel could maintain its photoactivity with the same maximum bending angle over at least ten cycles by switching the light on and off [6, fig. S9]. Fig. 4.1E (left) shows the calculated water concentration gradient within a hydrogel after exposure to light based on the material model discussed in section 4.4.

4.3.3   Response to magnetic field

The deformed light-induced bent geometry leads to a nonuniform 3D magnetization profile of the magnetic nanowires (indicated by the magenta arrows) with respect to the applied magnetic field.

This change enables the arch-shaped hydrogel to respond to a spatially uniform external magnetic field B_{ext}, but remains completely unresponsive in its flat state. Thus, the span of the arch-shaped hydrogel can be increased or decreased by simply applying a static magnetic field parallel or anti-parallel to the nanowires' alignment direction (fig. 4.1E, right).

4.4   The continuum model of the dual-responsive hydrogel-metal hybrid

The dual-responsive hydrogel has two components i.e. a photo-responsive component due to the presence of spiropyran photoswitches and a magneto-responsive component due to the presence of nickle nanowires. The continuum model used to analyse the photoactivity of the spiropyran hydrogel has been extensively discussed in chapter 2 of this thesis. Here, we will build on top of that model and discuss the implications of the presence of nickle nanowires in the hydrogel.

Firstly, the presence of nickle nanowires makes the elastic response of the hydrogel anisotropic as the wires are all aligned in the same direction. The hydrogel will be stiffer along the direction of the fibers compared to the direction perpendicular to the fibers. In order to describe the anisotropic elastic response of the hydrogel, we assume that the hydrogel is transversely isotropic and its elastic response can be described by the standard reinforcement model [121]. Then, corresponding elastic energy density function can be written as:

$$U_{reinforced} = \frac{1}{2}G\left(\sum_i \lambda_i^2 - 3\right) + \frac{1}{2}\gamma G(\mathbf{A}.\mathbf{C}\mathbf{A} - 1)^2 \tag{4.1}$$

where G is the shear modulus; γ is a stiffness parameter which characterizes the reinforcement ($\gamma > 0$) [122]; $\mathbf{A}$ is the direction of the nanowires and $\mathbf{C}$ is the right Cauchy-Green tensor. Notice the first term is the same as $U_{elastic}$ described in chapter 1 eq. 1.25 and the second term can
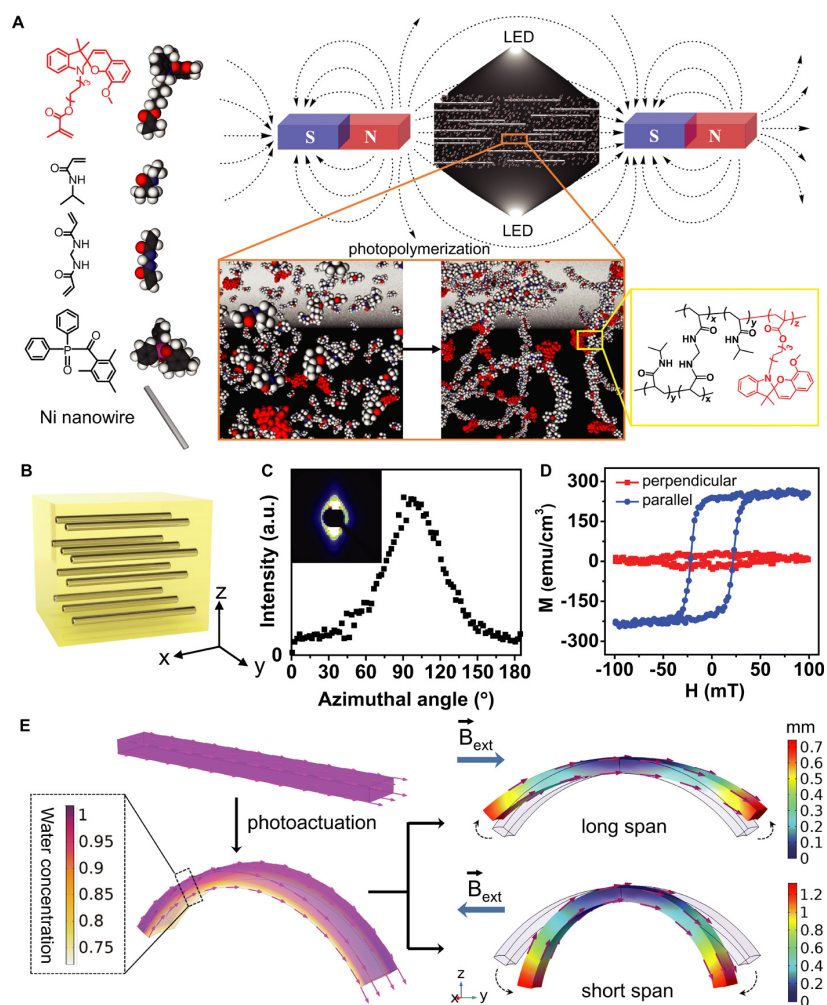
Figure 4.1: Hydrogels designed for coupled response to light and magnetic fields. (A) Schematic of Ni nanowires aligned and fixed within a hydrogel network containing photoactive SP moieties using a uniform magnetic field during free radical photopolymerization. (B) Schematic representation of aligned Ni nanowires (gray) immobilized in a hydrogel network (yellow). (C) Radial integration of 2D SAXS pattern (inset) revealing the macroscopic alignment of Ni nanowires within the hydrogel. (D) Magnetization loops parallel and perpendicular to the alignment axis of the nanowires. (E) Finite element calculation of the water concentration gradient and deformation in a slab of hydrogel exposed to light (left); finite element calculation of deformation as a result of magnetic field exposure in a hydrogel slab previously bent by light (right). Magenta arrows denote the magnetization of Ni nanowires; blue arrows indicate the direction of the external magnetic fields; dashed arrows represent the movement of both ends after applying magnetic fields; rainbow surface colors represent the deformations relative to its initial configurations (shaded regions).

henceforth be labeled as U_{aniso} i.e.

$$U_{aniso} = \frac{1}{2}\gamma G(\mathbf{A}.\mathbf{CA} - 1)^2 \tag{4.2}$$

Therefore, the total free energy of the hydrogel material in the absence of magnetic field is now given by $U = U_{elastic} + U_{mix} + U_{photo} + U_{aniso}$ (eqs. 1.25, 1.26, 2.7 and 4.2).

Second implication of having nickle nanowires embedded into the hydrogel is that it makes the hydrogel responsive to magnetic field. An external magnetic field induces local torques since Ni nanowires prefer to align with the field. Given that the nanowires are immobilized by the hydrogel, these magnetic torques transmit stresses that collectively result in macroscopic deformation of the material. The free energy density function of the fiber-reinforced magneto-elastic materials is given by

$$U_{magneto-elastic} = U_{elastic} + U_{aniso} + U_{mag} \tag{4.3}$$

where the term U_{mag} is given by

$$U_{mag} = - (\mathbf{FM}) \cdot \mathbf{B} \tag{4.4}$$

Here $\mathbf{B}$ is the magnetic flux density; $\mathbf{F}$ is the deformation gradient tensor and $\mathbf{M}$ is the magnetization of the material in the reference configuration. Notice that the magneto-elastic model used for the hydrogel does not contain the U_{mix} term. This is a reasonable approximation because over the small time scales of magnetic actuation, no (or very little) fluid leaves the hydrogel (which is a much slower process), thereby making the U_{mix} term of the hydrogels free energy a constant. Therefore, U_{mix} does not contribute to the total stress on the material. Since the time scale over which the geometry deforms due to light ($\sim$ 5-10 minutes) is much larger than the time scale for

deformation due to magnetic field ($\sim$ 1-2 seconds), we can treat the photo-responsive and magneto-responsive natures of the hydrogel independently. This allowed us to solve the model of the dual responsive hybrid metal-hydrogel in two steps. We first used the photo-responsive hydrogel model with reinforcement to calculate the light induced deformed geometry and then used this resultant geometry as the input shape for the magneto-elastic model (eq. 4.3).

The magnetic energy term U_{mag} corresponds to the magnetic stress tensor $\boldsymbol{\sigma}_{mag} = \frac{1}{J} \frac{\partial U_{mag}}{\partial \mathbf{F}} \mathbf{F}^T$. This model demonstrates a clear coupling between light and magnetic actuation via elastic deformation. With light exposure, the light propagates through the hydrogel and creates differential shrinking, which induces macroscopic deformations ($\mathbf{F}$) of the hydrogel and enables the light actuation. Since the Ni nanowires are trapped within the hydrogel, the elastic deformation will change the spatial orientation of Ni nanowires ($\mathbf{FM}$). This change in Ni nanowire orientation ultimately modifies magnetic actuation ($\boldsymbol{\sigma}_{mag}$). In this model, the nickel nanowires move with the hydrogel without slipping and the higher order energy contributions in $\mathbf{B}$ to the free energy density are ignored [21]. The strength of external magnetic field stays in the linear response region of Ni nanowires [6, fig. S10] and all elastic parameters are calibrated from experimental measurements [6, fig. S11]. This continuum model was solved using the finite element method and the implementation details are discussed in Appendix A. This provides a quantitative analysis for the dynamic behavior of the hydrogels in magnetic fields.

4.5   Programmed walking and steering motions

To develop robotic functions, we prepared cross-shaped hydrogel films containing aligned Ni nanowires (fig. 4.2A). The film thickness was fixed around 0.5 mm to obtain an optimal photoisomerization speed and deformation stability based on our previous results [39]. After light irradiation, the flat sample bends up as an object with two walking legs (w1, w2) and two stabiliz-

ing arms (s1, s2) (fig. 4.2B). The alignment of the wires within the object creates an anisotropic mechanical response, and therefore, the span between w1 and w2 (see front view) is larger than that between s1 and s2 (see side view). We calculated photo-actuation of these samples using the model described before and generated the green wireframes shown in fig. 4.2B. The wireframes overlap exactly with the actual bending geometry of the hydrogels, observed from both front and side views, suggesting clear agreement between the calculated and actual light-induced deformation observed in the photographs. It is therefore possible to exploit this mechanical anisotropy [6, figs. S13 and S14] caused by the aligned Ni nanowires to modulate photo-actuation in hydrogel samples with simple geometries such as squares [6, fig. S15]. We found that when the hydrogel-metal hybrids are illuminated and bent by the light, a nonuniform 3D magnetization profile is established that enables walking under the influence of an external rotating magnetic field (Fig. 4.2C and [6, movie S1]). As a control, samples containing unaligned Ni nanowires or aligned chains of Ni nanoparticles exhibited minimal movement under the same magnetic field and were not capable of walking [6, fig. S16]. The average magnetization (purple arrow) and the external magnetic field (blue arrow) lie within the y-z plane, and the magnetic torque density is given by $\boldsymbol{\tau}_{mag} = \mathbf{FM}/J \times \mathbf{B}$. Therefore, only the x component of the magnetic torque is a nonzero quantity. The rotating magnetic field in the y-z plane generates an oscillatory x component of the magnetic torque that causes the objects to rotate alternately clockwise and counterclockwise around the x axis (perpendicular to the walking direction) (fig. 4.2D). Because of the combination of magnetic torque and gravity, the object lands on its front and back legs in alternating fashion (fig. 4.2C). Our model assumes that the friction between the legs and the floor is large enough to avoid slippage during walking (see section 4.5.1 for the boundary conditions used in finite element calculations). Magnetoelastic coupling results in a periodic change in the hydrogel's leg span (distance between w1 and w2) (Fig. 4.2 D and E), which enables the net displacement of the hydrogel along the

y axis. Furthermore, longer side arms were found to be important in stabilizing the hydrogel's movement and optimizing its lift during walking because of a larger magnetic torque [6, fig. S17 and movie S2]. Also, the walking speed was found to be faster with higher frequencies (0.3 to 0.7 Hz) or stronger magnetic fields (11.5 to 16.0 mT) (fig. 4.2F). With a fixed frequency (0.7 Hz) and field strength (14.5 mT), it was possible to achieve walking over macroscopic distances ($\sim$53 mm) (fig. 4.2G) and reduction of the hydrogels to millimeter-size scales did not change the mechanism of motion [6, movie S4].

The hybrid hydrogels can also achieve steering motion in arbitrary directions while walking along the x-y plane by controlling the applied magnetic field to produce an additional torque in the z direction (i.e., normal to the walking plane). Using simulations, we predicted that the objects could turn 90° in 30° increments (fig. 4.3A) by programming the applied field in the x, y, and z directions to achieve the required torque (fig. 4.3, B and C). The predicted motion using simulations was observed experimentally as shown in fig. 4.3A. The two modes of motion (walking and steering) allow our hydrogel sample to reach any arbitrary destination on a 2D level or inclined surface. Figure 4.3D shows a designed arbitrary path with multiple turns, and Fig. 4.3E shows its corresponding experimental realization [6, Movie S6]. We therefore conclude that the experimental samples of these materials can have robotic functions, which in this case involve following continuous paths over macroscopic distances.

4.5.1 Contact boundary conditions

The complete analysis of the contacts between the hydrogel robot and the floor requires the simulation to consider mechanical frictions and contact pressures, which are generally difficult to model in the finite element analysis. In order to keep the essential physics without introducing too much complexities, we assume all contacts are non-slippery during walking. Specifically, it means that
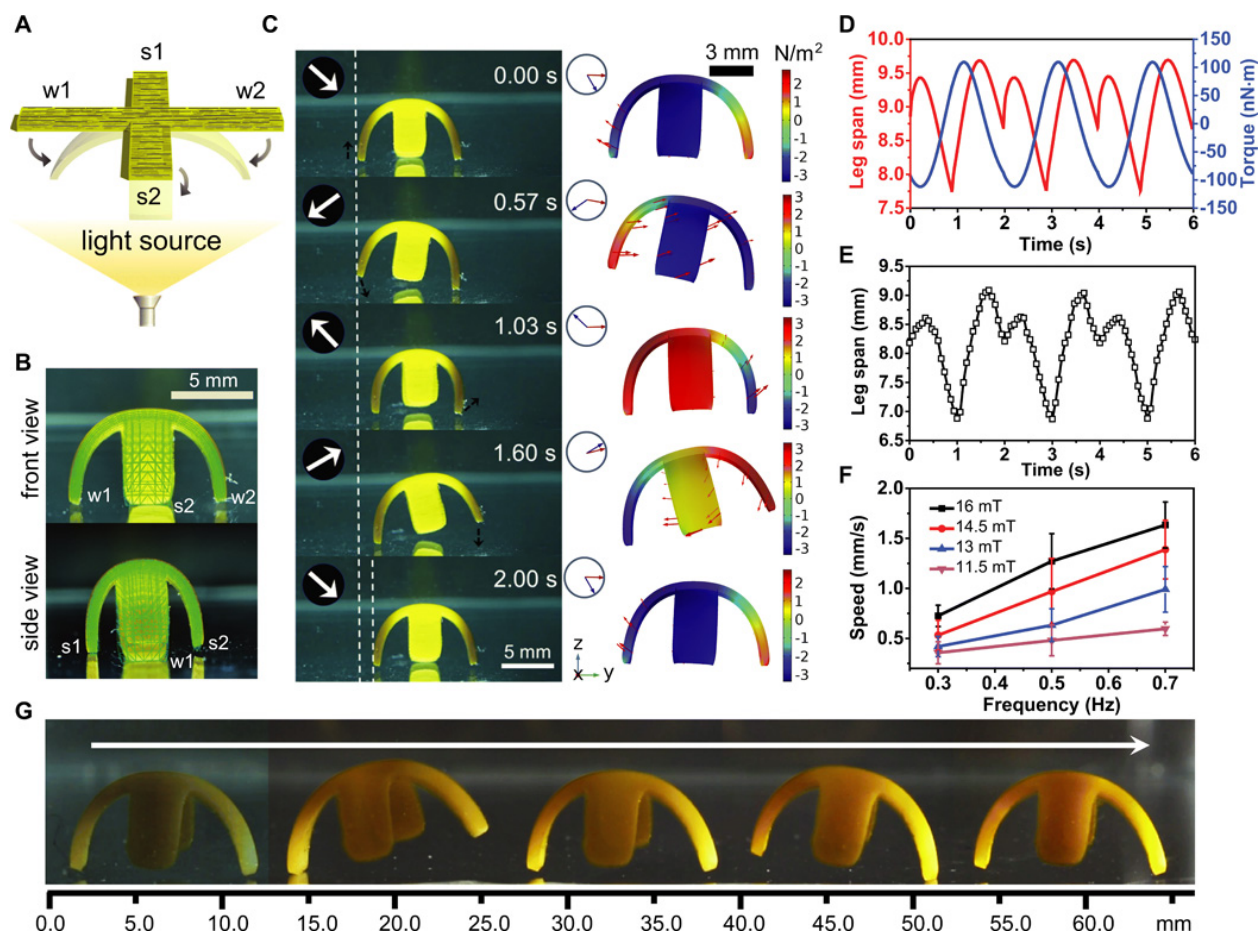
Figure 4.2: Light triggered walking under rotating magnetic fields. (A) Schematic of a cross-shaped hydrogel film containing aligned Ni nanowires irradiated from below. (B) Photographs of the bent hydrogels (front and side views) superimposed with green wireframe representations of the calculated photo-actuation using a finite element method. (C) Left, photographs of the hydrogel walking from left to right for one cycle (white arrows indicate direction of the magnetic fields); Right, calculated snapshots from a finite element simulation of the walking motion (color scale represents the x component of the magnetic torque density). Red arrows indicate instantaneous velocity field, blue arrows indicate direction of the external magnetic field, and magenta arrows indicate direction of the average magnetization. (D) Plot of the x component of the magnetic torque (blue) and leg span (red) from the simulation. (E) Plot of the experimental leg span of samples as a function of time over multiple walking cycles. (F) Plot of the walking speed as a function of rotating frequency at various magnetic field strengths (error bars represent SDs from three separate samples). (G) Time-lapse photographs of hydrogel walking (collected every four cycles, ∼8.3 s) over macroscopic distances under a rotating magnetic field (14.5 mT, 0.7 Hz).
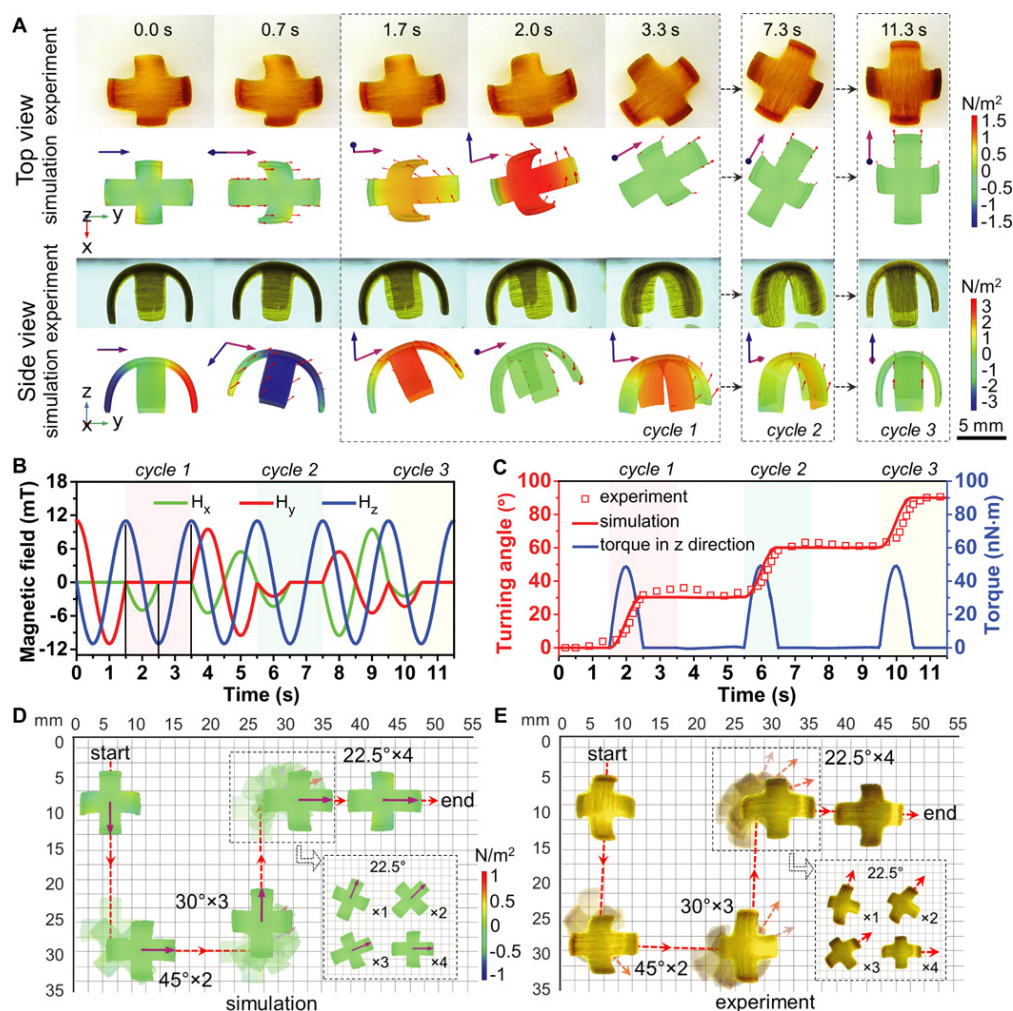
Figure 4.3: Steering motion and path followed by samples under rotating magnetic fields. Snapshots of three periods of steering motion from both experiment and simulation shown in the top view (top) and side view (bottom). Red arrows depict the instantaneous velocity field, blue arrows depict the direction of external rotating magnetic fields, purple arrows depict the direction of the average magnetization, and surface colors represent the z and x components of the magnetic torque density in the top and side views, respectively. (B) The x, y, and z components of the external rotating magnetic fields as functions of time. (C) Turning angle of the hydrogel robot from the experiment (red square) and the simulation (red line) and the z component of the total magnetic torque (blue line). Arbitrary path of the hydrogel from simulations (D) and experiment (E). The surface colors represent the z component of the magnetic torque density; dashed red line indicates the motion trajectory; magenta arrows indicate the direction of the average magnetization. Insets show a 90° turn in four 22.5° increments. "x1," "x2," "x3," and "x4" indicate the number of turning increments made while steering along a 90° turn.

once a leg of the hydrogel robot lands on the floor, the landed leg is not allowed to have translational displacement. However, rotational movement around the center of the landed leg is allowed to give its steering capability. Besides, we assume all contacts are perfectly inelastic collisions, which means that the kinetic energy of the hydrogel robot gets dissipated immediately when a leg lands on the ground. With above assumptions, we track the positions of each legs of the hydrogel robot during the time-dependent simulation and trigger a contact event once any leg hits the floor. For each contact event, the boundary condition of the landed leg is switched as a fixed boundary condition. At the same time, the boundary condition of the other leg is switched as a free boundary condition. The kinetic energy of the hydrogel robot is also dissipated completely during each contact events. This contact event-driven boundary condition allows us to recover the dynamic behaviors of the hydrogel robots observed in the experiment and quantitatively study possible robotic functions of the hydrogel robots.

4.6 Effect of photoswitch chemistry on walking trajectories

To develop more complex robotic functions, we synthesized hydrogels with different molecular photoswitches to tune the kinetics of photo-actuation. Hydrogels made of SP1 can maintain their bending curvature under variable light intensities (96 to 190 mW/cm^2) through the duration of our experiments (fig. 4.4A), confirmed by the change of leg span (fig. 4.4C, black). We also synthesized a photoswitch (SP2) that could be covalently incorporated in the polymeric network, which lacks the methoxy group and displays faster photoisomerization to the closed ring form [6, figs. S18 and S19]. The hydrogel component of the hybrid samples containing SP2 bend and then flatten in response to relatively low light intensities (23.5 to 33.0 mW/cm^2) (fig. 4.4, B and C, red), because prolonged irradiation destroys the initial light-induced hydrophobicity gradient associated with bending of the material. Because the bending angle is highly tunable by changing
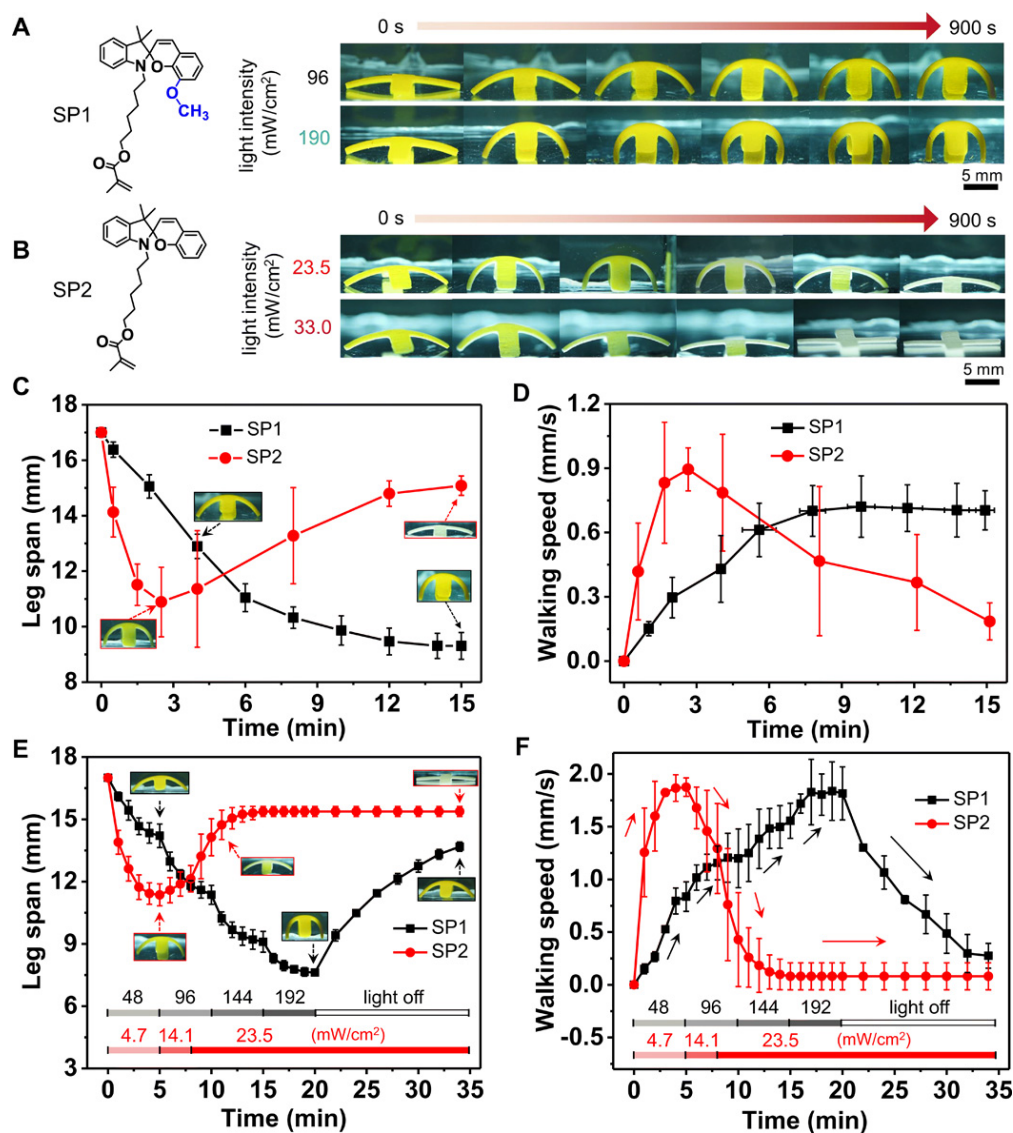
Figure 4.4: Chemical design and bimodal control of the hydrogel robots. (A and B) Molecular structures of SP1 and SP2 and snapshots of the corresponding hydrogel robots under constant light irradiation over 900 s. (C) Leg span and (D) walking speed under irradiation with 96 mW/cm^2 for SP1 and 23.5 mW/cm^2 for SP2 (error bars represent SDs of data collected from three separate samples). (E and F) Variable light intensity applied over 2100 s to program leg span and walking speed, respectively. Black bar, four different light intensities (48, 96, 144, 192 mW/cm^2) were sequentially applied on SP1 samples every 5 min followed by a dark time for 15 min; red bar, three different light intensities (4.7, 14.1, and 23.5 mW/cm^2) were sequentially applied on SP2 samples for 5, 3, and 27 min, respectively.

irradiation conditions [6, fig. S20] and the walking behaviors depend directly on the bending geometry, a permanent walker made of SP1 walks with a constant speed, whereas one made of SP2 gradually loses its walking ability with continuous irradiation (fig. 4.4D, [6, fig. S21 and movie S7]) and is therefore a transient walker. Note that the walking speed of SP2 samples has a large SD, probably because of the rapidly increasing stiffness upon light irradiation [6, fig. S14] as well as some uncontrolled slippage and rotation of the walker. The walking speed can be controlled by programmed sequences of light intensity. As shown in fig. 4.4 (E and F), samples containing SP1 hydrogel were found to bend and walk faster as the light intensity increased. The walking speed of SP1 hydrogels after 10 min of sequential irradiation at low and then higher intensity (see fig. 4.4F) was faster (1.2 mm/s) than the speed after 10 min of exposure to a constant light intensity (0.7 mm/s) (fig. 4.4D). We suggest that light irradiation history leads to variations in bending curvature and mechanical properties. For example, fig. 4.4 (E and F) shows plateaus in leg span and walking speed during the first 10 min. A full understanding of this phenomenon is beyond the scope of this paper, but we can suggest that equilibration rate of structures during irradiation will be sensitively dependent to light exposure history. Also, the SP1 hydrogel was able to selectively bend and its walking accelerated along a section of its path where the light source was localized, offering another possibility for adaptive response to the surrounding environment. This permanent walker gradually stops walking when light is turned off [6, fig. S22], because the bending hydrogel returns to its initial flat geometry and the hydrophobicity gradient disappears. In contrast to the SP1 samples, prolonged light irradiation of SP2 leads to rapid penetration of light and the disappearance of the hydrophobicity gradient through the thickness of samples. Therefore, increasing the light intensity did not cause samples containing SP2 to walk faster but rather accelerated flattening of bent samples [6, fig. S23]. We also found that we can create objects with different walking modes by controlling the alignment direction of the nanowires during preparation of the Ni-hydrogel

composites [6, fig. S24]. Objects with nanowires aligned diagonally relative to their legs exhibited a walking motion by lifting two legs simultaneously under the rotating magnetic field (fig. 4.5A). Objects with nanowires aligned perpendicular to the films walk similarly to those with nanowires in the plane of the film but do not rotate their bodies when the magnetic field is reoriented from the y-z to x-z plane because of the lack of magnetic anisotropy (fig. 4.5B and [6, movie S8]).

4.7   Cargo transport and release

In addition to walking across a flat plane, the hydrogel objects can also climb inclined surfaces (fig. 4.6A) and therefore displayed a different walking speed during the ascending and descending process (Fig. 4.6B). The hydrogel-metal hybrid samples can transport and release cargos using light and magnetic field exposure. Irradiating samples with high intensity light (4800 mW/cm^2) from below caused the hydrogel to curl into a spheroidal object, wrapping around an alginate hydrogel bead (cargo) that had been placed underneath it (fig. 4.6C, top). We point out that substantial photothermal or photobleaching effects were not observed when using this short exposure to high intensity irradiation [6, fig. S25]. The rolling motion of the ball-like object under a rotating magnetic field can be guided to different directions without dropping the alginate bead, allowing delivery of the cargo to any arbitrary destination (fig. 4.6C, middle). By shining light continuously on the convex side of the object, we can eliminate the photoisomerization gradient to flatten the object first, followed by continuous irradiation from the bottom to create an opposing gradient, thus causing the object to bend up and release its cargo (fig. 4.6C, bottom, and [6, movie S10]). In addition to using the rolling motion, our robot was also able to transport cargo using the walking motion. Because the MCH$^+$ is positively charged, the hydrogel robots can transport negatively charged cargo (an alginate bead) adhered to the top of the object through electrostatic attractions and deliver the cargo to any destination by walking and subsequent release by fast spinning (fig.
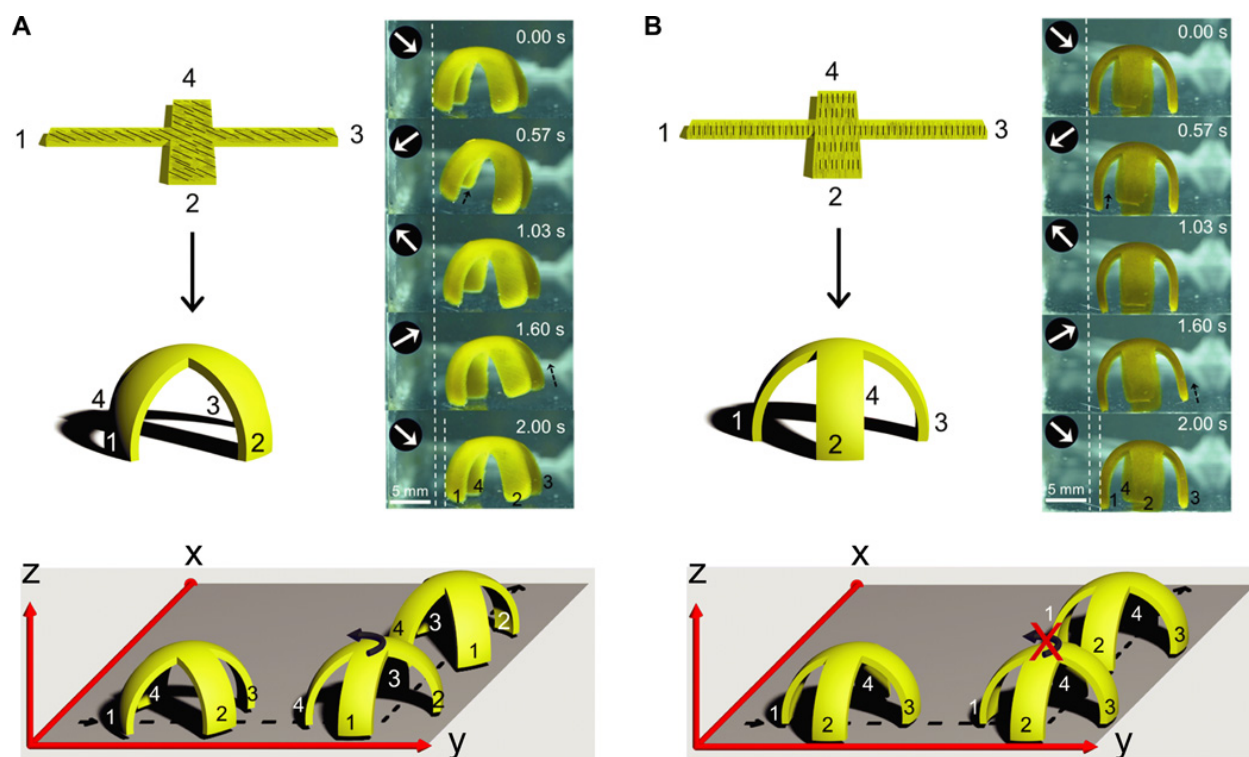
Figure 4.5: Walking modes of the hydrogel robots in response to nanowire orientation. (A) Top, schematic representation of a cross-shaped hydrogel object irradiated from below with the Ni nanowires aligned diagonally, and photographs at different times (indicated at the upper right corner) of the hydrogel robot after irradiation walking from left to right for one cycle by lifting two legs simultaneously (1, 4) or (2, 3); bottom, schematic representation of the object rotating its body 90° counterclockwise when the rotation direction of the magnetic field changes from the y-z plane to the x-z plane. (B) Top, schematic representation of a cross-shaped hydrogel object irradiated from below with the Ni nanowires aligned perpendicular to the thickness direction, and photographs of the robots as in (A) but alternating the lift of legs 1 and 3 (white arrows indicate the direction of magnetic fields, and black dashed arrows indicate the lifting of the robot legs); bottom, schematic representation of the walking hydrogel robot showing that this orientation of the Ni nanowires does not lead to rotation of the robot's body when the magnetic field changes to the x-z plane.

4.6D). These results offer proof of concept on the use of programmed light and magnetic fields to externally and remotely stimulate materials to transport and release cargo.

4.8 Discussion

In this work, we have investigated the design of highly hydrated soft matter with the capability to respond to both light and magnetic fields to emulate locomotion and other functions observed in living organisms. This coupling is achieved by embedding rigid and macroscopically aligned ferromagnetic nanowires in a soft photoactive hydrogel. Compared with conventional polymers or liquid crystal elastomers (LCEs) that have been widely investigated, hydrogels offer great potential in biorelated applications because of their high water content and mechanical similarity to soft tissues. At the same time, the high aspect ratio of the Ni nanowires used to create the experimental materials allows the possibility of aligning the magnetic scaffold of the hydrogels. Thus, these hybrid materials have potential as systems that can be designed to have anisotropic properties. In this context, the common spherical and irregularly shaped magnetic particles (such as NdFeB) used in previous work lack well-defined shapes and magnetic anisotropy. In those earlier systems, a high content of the magnetic component [$\sim$10 weight % (wt %)] or a large magnetic field is required to activate a considerable response. In contrast, a very low content of aligned Ni nanowires (0.5 wt %) is sufficient in the hybrid hydrogels to generate a large magnetic response for robotic functions using a relatively weak magnetic field strength ($\leq$ 16 mT). This advantage is supported by the product of the weight percentage of magnetic material and the applied field strength in our system, which is about three times lower than those used with previous systems. Also, although the responses of our system to light and magnetic fields are driven by different mechanisms, they are interestingly coupled strongly via elastic deformation. The magnetic response depends on the geometry induced by photo-actuation (light direction, intensity, and irradiation time), whereas
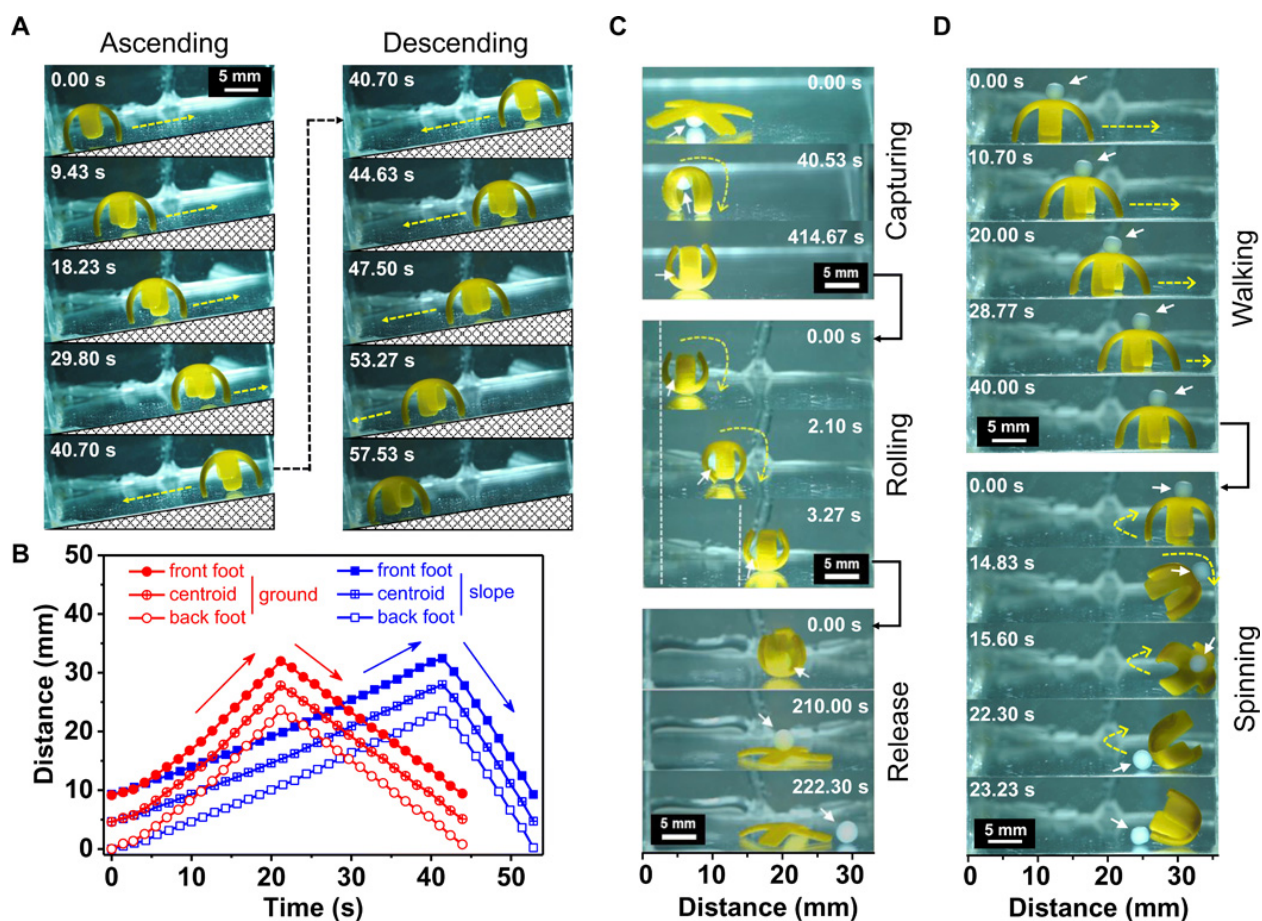
Figure 4.6: Hydrogel robots performing tasks under rotating magnetic fields. (A) Photographs of ascending (left) and descending (right) hydrogel objects containing the SP1 moiety on a glass surface with an inclined angle of 9° and exposed to a magnetic field rotating in the y-z plane (the time at which each photograph was taken is indicated in the upper left-hand corner). (B) Plot of the position of the centroid, front and back feet of hydrogel objects as a function of time when robots walk on an inclined surface (blue) or a flat surface (red) but exposed to the same rotating magnetic field. (C) Starting at the top, sequential photographs (see times at upper right corner) show an alginate bead (white arrow) initially underneath a robot in the flattened state and subsequently captured when light from below bends the robot; the robot is then transported by a rolling motion under a magnetic field; and irradiation from the bottom exposes and releases the alginate cargo. (D) Time sequence photographs (see times at upper left corner) showing an alginate bead initially adhered to the top of a hydrogel object, then transported by walking motion, and subsequently released by fast spinning using the magnetic field.

the magnetic response only appears to affect photo-actuation by changing the object's orientation with respect to incident light [6, fig. S26]. As demonstrated above, chemical changes in the photoswitching molecules can also alter the programmable shape changes upon light exposure and in this way change the magnetically driven robotic functions. The photoswitching approach via molecular isomerization offers the advantage of activation using relatively low light intensity [23], [119], [123]. This is in contrast to the commonly used photothermal agents, which require high intensity light [115], [124], [125].

In miniaturized form, the materials developed in this work could be potentially used to transport and release cargoes in aqueous media through narrow passages with complex routes. In the experiments reported here, a rotating external field precessing at a 90° angle to the walking direction was selected because it maximizes the magnetic torque that drives actuation when the nanowires are aligned along the bending direction of the hydrogel. However, the actuation mechanisms investigated here could be used in the future to explore other modes of locomotion and functions by designing objects with other shapes and fields precessing at other angles with respect to the magnetization of the nanowires. The coupling principle between shape-morphing and responsive actuation developed here provides a general framework to create more complex bioinspired motions and functions.

Given the hydrogel nature of our materials, they can potentially collect molecular components from aqueous solutions and deliver them at another point by expelling water. Future directions could also include developing much smaller objects for drug delivery in tissues or to specific cells. In this respect, our understanding of the synergy between light and magnetic actuation will be important in design geometries suited for swimming and locomotion in low Reynolds number environments [126]. The walking mechanism reported here can occur on any flat or inclined surface without relying on ratchets, which is comparable with previous photothermal [127], thermal [128],

or electrically [129], [130] driven walkers. The walking speed reached in our system ($\sim$2 mm/s) is fast from the perspective of previously observed light-induced locomotion but is comparable with other examples of magnetic actuation. However, we point out that in our system exposure of the objects to photons and the magnetic field are physically inseparable factors in the observed actuation. As we approach the walking speed in biologically relevant systems ($\sim$1 body length per second), the walking speed of our systems ($\sim$0.3 body length per second) is comparable or lower than that of light-actuated robots [114], [131], which is limited by the viscous drag from the liquid environment and surface friction. With increasing walking speed, the viscous drag creates higher resistance forces, and slippage occurs during walking because of insufficient friction with the surface. Given the possibility to match the mechanical properties and water content of molecularly designed hydrogels to those of cells and tissues, these systems may allow us to recreate in synthetic robots the locomotion modes and other actuation behaviors observed in living organisms. We conclude that by theoretically integrating magnetoelasticity, polymer physics, and photochemical kinetics, we learned how to control locomotion and shape changes in soft materials responding to both light and magnetic fields.

CHAPTER 5

CONTROL OF A PHOTOTACTIC HYDROGEL SWIMMER USING LIGHT AND MAGNETIC FIELDS

5.1 Abstract

Similar to living organisms that experience their environment using different sensory mechanisms, we need materials capable of sensing multiple external stimuli. Soft robotic systems that rely on remote control can benefit heavily by the design of such active materials. Functionalized hydrogels that respond to light and magnetic fields allow for such remote multimodal actuation. Here, we design, synthesize and model a soft hydrogel robot that is capable of swimming underwater under the influence of external light and magnetic fields. By coupling the magnetoelasticity and the light induced photochemistry of these hydrogels, we were able to model and predict the response of our hydrogel robot to external fields. We modeled the fluid-structure interaction of the robot to demonstrate its swimming behavior. The unique photochemistry of our material allows our hydrogel robot to also demonstrate phototactic behaviour which is reminiscent of biological matter.

5.2 Introduction

Active materials that can spontaneously respond to changes in their external environment can prove to be extremely useful in the field of soft robotics. Functionalized hydrogels that interact with their

---

chemical surroundings or external fields such as thermal, light, and magnetic fields can help create soft actuators for tetherless robotic systems as they allow for remote control. Materials that respond to multiple stimuli at once are better as these materials can not only perform multiple tasks but also more complex tasks [6]. To direct such soft robots we need to have a control over their shape and elastic properties along with a remote actuation mechanisms. Magnetically actuated soft materials are of particular interest as magnetic fields can penetrate most materials. In this work, we have synthesized a functionalized hydrogel that responds to both light and magnetic fields and used it to construct a soft hydrogel swimmer that can be actuated remotely using magnetic fields with light controlling the properties of the motion. Compared to our previous work [6] presented in chapter 4, this material has much faster response times to photoactuation and due to the material's chemical nature, we can control both its morphology and elasticity using light which was not possible before. The control of the elastic properties of the hydrogel allowed us to introduce phototactic behaviour in our robotic swimmer. In order to describe the interaction of the hydrogel with external light and magnetic fields, we used the continuum modelling approach presented in the previous chapters. In this chapter, we will model the dual-responsive material's interaction with the surrounding aqueous environment to theoretically calculate the swimming motion of the robotic swimmer. We also augment the hyperelastic model presented in chapter 4 to account for the changes in the elastic properties of the hydrogel due to light.

5.3   Finite Element Model

5.3.1   Hyperelastic Material

In chapter 4 we modeled the dual-responsive (light and magnetic field) hydrogel in two separate steps

- Use the hyperelastic model for reinforced photoresponsive gels given by $U_{gel} = U_{elastic} + U_{mix} + U_{photo} + U_{aniso}$ (see equations 1.25, 1.26, 2.7 and 4.2) to calculate the deformed geometry.

- Use the deformed geometry as the initial configuration for the magneto-elastic material model given by $U_{gel} = U_{elastic} + U_{aniso} + U_{mag}$ (see equations 1.25, 4.2 and 4.4)

This was possible due to the large difference in the time scales of the photo-actuation and magneto-actuation. However, this is not the case for the material developed in this chapter. We will therefore have to consider all the energy terms together and thereby construct a '*true*' dual-responsive material model which is given by

$$U_{gel} = U_{elastic} + U_{mix} + U_{photo} + U_{aniso} + U_{mag}$$

$$
\begin{aligned}
U_{gel}(\mathbf{F}) = {} & \frac{1}{2}\frac{k_B T}{v_m N_x}\left(tr(\mathbf{F}^T\mathbf{F}) - 3 + \gamma(\mathbf{A}\cdot\mathbf{F}^T\mathbf{F}\mathbf{A} - 1)^2\right) \\
& + \frac{k_B T}{v_m}\left[(det(\mathbf{F}) - 1)\,ln\left(1 - \frac{1}{det(\mathbf{F})}\right) + (\chi + \alpha r_{sp})\left(1 - \frac{1}{det(\mathbf{F})}\right)\right] - (\mathbf{F}\mathbf{M})\cdot\mathbf{B}
\end{aligned}
$$

$$(5.1)$$

The above continuum model for dual-responsive hydrogel is solved via the finite element method, which when combined with an external precessing magnetic field provides a quantitative description for the motion of the synthesized hydrogel swimmer. The geometry of our model swimmer is illustrated in Fig. 5.1a which shows the hydrogel robot to be 30mm x 5mm and 0.5mm thick with nickle nanowires arranged along the length of the robot. The arrows show the direction of the magnetization, **M**. Fig. 5.1b shows finite element calculations demonstrating three configurations of the swimmer in the external magnetic field, **H**. As the magnetic field oscillates, the
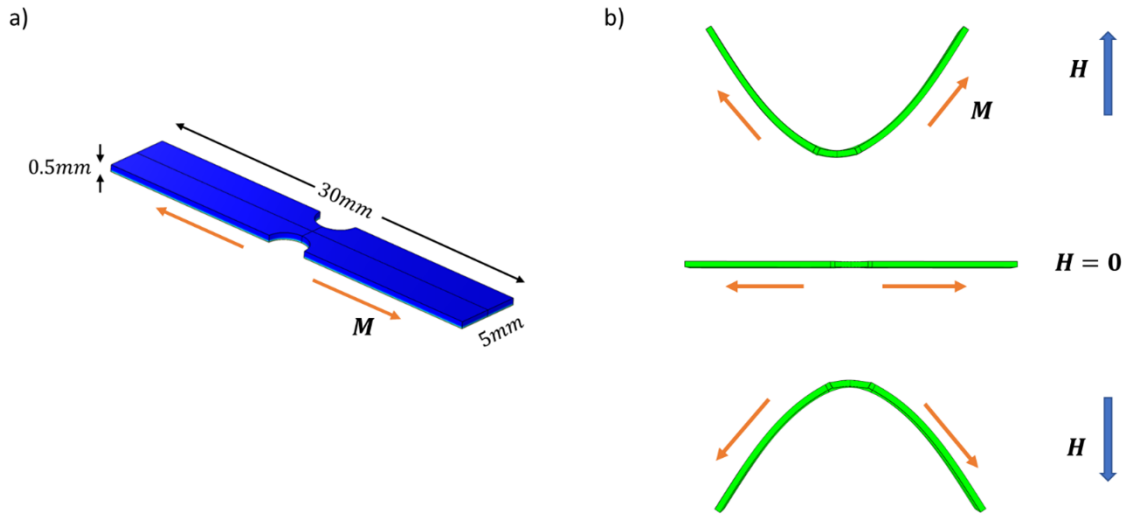
Figure 5.1: Hydrogel robot's shape analysis. (a) The geometry of the hydrogel robot. The arrows show the direction of magnetization, **M**. (b) Finite element calculations demonstrating the deformation of the hyperelastic solid in the presence of three different configurations of the external magnetic field **H**.

swimmer cycles between the three configurations generating a "flapping" motion.

5.3.2 Fluid-Structure Interaction

The flapping wings of the hydrogel swimmer can potentially generate locomotion when submerge in water due to hydrodynamic interaction. The governing equations for the fluid flow around the hydrogel robot are given by the incompressible Navier Stokes equations:

$$\rho \left(\frac{\partial \boldsymbol{u}}{\partial t} + \boldsymbol{u} \cdot \boldsymbol{\nabla} \boldsymbol{u} \right) = -\boldsymbol{\nabla} p + \boldsymbol{\nabla} \cdot \left(\mu \left(\boldsymbol{\nabla} \boldsymbol{u} + (\boldsymbol{\nabla} \boldsymbol{u})^T \right) \right) + \rho \boldsymbol{g} \tag{5.2}$$

$$\boldsymbol{\nabla} \cdot \boldsymbol{u} = 0 \tag{5.3}$$

Where ρ is the mass density of the fluid, $\boldsymbol{u}$ is the fluid velocity, μ is the dynamic viscosity of the fluid and $\rho\boldsymbol{g}$ is the volumetric force density due to gravity. The equations for the fluid motion are formulated using the Eularian description where the quantities are defined with respect to a fixed frame of reference also known as the spatial frame. This is different from the Lagrangian formalism used to describe the hyperelastic solid where the energy densities are defined with respect to the material frame that moves along with the deforming material. For the fluid motion, a Lagrangian approach would be impractical as it can lead to severe mesh distortions, therefore the Eularian formulation is more suitable. However, the Eularian description has a limitation; it is not well suited for problems where the boundaries of the fluid domain move with time as in our case where the fluid boundaries move with the flapping swimmer. In order to model the interaction between the hydrogel and the fluid, we need to combine the two formulations for which we use the Arbitrary Lagrangian–Eulerian (ALE) method. ALE takes an intermediate approach where we describe the dynamics of the system with respect to a *moving mesh* frame that is neither Lagrangian nor Eularian and can move independently. This allows us to handle the moving boundaries and interfaces without following individual fluid packets as in the Lagrangian formulation [132]. Therefore, the Navier-Stokes equations that describe the fluid motion are solved on a freely moving mesh where COMSOL calculates the mesh coordinates based on the movement of the solid structure (hydrogel swimmer). Fig. 5.2 shows an example case of an oscillating beam in water solved using COMSOL where the fluid mesh can be seen deforming in response to the solid structure's movement. The deformation of the mesh is calculated using hyperelastic smoothing [133].

The Fluid-Structure Interaction (FSI) coupling appears on the boundary between the fluid and and the solid. The total force exerted by the fluid on the solid body is

$$\mathbf{F_T} = -\mathbf{n}.\left\{ -p\mathbf{I} + \mu\left(\boldsymbol{\nabla}\boldsymbol{u} + (\boldsymbol{\nabla}\boldsymbol{u})^T \right) \right\} \tag{5.4}$$
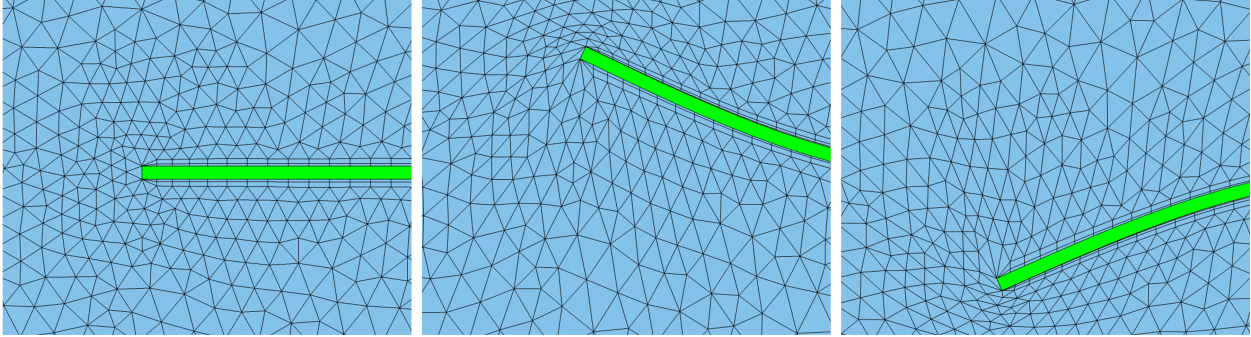
Figure 5.2: Deforming mesh in an example fluid structure interaction problem. A green colored solid beam is oscillating in the blue colored fluid. The mesh in the fluid domain deforms in response to the solid beam's movement.

where **n** is the solid surface's normal vector and **I** is the identity matrix. The coupling in the other direction is applied through a boundary condition on the fluid domain i.e. at the fluid-structure boundary, the fluid velocity is given by

$$\mathbf{u}_{fluid} = \frac{\partial \mathbf{x}_{solid}}{\partial t} \tag{5.5}$$

where $\partial \mathbf{x}_{solid}/\partial t$ is the velocity of the solid structure that acts as the velocity of the moving wall for the fluid domain.

5.4   Swimming in water

The Reynold's number (Re) for our hydrogel swimmer is ~ 100 where $Re = \rho u L / \mu$ and L is the characteristic length scale. At intermediate Reynolds numbers ($1 < Re < 1000$), both viscous and inertial forces contribute to thrust and drag. A large variety of aquatic animals also operate in this domain [134]. Our hydrogel swimmer employs a drag-based propulsion mechanism where the flapping wings of the swimmer pushes against the water to generate thrust. The propulsion mechanism is divided into two phases, the power stroke and the recovery stroke. As the swimmer
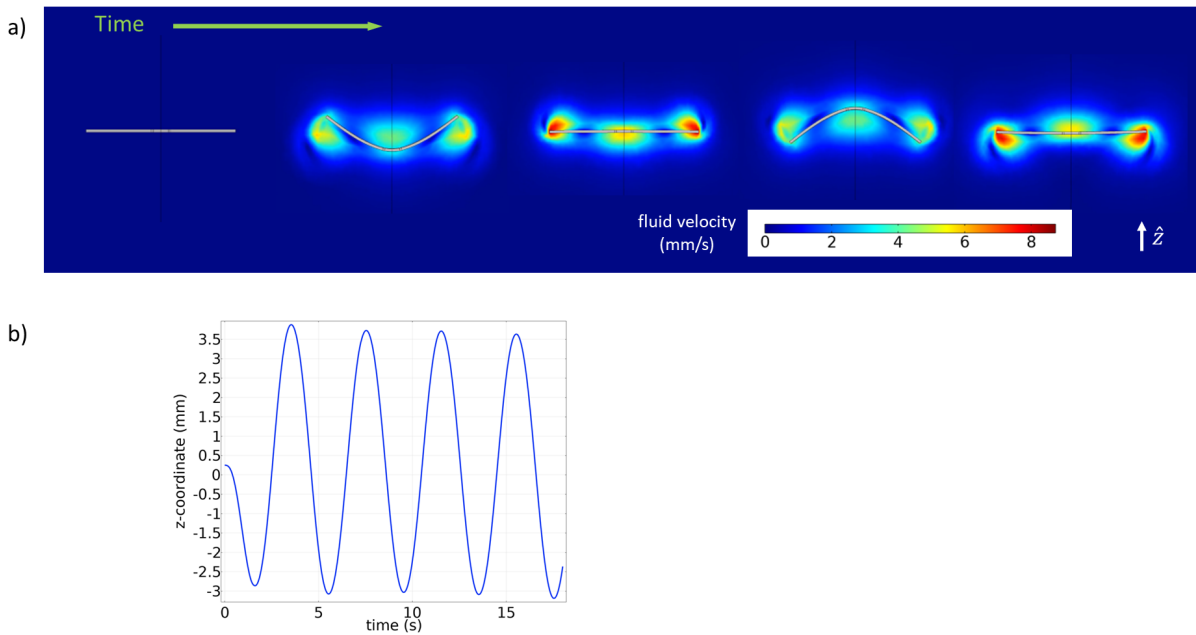
Figure 5.3: Hydrogel robot's interaction with fluid . (a) Side view of the hydrogel robot flapping its wings in an external oscillating magnetic field as a function of time. Snapshots of different configurations of the robot placed chronologically from top to bottom. The color bar represents the velocity of the surrounding fluid in mm/s (b) The z-coordinate of the center point of the robot as a function of time demonstrating no net locomotion.

closes its wings to push against the water, it generates a forward thrust due to the drag force. However, during the recovery stroke, the drag force acts in the opposite direction causing the swimmer to generate thrust in the opposite direction. Since our model swimmer is flat (fig. 5.3a leftmost) and the actuation field (magnetic field) is sinusoidal, the geometry and the motion of the swimmer is invariant under the transformation of the axis $\hat{z} \rightarrow -\hat{z}$. This symmetry of the physical problem stops the flat swimmer to undergo locomotion as the power strokes and the recovery strokes generate equal and opposite thrusts causing the swimmer to stay in the same place. This situation can be visualized in fig. 5.3a which shows snapshots of the swimming motion arranged chronologically from initial state to final state indicated by the arrow of time. Fig. 5.3a
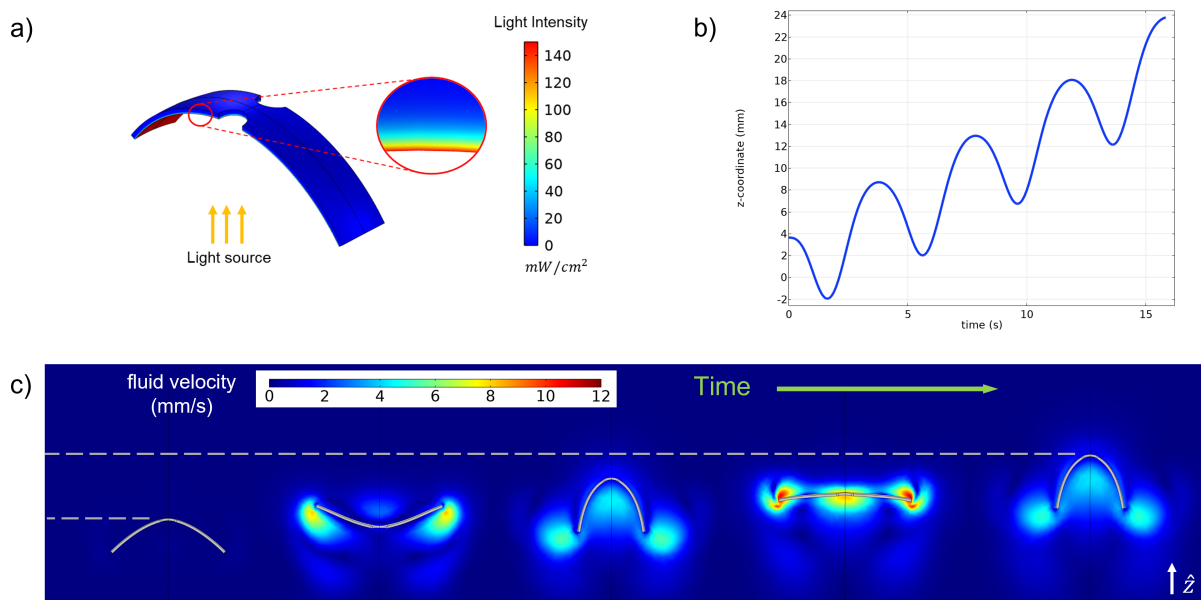
Figure 5.4: Hydrogel robot's swimming motion. (a) Deformation caused due to light with 140 mW/cm^2 intensity in the absence of magnetic field. Inset shows the gradient of light intensity responsible for the bending. (b) The z-coordinate of the center point of the robot as a function of time demonstrating a net upward motion along the z-axis. (c) Snapshots of the swimmer's upward motion arranged chronologically from left to right.

demonstrates the symmetry of the power and recovery strokes due to the initial flat shape of the swimmer. We can track the location of the swimmer by tracking the position of its geometric center along the z-axis as a function of time as shown in fig. 5.3b. It can be seen from fig. 5.3b that over time, there is no net locomotion as the swimmer keeps oscillating back and forth in the same place.

In order for the swimmer to have a net displacement underwater, we have to break the symmetry of the power and recovery strokes. This asymmetry can be introduced by deforming the geometry of the swimmer which can be done using light. As demonstrated in chapter 2, the light intensity creates a gradient of hydrophobicity in the material causing the hydrogel to bend as the side that faces the light source shrinks more compared to the side that faces away. Our hyperelastic material model (eq. 5.1) is solved along with the equations for chemical reaction and light propagation (see

Figure 5.5: Hydrogel swimmer demonstrating underwater locomotion in the lab. The three snapshots are taken in chronological order from left to right.

section 2.3.1 eq. 2.5). Fig. 5.4a shows the deformation caused due to the light in the absence of an external magnetic field. Here the light is propagating in the +z-direction and the swimmer can be seen to bend due to the presence of a gradient of light intensity inside the hydrogel. A bent geometry (fig. 5.4a) can now generate a net thrust in the z-direction as the power strokes generate more thrust compared to the recovery strokes. Fig. 5.4b is a plot of the displacement versus time of the hydrogel swimming in water in the presence of an external oscillating magnetic field. For fig. 5.4b, we have taken into account the light induced deformation. Compared to fig. 5.3b, fig. 5.4b demonstrates a net upward motion along the z-axis because of the bent shape of the swimmer. Fig. 5.4c shows the snapshots of the corresponding time sequence of the hydrogel swimming upwards (+z direction) in the fluid.

Fig. 5.5 shows the corresponding swimming motion achieved by a hydrogel swimmer synthesized in the lab. Notice the presence of a small air bubble on top of the swimmer in fig. 5.5. The air bubble is an important component as it reduces the effective 'weight' of the swimmer by providing a small buoyant force and also helps keep the swimmer upright. The bubble used in the experiments is typically of the order of $\sim 0.5\mu L$, thereby providing a net upward force of $\sim 5\mu N$. The finite element calculation depicted in fig. 5.4c takes this force into account by means of a point force applied to the center of the swimmer geometry.

5.5 Phototactic Motion

In order to understand the origin of phototactic behaviour, we have to look at the chemical composition of the dual-responsive hydrogel material. The hydrogel material developed for this project has an additional component compared to the hydrogel material presented in chapter 4. In order to improve the photo-response time of the hydrogel, we added peptide amphiphile (PA) nanofibers to the spiropyran-NIPAM-(Ni nanowire) system. PA nanofibers speed up the process of photoactuation (see section 2.3.1) by $\sim$60 times i.e. the time it takes for the swimmer to bend to the required shape for swimming, decreases from $\sim$15 mins to $\sim$ 15 secs. The surmised mechanism for this improvement is based on the movement of protons between the spiropyran chromophores and the PA fibers. In the absence of light, the acid groups on the PA fibers spontaneously protonate the chromophores into the hydrophilic form MCH^+. This drives the conversion of uncharged SP to MCH^+ while simultaneously increasing the population of the carboxylate anions in the PA fibers and chromophores. On the other hand, in the presence of light, the proton released by MCH^+ gets readily consumed by the acrylate groups present on both PA fibers and the chromophores. This leads to a simultaneous formation of the uncharged SP and protonated acrylate anions causing the hydrogel to become more hydrophobic. The presence of hydrophobic molecules causes the hydrogel to lose water and causes dehydration of the PA fibers. It has been reported in the literature that the dehydration of PA nanofibers leads to the contraction and stiffening of the supramolecular networks [39], [135]. Therefore due to the presence of PA fibers the dual-responsive hydrogel tend to get stiffer upon light irradiation. Please note that even though this is the proposed mechanism, more investigation is needed to support the argument presented here with more experimental evidence.

Regardless of the exact mechanism, we know from rheological measurements that the spiropy-
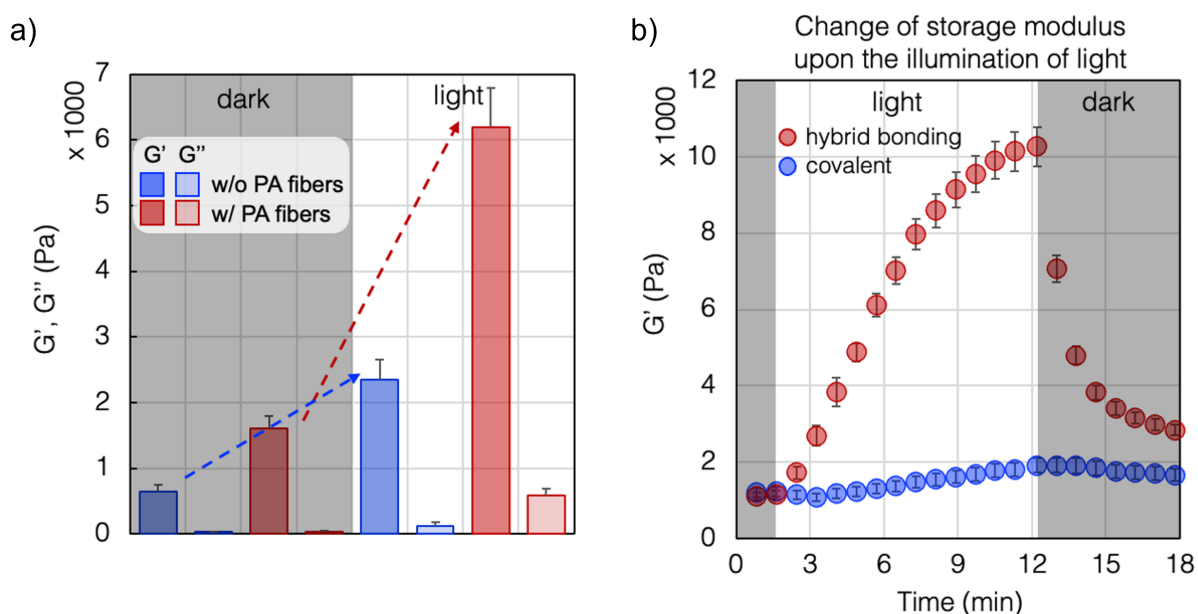
Figure 5.6: Light induced stiffening. a) Plot showing the increase in the storage and loss moduli of the spiropyran-NIPAM hydrogel in the presence of light. The increase in stiffness is much higher in hydrogels with embedded peptide amphiphile (PA) fibers compared to hydrogels without PA fibers. b) Plot showing the change in storage modulus G' in a PA fiber gel exposed to light as a function of time.

ran hydrogels with PA fibers tend to become a lot stiffer compared to the gels without PA fibers in the presence of light. This is demonstrated by fig. 5.6a which plots the storage modulus G' and the loss modulus G'' of the hydrogels with and without PA fibers. We can see that the storage modulus G' (also known as the elastic modulus) increases by a much larger extent in the presence of light for PA fiber gels. Fig. 5.6b plots G' as a function of time demonstrating the time required for the hydrogels to become stiffer.

The stiffening of the hydrogel in the presence of light leads to an interesting emergent phenomenon. This causes the hydrogel swimmer to exhibit phototaxis. An intuitive explanation of how the light induced stiffening causes phototaxis is as follows. A light source at the bottom of the fluid chamber increases the stiffness of both the wings of the hydrogel swimmer equally. However,
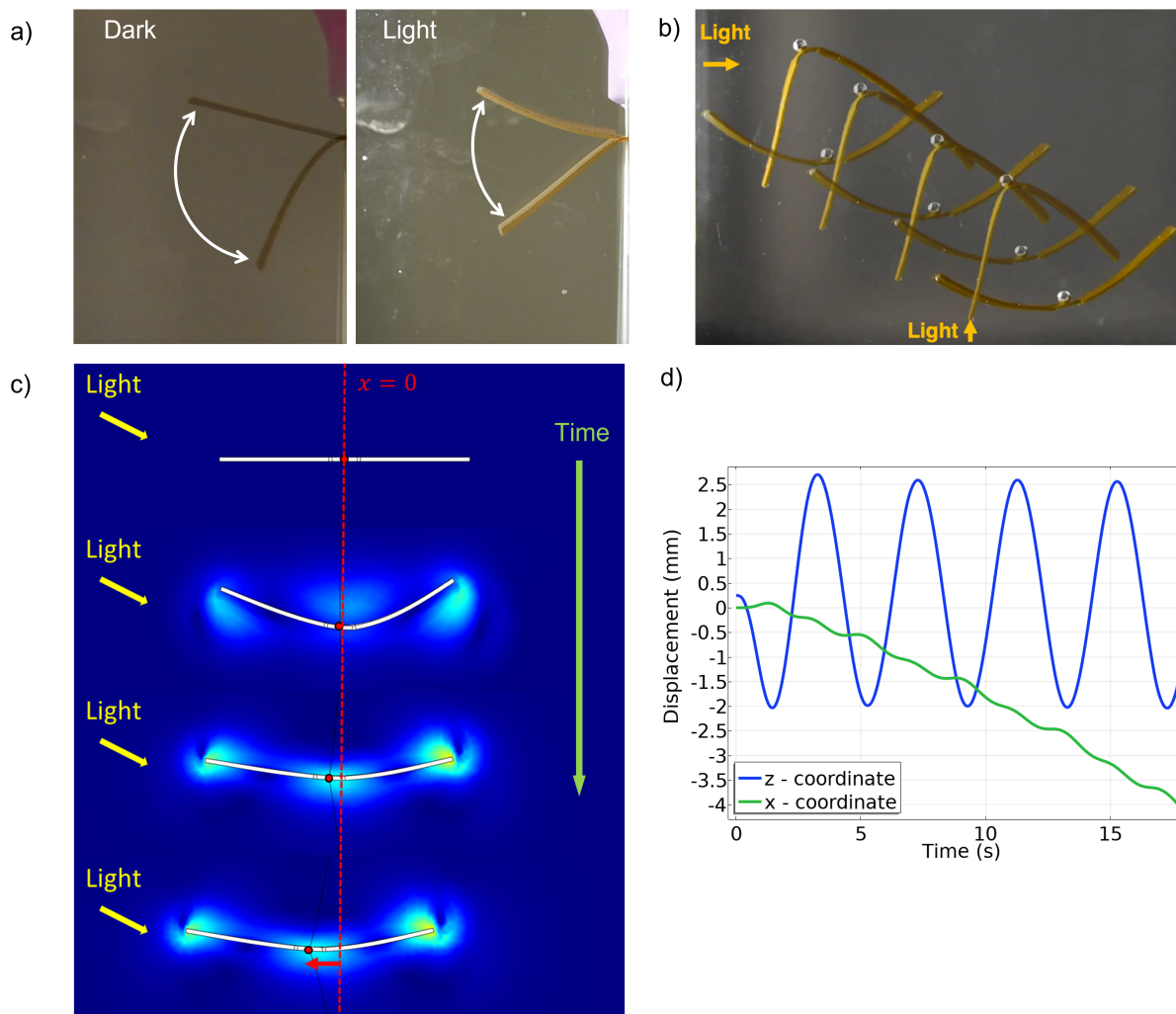
Figure 5.7: Swimming towards the light. a) Photographs of a hydrogel beam in dark and light conditions demonstrating a decrease in the range of motion due to light induced stiffness. b) Photographs of a hydrogel swimmer, swimming towards the secondary light source demonstrating the phototactic properties of the swimmer. The photographs of the swimmer at different time stamps are overlapped to show the motion. c) Finite element simulations of a 'flat' hydrogel with anisotropy in the stiffness of the wings. We can see that the swimmer gradually moves towards the direction of the stiffer wing. d) A plot of the corresponding displacement of the swimmer along the x-axis and the z-axis.

in the presence of a second light source, the wing of the swimmer that receives more light becomes stiffer. This leads to a phenomenon where the stiffer wing generates lesser thrust compared to the other wing and the swimmer starts swimming in the direction of the second light source. This phenomenon can be demonstrated by fig. 5.7a which shows an experimental setup of a hydrogel beam oscillating in an external magnetic field. We can see that the range of motion of the beam is much smaller in the presence of light as the beam becomes stiffer which leads to the generation of a smaller thrust.

Fig. 5.7b shows an experimental setup where the hydrogel swimmer is in the presence of two light sources. The primary light source shines light from below the swimmer (light travelling in +z direction) and is required for the swimmers to move along the z-axis (see section 5.4). The secondary light source shines light from the side and is responsible for creating an anisotropy in the stiffness of the two wings of the swimmer. The spontaneous steering of the hydrogel swimmer towards this secondary light source can be seen in fig. 5.7b.

This phototactic behaviour can also be seen in the theoretical calculations. Fig. 5.7c shows finite element calculation of a 'flat' swimmer with the left wing stiffer than the right wing. For the purpose of this simulation, we did not take into account the light induced geometric deformation. This was done to isolate only the effect of stiffness anisotropy. We can see from fig. 5.7c that the hydrogel does infact move towards the secondary light source. Fig. 5.7d plots the corresponding displacement of the swimmer along the x-axis and the z-axis (no net displacement along z-axis is due to the 'flat' shape of the swimmer). In the finite element simulations (fig. 5.7c), we used the storage modulus values from fig. 5.6 i.e. we chose the left wing to be $G' \sim 6 Pa$ and the right wing to be $G' \sim 1.5 Pa$. The storage modulus is given by the elastic term in the constitutive relation eq. 5.1 with $G' = k_B T / v_m N_x$.

Due to the reversibility of the spiropyran's photochemical reaction the changes in the material

stiffness due to light are also reversible. This allows us to steer the swimmer in any direction by merely moving the secondary light source and the swimmer will follow the light.

5.6 Conclusion

In this work, we developed a constitutive model for the description of a dual responsive hydrogel material that responds to both light and magnetic fields. The photo-activity of the hydrogel system is attributed to the presence of grafted spiropyran chromophores and the magneto-activity is attributed to the presence of embedded nickle nanowires in the hydrogel. In order to improve the response time of the hydrogel, peptide amphiphile (PA) fibers were added to it. Using this material, we fabricated hydrogel swimmers that are capable of underwater locomotion. Using finite element method to solve the material model, we were able to predict the dynamic response of the material to external fields. We also modeled the material's interaction with the surrounding fluid to theoretically demonstrate the swimming motion of the hydrogel robot.

Due to the interaction of PA fibers with the spiropyran in the hydrogel, the material becomes much stiffer in the presence of light. We demonstrated both theoretically and experimentally that due to this property of the PA fiber gels, the swimming robots exhibit phototactic properties which is reminiscent of biological matter. Since, the photochemical reaction is reversible, the stiffening effect of the PA fiber gels is also reversible. Therefore, the hydrogel swimmers with PA fibers have an intrinsic 'intelligence' that allows them to detect and follow an external light source.

CHAPTER 6

ACTIVITY-INDUCED MIGRATION OF VISCOUS DROPLETS ON A SOLID SUBSTRATE

6.1 Abstract

In this article we demonstrate computationally that viscous liquid droplets containing magnetic nanoparticles with frozen-in magnetic moments, sitting on a solid substrate and surrounded by an ambient gas phase can migrate under the influence of a magnetic torque. The effect arises because the collective rotation of the magnetic nanoparticles at the liquid-gas interface tilts the droplet away from a symmetric configuration, breaks the reflection symmetry with respect to the center axis, and leads to a left-right asymmetry of the contact angles. A sufficiently strong magnetic torque leads the contact angles to overcome hysteresis effects leading the droplet to migrate. Such droplets can be employed as agents in active surfaces and can move against gravity, chemical and thermal gradients, providing a mechanism that could be utilized by both industry and medicine.

6.2 Introduction

In recent years, it has become possible to design and synthesize systems that execute cooperative functions employing active matter cf. Driscoll and Delmotte [136] and references therein. Active materials are controlled by the application of external inputs such as chemical energy, magnetic

---

This chapter originates from the unpublished collaborative efforts with Dr. Eleftherios Kirkinis
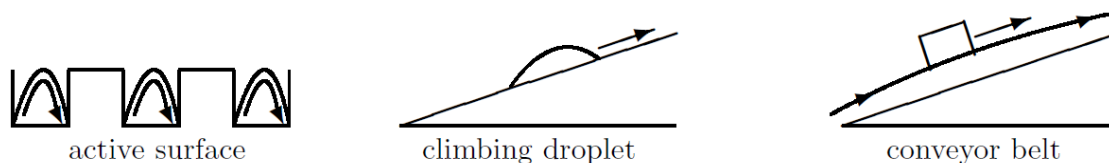
Figure 6.1: Possible applications of the present formalism. Active surfaces (left): active droplets embedded in the grooves of a solid surface reduce hysteresis and increase mobility. Arrows indicate streamlines and flow direction. Active droplets (middle): they can squeeze-through narrow spaces, work against gravitational potentials, temperature or chemical gradients and overcome barriers (see section 6.7). Here they work against gravity climbing an inclined barrier. Active films (right): they can be employed to transport cargo in a "conveyor-belt" manner

fields and/or light. Because magnetic fields can penetrate matter, they can replace chemical energy in actuating systems by enabling, for instance, the locomotion of robots [137][6].

Droplets of a magnetic liquid that can be actuated by external fields form a special case of active matter, which is employed in various fields of medicine and industry [138]. In particular, such droplets can be employed to form "active surfaces" (cf. Fig. 6.1 left) whereby they are placed in grooves of a surface and with the application of an external field they can reduce hysteresis effects and increase mobility [139]. Such droplets can navigate uncharted terrains, climb an inclined plane working against pressure, thermal or chemical gradients and gravity (cf. Fig. 6.1 center); move on the underside of a plate; climb and get past obstacles and even deform to enter narrow passage-ways [138]. Films composed of such a liquid can act as "conveyor belts" for the transport of cargo (cf. Fig. 6.1 right).

In this article, employing continuum field theories incorporating antisymmetric and couple stresses we develop models capturing the motion of magnetic droplets in diverse terrains. Droplet motion as a whole - termed migration in this article - depends on processes taking place at the

contact line. Thus, a brief discussion of known facts regarding the mobility of a contact line is at place here. It is a known experimental result [140] that a contact line moves with a horizontal velocity u_{CL} according to

$$u_{\text{CL}} = k\left[\theta(t) - \bar{\theta}_A\right]^m, \quad \text{when} \quad \theta(t) > \bar{\theta}_A, \tag{6.1}$$

where $\bar{\theta}_A \geq 0$ is the static advancing contact angle that $\theta(t)$ (the dynamic contact angle) has to overcome for the contact line motion to commence. The exponent m has been found in the experiments of [141]–[143] to acquire the value $m = 3$. The phenomenological constant k also has to be determined by experiment. For instance, Ehrhard [144] determined that $k \sim 4$ mm/sec for silicon oil and $k \sim 8$ mm/sec for parafin oil in experiments of non-isothermal spreading on glass surfaces. For the receding contact angle of Fig. 6.2 (upper right), one has

$$u_{\text{CL}} = -k\left[\theta(t) - \bar{\theta}_R\right]^m, \quad \text{when} \quad \theta(t) < \bar{\theta}_R, \tag{6.2}$$

where $\bar{\theta}_R \geq 0$ is the static receding contact angle that $\theta(t)$ (the dynamic contact angle) has to fall against for the contact line motion to commence. As discussed by Ehrhard and Davis [145] there are a number of approaches to model the contact line dynamics. The first, termed the excision approach, uses lubrication theory to describe the bulk liquid flow away from the contact line. The excised contact-line region is then replaced by *a-priori* statements about the drop shape and the "outer" region [143], [146]. A second approach is to replace the contact line by a precursor film [147]. And a third is to consider the whole drop, introduce the constitutive law eq. 6.1 and eq. 6.2 at the contact line, and employ lubrication theory for flat drops [148].

This latter approach was successfully employed by Ehrhard and Davis [145] to develop a theory of thermocapillary spreading, validated by subsequent experiments [144] and by Smith [149]

to study the *migration* of liquid droplets under a horizontal temperature gradient. In the spreading case of Ehrhard and Davis [145], a vertical temperature gradient gives rise to surface tension variations which are symmetric with respect to the center axis of the droplet and leads to the formation of two symmetric flow cells inside the droplet cf. [145, Fig.5], even when spreading has ceased. In this spreading regime, the contact lines always remain equal and the droplet shape stays symmetric with respect to its center axis. On the other hand, a horizontal temperature gradient gives rise to asymmetric surface tension with respect to the center axis of the droplet. The corresponding surface tension gradient tilts the droplet and gives rise, in principle, to a single cell [149, Fig. 6] and drives these non-isothermal droplets to migrate. During migration, the contact angles are unequal and the shape of the droplet asymmetric with respect to its center axis. It is interesting to note that the effect of the horizontal temperature gradient (subject to certain approximations employed by [149]) on the liquid-gas interface is identical to the one that would be generated by a constant surface shear "wind" imposed on a droplet or film [150].

Migration is realized when both dynamic contact angles overcome their advancing and receding static counterparts: when the right dynamic contact angle $\theta_a(t)$ exceeds the static advancing contact angle $\bar{\theta}_A$ and the left dynamic contact angle $\theta_r(t)$ falls short of the static receding contact angle $\bar{\theta}_R$ (cf. Fig. 6.2). For the problem under consideration notation becomes increasingly cumbersome. With a view to simplify it, we adopt the notation employed by Smith [149] and Ehrhard and Davis [145]. We are mainly interested in the steady state regime, that is, when the droplet has acquired a constant migration velocity, specific shape and a constant radius. Initial and transient behaviour is of some interest and these have been discussed in detail by Smith [149] for the thermocapillary problem under a horizontal temperature gradient.

Fine ferromagnetic particles suspended in a Newtonian liquid can bring about an imbalance of angular momentum [151]–[153]. This imbalance is due to deviations of the macroscopic particle
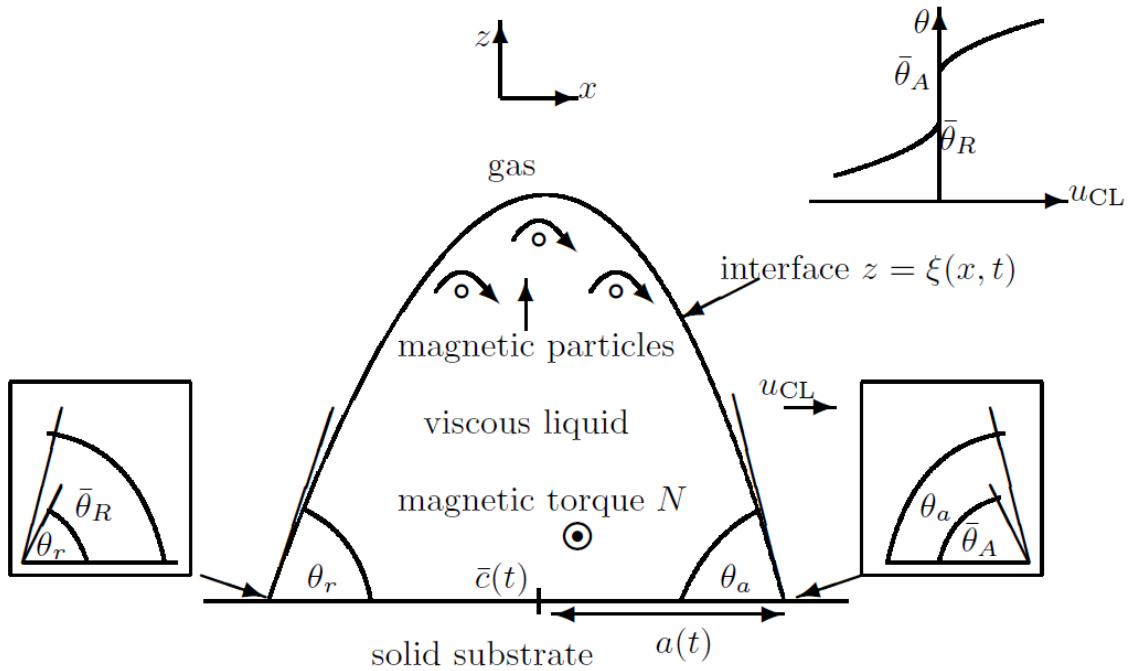
Figure 6.2: **Top right**: Experiment-inspired hysteretic diagram of a single contact line moving with velocity u_{CL} vs. dynamic contact angle θ (cf. Eq.6.1 and [140]). Thus, motion of the contact line takes place when the contact angle lies outside the interval $[\bar{\theta}_R, \bar{\theta}_A]$, determined by the *static* advancing and receding contact angles $\bar{\theta}_A$ and $\bar{\theta}_R$, respectively. **Main figure**: viscous droplet with rotational degrees of freedom (suspended ferromagnetic nanoparticles) sitting on a solid substrate and surrounded by an ambient gas phase. A moving interface at $z = \xi(x, t)$ separates a gas from a viscous liquid lying on a solid substrate located at $z = 0$. Nanosize particles suspended in the carrier liquid rotate with a macroscopic angular velocity field $\boldsymbol{\omega} = \omega(x, z, t)\hat{\boldsymbol{y}}$ by responding to a magnetic torque density $N\hat{\boldsymbol{y}} = \boldsymbol{m} \times \boldsymbol{h}$ produced by a rotating magnetic field of frequency ν applied on the suspension of macroscopic magnetization $\boldsymbol{m}$. The particle collective rotation near the liquid-gas interface induces a dominant horizontal liquid velocity component $u(x, z, t)\hat{\boldsymbol{x}}$ deforming the droplet, tilting it to the right. If the torque is strong enough so that the droplet overcomes hysteresis effects (and thus the left dynamic contact angle $\theta_r(t)$ falls short of the receding static angle $\bar{\theta}_R$ and the right dynamic contact angle $\theta_a(t)$ exceeds the advancing static contact angle $\bar{\theta}_A$ - see the corresponding insets) it starts moving to the right with velocity u_{CL}.

angular velocity from the liquid angular velocity, that is, one-half of the liquid's vorticity field, generated by an external magnetic field.

A magnetic torque can drive the suspended particles in such a way that at the liquid-gas interface, their collective rotation (in a "conveyor-belt fashion", see. Fig. 6.2), described by the macroscopic particle angular velocity ω [153] manifests itself as an effective, non-uniform surface shear stress. The effect of such a stress is to provide a dominant horizontal component for the fluid velocity u, which causes a droplet to deform.

In this article we demonstrate that viscous liquid droplets containing magnetic nanoparticles with frozen-in magnetic moments, sitting on a solid substrate and surrounded by an ambient gas phase can migrate under the influence of a magnetic torque generated by a rotating magnetic field (cf. Fig. 6.2). The effect arises because the collective rotation of the magnetic nanoparticles at the liquid-gas interface tilts the droplet away from a symmetric configuration, breaks the reflection symmetry with respect to the center axis, and leads to a left-right asymmetry of the contact angles (cf. left and right panels of Fig. 6.2). A sufficiently strong magnetic torque leads the contact angles to overcome hysteresis effects and induces droplet migration. Thus, this is a symmetry-breaking effect at the level of the Navier-Stokes equations. Symmetry-breaking is also inherited by the liquid-gas profile evolution equation as well as the mobility constitutive law eq. 6.1 describing the motion of a contact line. The effect is a companion to the thermocapillary migration of the non-isothermal liquid droplets analyzed theoretically by [149]. Thus, the theoretical and computational framework developed in the present article, with respect to symmetry-breaking and droplet mobility, encompasses these former results as a special case.

Quantity	Description	Definition
$\bar{\theta}_A, \bar{\theta}_R$	static advancing and receding contact angles	Fig. 6.2, Eq. 6.36
$\theta_a(t), \theta_r(t)$	right and left dynamic contact angles	Fig. 6.2, Eq. 6.34
η, ζ, η'	constitutive parameters	Eq. 6.4, Eq. 6.6
$c_a(t), c_r(t)$	horizontal coordinates of right/left contact lines	Eq. 6.34
u, w	dimensional horizontal/vertical velocity fields	Eq. 6.19
u_{CL}	dimensional contact line velocity	Eq. 6.1
ω	dimensional particle angular velocity	Eq. 6.25
m, h, b	dimensional magnetization & magnetic fields	Eq. 6.7
ℓ, λ	dimensional slip lengths	Eq. 6.16
k	contact line mobility	Eq. 6.1
$\mathcal{K}$	mean curvature	Eq.6.11, 6.30
$\hat{\mathbf{t}}, \hat{\mathbf{n}}$	tangent and normal unit vectors at an interface	Fig.6.2, Eq.6.11, 6.28
x, z, t	dimensional spatial coordinates and time	Fig. 6.2
$\xi(x, t)$	dimensional liquid-gas interface	Eq. 6.18
τ_{B}, ν	Brownian time scale and external field frequency	Eq.6.9
p	dimensional pressure	Eq. 6.4
N	dimensional magnetic torque	Eq. 6.8
g	dimensional grav. acceleration	Eq.6.26
ϕ	dimensional potential	Eq.6.26
ψ	inclination angle of a plane	Section 6.7

Table 6.1: Notation employed in this chapter

6.3   Viscous liquid motion in the presence of rotational degrees of freedom

In a liquid with rotational degrees of freedom - a classical Newtonian liquid with small suspended particles that can respond to an external torque - the balance of linear and internal angular momentum can be expressed in the form [151], [152]

$$\rho Du_i/Dt = \partial_k \sigma_{ik} \quad \text{and} \quad ID\omega_i/Dt = \partial_k C_{ik} + N_i + \epsilon_{imk}\sigma_{km}, \quad i,k,m = 1,2,3, \tag{6.3}$$

where D/Dt is the convective derivative, ρ is the fluid density, I the volume density of particle moment of inertia u_i is the fluid velocity, ω_i the particle angular velocity and N_i is the magnetic torque density. As noted by Dahler and Scriven [151] the last term of the second equation in 6.3 represents the transformation of moment of momentum $\epsilon_{ijk}x_i u_j$ into internal angular momentum only when the stress σ_{ij} has an antisymmetric part. This part augments the standard Cauchy stress tensor and arises solely due to the inclusion of the nanostructure in the liquid. The resulting total stress $\boldsymbol{\sigma}$ is [153]

$$\sigma_{ik} = -p\delta_{ik} + \eta \hat{V}_{ik} + \zeta \hat{W}_{ik} + \hat{T}_{ik}, \tag{6.4}$$

where $\hat{V}_{ik} = \partial_k u_i + \partial_i u_k$ is twice the rate-of-strain tensor, $\hat{W}_{ik} = \partial_k u_i - \partial_i u_k - 2\epsilon_{kil}\omega_l$ is a "spin" tensor measuring the imbalance between liquid and particle angular velocity, $\hat{T}_{ik} = (h_i b_k - \frac{1}{2}h_j^2 \delta_{ik})/4\pi$ is the Maxwell stress tensor and $\boldsymbol{h}$ and $\boldsymbol{b}$ denote the *macroscopic* magnetic field and induction respectively. The liquid is considered incompressible

$$\partial_i u_i = 0, \tag{6.5}$$

p is the hydrostatic pressure and η is the liquid viscosity. The phenomenological coefficient ζ multiplying $\hat{W}$ in eq. 6.4 is termed the vortex viscosity in the literature [152], [153]. ϵ_{ijk} is the alternating pseudotensor and we employed the Einstein summation convention on repeated indices. $\hat{W}$ has curl$\boldsymbol{u} - 2\boldsymbol{\omega}$ as its axial vector. When this vector vanishes identically in the body of a slowly flowing viscous liquid in the absence of externally applied torques and non-conservative forces, the balance of internal angular momentum in eq. 6.3 is automatically satisfied and the balance of linear momentum in eq. 6.3 reduces to the standard Navier-Stokes equations satisfied by the velocity field of an unstructured liquid [152]. Diffusion of internal angular momentum takes place due to couple stresses $\boldsymbol{C}$

$$C_{ik} = \eta' \left(\partial_k \omega_i + \partial_i \omega_k \right) + \zeta' \partial_j \omega_j \delta_{ik}, \tag{6.6}$$

the suspended particles experience in their rotational motion. Here η' and ζ' are the shear and bulk coefficients of spin viscosity [152]. Therefore, $\partial_j C_{ij}$ in Eq. 6.3 is the rate of arrival of internal angular momentum by way of diffusion. Maxwell's equations are

$$\nabla \times \boldsymbol{h} = \boldsymbol{0}, \quad \text{and} \quad \nabla \cdot \boldsymbol{b} = 0, \tag{6.7}$$

where $\boldsymbol{b} = \boldsymbol{h} + 4\pi \boldsymbol{m}$. Since the torque density

$$\boldsymbol{N} = \boldsymbol{m} \times \boldsymbol{h} \tag{6.8}$$

depends on the macroscopic magnetization field $\boldsymbol{m}$ of suspended particles, one more constitutive equation describing the evolution of this field has to be imposed in order to provide closure

[153]. This is

$$Dm_i/Dt = \epsilon_{ijk}\omega_j m_k - (m_i - \chi h_i)/\tau_B \quad i = 1, 2, 3. \tag{6.9}$$

Here τ_B is the Brownian relaxation time [153, p.54-57] and χ is the effective magnetic suscep-

tibility

$$\chi = nm_d L(\alpha)/h, \quad L = \coth\alpha - \frac{1}{\alpha}, \quad \alpha = \frac{m_d h}{k_B T}, \tag{6.10}$$

where $m_d = M_d V$ is the magnetic moment of a single subdomain particle, V is the particle

volume, M_d is the domain magnetization of dispersed ferromagnetic material and n is the number

density of the magnetic grains. In this form, Eq. 6.9 applies only at moderate strengths of the

applied field. For a discussion of this point see Rinaldi [153, p.54-57] and references therein.

6.3.1   Boundary conditions

At a liquid-gas interface with mean curvature $\mathcal{K}$ and constant surface tension γ, continuity of

traction implies [154],

$$-[[\boldsymbol{\sigma n}]] + 2\mathcal{K}\gamma\boldsymbol{n} = \boldsymbol{0} \tag{6.11}$$

where $\boldsymbol{n}$ and $\boldsymbol{t}$ are the normal and tangent unit vectors at this interface respectively, and the

symbol $[[\cdot]]$ denotes the jump of the field across an interface. Thus, for the shear and normal

stresses we have

$$[[\boldsymbol{t\sigma n}]] = 0, \quad \text{and} \quad [[\boldsymbol{n\sigma n}]] = 2\mathcal{K}\gamma, \tag{6.12}$$

on the liquid-gas interface, while the couple-stress tensor $\boldsymbol{C}$ satisfies [155]

$$[[\boldsymbol{Cn}]] = \boldsymbol{0}. \tag{6.13}$$

At the liquid-solid interface the no-slip and no penetration conditions read

$$\boldsymbol{u} \cdot \boldsymbol{t} = 0, \quad \boldsymbol{u} \cdot \boldsymbol{n} = 0. \tag{6.14}$$

respectively. When required, the former can be relaxed and be replaced by a slip model as is usual in thin liquid film and droplet studies [154], [156], [157]. Finally the question arises as to the most suitable boundary condition satisfied by the particle angular velocity at the liquid-solid interface. In the literature of magnetic liquids one may specify a condition of the form [158]–[160],

$$\boldsymbol{\omega} = \boldsymbol{0}. \tag{6.15}$$

It may however be necessary to allow for a finite angular velocity at this boundary. Aero, Bulygin, and Kuvshinskii [161] allowed for rotation of the ferroparticles derived by the balance of their overall angular velocity at the liquid-solid interface with the surface density of micromoments

$$\boldsymbol{\omega} = \hat{\boldsymbol{\lambda}}\hat{\mathbf{C}}\hat{\mathbf{n}} \tag{6.16}$$

cf. [161, Eq.(6.6)] where λ_{ij}, having units of length, is the inverse of the rotational friction tensor and $\hat{\mathbf{n}}$ is normal at the solid-liquid interface so that the appearance of micro-moments at the surface is due to friction. We note that this boundary condition is analogous to the Navier slip condition of Newtonian fluid mechanics [162] thus λ_{ij} is a rotational slip length. Its values will depend on surface roughness, liquid viscosity and particle size.

At the liquid-gas interface the induction and magnetic field components are continuous

$$[[\boldsymbol{b} \cdot \boldsymbol{n}]] = 0 \quad \text{and} \quad [[\boldsymbol{h} \cdot \boldsymbol{t}]] = 0. \tag{6.17}$$

6.4 Reduction of the equations of motion

In the geometry displayed in Fig. 6.2 and in dimensional units, the liquid-gas interface lies at

$$z = \xi(x, t) \tag{6.18}$$

and the solid-liquid interface at $z = 0$. The fluid velocity $\boldsymbol{u}$, macroscopic particle angular velocity $\boldsymbol{\omega}$ and magnetization $\boldsymbol{m}$ obtain the component forms

$$(u(x, z, t), 0, w(x, z, t)), \quad (0, \omega(x, z, t), 0) \quad \text{and} \quad (m_1(x, z, t), 0, m_3(x, z, t)), \tag{6.19}$$

respectively. The stress tensor eq. 6.4 has the following non-vanishing components

$$\sigma_{11} = -p + 2\eta u_x, \quad \text{and} \quad \sigma_{13} = (\eta + \zeta)u_z + (\eta - \zeta)w_x - 2\zeta\omega, \tag{6.20}$$

$$\sigma_{31} = (\eta - \zeta)u_z + (\eta + \zeta)w_x + 2\zeta\omega, \quad \text{and} \quad \sigma_{33} = -p + 2\eta w_z, \tag{6.21}$$

where a low case Latin subscript denotes differentiation with respect to the corresponding dimensional variable. For clarity and brevity we did not manifestly include the Maxwell stress tensor components in these expressions because they only give rise to a body force whose effects are subdominant to those of the torque studied in the present article (assuming weak fields and slow

rotations, see the discussion in [163, Appendix A]). The couple stress tensor C has the following non-zero components

$$C_{12} = C_{21} = \eta'\omega_x \quad \text{and} \quad C_{23} = C_{32} = \eta'\omega_z \tag{6.22}$$

and we assume that $\partial_j\omega_j = 0$ is also satisfied. Then, the governing equations 6.3 reduce to

$$\rho\left[u_t + uu_x + wu_z\right] = -p_x - 2\zeta\omega_z + (\zeta + \eta)(u_{xx} + u_{zz}) - \phi_x, \tag{6.23}$$

$$\rho\left[w_t + uw_x + ww_z\right] = -p_z + 2\zeta\omega_x + (\zeta + \eta)(w_{xx} + w_{zz}) - \phi_z, \tag{6.24}$$

$$I\left[\omega_t + u\omega_x + w\omega_z\right] = 2\zeta(u_z - w_x - 2\omega) + \eta'(\omega_{xx} + \omega_{zz}) + N. \tag{6.25}$$

where N is an applied magnetic torque and the potential ϕ represents fields acting on the droplet such as gravity, intermolecular forces etc. For the present analysis we will consider that ϕ represents the gravitational field acting on a droplet placed on an inclined substrate at angle ψ to the horizontal x-axis, leading to

$$\phi = \rho g(x\sin\psi + z\cos\psi). \tag{6.26}$$

The boundary conditions eq. 6.14 and eq. 6.16 become

$$u = 0, \quad w = 0 \quad \text{and} \quad \omega = \lambda\omega_z, \quad \text{at} \quad z = 0, \tag{6.27}$$

The tangent and normal vectors to the interface are

$$\boldsymbol{t} = (1, 0, \xi_x)/\sqrt{1 + \xi_x^2} \quad \text{and} \quad \boldsymbol{n} = (-\xi_x, 0, 1)/\sqrt{1 + \xi_x^2} \tag{6.28}$$

respectively. Thus, at the liquid-gas interface $z = \xi(x, t)$ the boundary conditions eq. 6.12 read

$$\sigma_{13} - \xi_x^2 \sigma_{31} + \xi_x(\sigma_{33} - \sigma_{11}) = 0 \quad \text{and} \quad \frac{\sigma_{33} + \xi_x^2 \sigma_{11} - \xi_x(\sigma_{13} + \sigma_{31})}{\sqrt{1 + \xi_x^2}} = \gamma \xi_{xx}. \tag{6.29}$$

where in eq. 6.12 we employed the expression for the curvature

$$2\mathcal{K} = \frac{\xi_{xx}}{\sqrt{1 + \xi_x^2}}. \tag{6.30}$$

Eq. 6.13 becomes

$$\omega_z - \xi_x \omega_x = 0. \tag{6.31}$$

To the above one may add the kinematic condition

$$w = \xi_t + u\xi_x \tag{6.32}$$

at the liquid-gas interface $z = \xi(x, t)$ which constitutes the starting point in deriving the sought-after evolution equation.

The problem of determining the motion of a droplet reduces to solving an evolution equation for the liquid-gas interface $z = \xi(x, t)$ with boundary conditions

$$\xi(c_a(t), t) = \xi(c_r(t), t) = 0, \quad \int_{c_r(t)}^{c_a(t)} \xi(x, t)dx = V_0, \tag{6.33}$$

where

$$c_a(t) \quad \text{and} \quad \theta_a(t), \qquad c_r(t) \quad \text{and} \quad \theta_r(t) \tag{6.34}$$

is the x-location of the contact line and dynamic contact angle at the right and the left contact line of the droplet, respectively (cf. Fig. 6.2). Following [149], we adopt the mobility law

$$\frac{dc_a}{dt} = \begin{cases} (\theta_a - \bar{\theta}_A)^m, & \theta_a > \bar{\theta}_A \\ 0, & \bar{\theta}_R \leq \theta_a \leq \bar{\theta}_A \\ -(\bar{\theta}_R - \theta_a)^m & \theta_a < \bar{\theta}_R \end{cases} \quad \text{and} \quad \frac{dc_r}{dt} = \begin{cases} -(\theta_r - \bar{\theta}_A)^m, & \theta_r > \bar{\theta}_A \\ 0, & \bar{\theta}_R \leq \theta_r \leq \bar{\theta}_A \\ (\bar{\theta}_R - \theta_r)^m & \theta_r < \bar{\theta}_R \end{cases}$$

$$(6.35)$$

where $\theta_a(t) = -\xi_x(c_a(t))$ and $\theta_r(t) = \xi_x(c_r(t))$ (cf. Fig. 6.2) and

$$\bar{\theta}_A \quad \text{and} \quad \bar{\theta}_R \tag{6.36}$$

are the advancing and receding *static* contact angle, respectively (upper right corner Fig. 6.2).

6.5 Numerical Analysis

The ferrofluid is modeled using COMSOL's *moving mesh* method. The moving mesh approach models the free surface of a fluid domain (fluid-air interface) as a geometric surface that separates the fluid domain from the air domain. The air domain is not explicitly defined and the interfacial effects are modeled via the surface tension and other surface forces applied directly on the fluid surface as boundary conditions at the *free surface*. This is one advantage of modeling the free surface using the moving mesh method as we only need to model one phase (liquid domain) and we can ignore the other phase (gas domain). This leads to a substantial improvement in performance compared to other commonly used field based methods such as the level set and the phase field methods Also, since the interface is defined as a geometric surface, the moving mesh method provides a much sharper and accurate interface compared to field based methods. However, the

moving mesh method has a shortcoming i.e. it cannot handle topological changes, eg. a droplet splitting into two. This limitation of the moving mesh method does not affect us as our fluid domain would not split into multiple domains.

6.5.1 Modeling the equation of fluid motion

We use COMSOL's in-built *laminar flow module* to model the fluid body. We augment this in-built module to include the ferromagetic interaction by appropriately adding additional equations to the model. First, we start with the Navier-Stokes equation that the laminar flow module solves i.e.

$$\rho Du_i/Dt = \partial_k \sigma_{ik} \quad \text{with} \quad \sigma_{ik} = -p\delta_{ik} + \eta(\partial_k u_i + \partial_i u_k). \tag{6.37}$$

From eq. 6.4 we can see that we need to add an additional term $\zeta \hat{W}_{ik} = \zeta(\partial_k u_i - \partial_i u_k - 2\epsilon_{kil}\omega_l)$ to the stress tensor. We use COMSOL's *weak contribution* functionality to add this term as a weak contribution to the in-built Navier-Stokes equation. The contribution term is given by

$$div(\zeta \hat{W}_{ik}) = \partial_k(\zeta \hat{W}_{ik}) \tag{6.38}$$

multiplying it with a test function ν_i and integrating with respect to the domain Ω, we get

$$\int_\Omega \partial_k(\zeta \hat{W}_{ik})\nu_i = \int_\Omega \zeta \partial_k \hat{W}_{ik}\nu_i \tag{6.39}$$

Using integration by parts and since the test functions are required to be zero at the domain boundary, we get

$$\int_{\Omega} \partial_k(\zeta \hat{W}_{ik})\nu_i = \int_{\Omega} -\zeta \hat{W}_{ik}\partial_k \nu_i \tag{6.40}$$

$$= \int_{\Omega} -\zeta \left(\hat{W}_{13}\partial_z \nu_1 + \hat{W}_{31}\partial_x \nu_3 \right) \tag{6.41}$$

where $\hat{W}_{13}$ and $\hat{W}_{31}$ are the only non zero terms since angular velocity of the ferromagnetic particles points only along the y-axis $\boldsymbol{\omega} = (0, \omega, 0)$. The in-built test function provided by COMSOL is given by $\boldsymbol{\nu} = (test(u), test(v), test(w))$ and their derivatives $\partial_k \nu_i$ are given by $test(u_x)$, $test(u_y)$, $test(u_z)$, $test(v_x)$, $test(v_y)$ and so on. Therefore, the weak expression is given by

$$\int_{\Omega} -\zeta \left(\hat{W}_{13}test(u_z) + \hat{W}_{31}test(w_x) \right)$$
$$= \int_{\Omega} -\zeta \left(u_z - w_x - 2\omega \right) \left(test(u_z) - test(w_x) \right) \tag{6.42}$$

where $\hat{W}_{13} = -\hat{W}_{31} = (u_z - w_x - 2\omega)$. This weak contribution expression will therefore model the additional terms (terms otherwise not present in the usual Navier-Stokes equation) present in the equations 6.23 and 6.24. The equations for fluid motion are solved together with the differential equation for the particle angular velocity given by the eq. 6.25 using COMSOL's *Convection-Diffusion Equation (cdeq)* module.

Note: The equations derived here are for a droplet lying in the x-z plane. However, COMSOL uses the x-y plane. The readers can easily rewrite the equations for x-y plane or re-derive them.

6.5.2 Implementation of the contact angle hysteresis

In order to implement the contact angle hysteresis, we follow the approach developed by Cai and Song [164]. The method involves dividing the motion of the droplet into two states - *pinned state* and *moving state*. If the contact angle lies in the range $\bar{\theta}_R \leq \theta \leq \bar{\theta}_A$, the droplet is considered to be in the pinned state and for $\theta < \bar{\theta}_R$ or $\theta > \bar{\theta}_A$, the droplet is considered to be in a moving state.

The contact angle θ_{in} is used as the input for COMSOL which is given by

$$\theta_{in} = \theta_0 + kd \tag{6.43}$$

where θ_0 is the initial contact angle; d is the displacement of the contact point and k is the penalty term. We set limits on θ_{in} such that θ_{in} never exceeds $\bar{\theta}_A$ and never becomes less than $\bar{\theta}_R$.

When the droplet is in the *pinned state*, any displacement d of the contact point causes θ_{in} to change in value in order to keep the contact line (almost) stationary. A higher value of k allows for a more precise pin as even a small d causes a large change in θ_{in}. In the *moving state*, θ_{in} saturates to either $\bar{\theta}_A$ or $\bar{\theta}_R$ and we update the values of θ_0 and d at every time step. A more detailed explanation and instructions for implementation can be found in [164].

Lastly, we need to define a geometry for our droplet such that in the absence of a magnetic torque the droplet should be stationary. To achieve this, we assume the geometry of the droplet to be a section of an ellipse. This geometry may not be the steady state shape of the droplet, therefore, we let the droplet equilibrate under gravity and surface tension for 2 seconds. The equilibration time is dependent on the viscosity of the fluid, therefore the readers should choose this time accordingly. We then take the equilibrated shape as the initial shape for the magnetic torque simulations.

6.6   Droplet migration on a horizontal substrate

Here we simulated a ferrofluid droplet moving on a horizontal substrate due to a constant magnetic torque density, $\mathbf{N}\hat{y}$. Fig. 6.3 shows the case of a droplet (parameters in table 6.2) with the length of the base $\sim 1.5mm$. The response of the droplet is captured in fig. 6.3.

Due to the symmetry of the initial conditions, the left and the right contact angles (θ_r and θ_a respectively) of the droplet in fig. 6.3a are equal at $t = 0ms$ with $\theta_a = \theta_r \sim 48°$. The static contact angles $\bar{\theta}_A$ and $\bar{\theta}_R$ are set to $51°$ and $45°$ respectively. Since the initial contact angles lie withing the range $[\bar{\theta}_R, \bar{\theta}_A]$, the droplet is at rest initially. Because of the magnetic torque density $\mathbf{N}\hat{y}$, the ferrofluid particles start spinning clockwise and set the fluid in motion as seen by the streamlines plotted in fig. 6.3a. The arrows on the streamlines show the clockwise direction of the fluid motion. Due to the fluid motion, the droplet tilts towards the right (fig. 6.3a $t = 5ms$). This causes the dynamic contact angles to overcome the static contact angles as shown in fig. 6.3b which plots the dynamic and static contact angles of the left and the right contact points. The droplet becomes mobile as a result of $\theta_a > \bar{\theta}_A$ and $\theta_r < \bar{\theta}_R$, thus becoming mobile (see eq. 6.35). The corresponding velocities of the left and right contact lines can be seen in fig. 6.3c.

Using our model we can furthermore calculate the functional dependence of droplet velocity on parameters such as the applied torque density N and the static contact angles ($\bar{\theta}_A$ and $\bar{\theta}_R$). Similar to the experimental power law used in contact line dynamics eq. 6.1, we can write a power law for the contact line velocity as a function of the applied torque.

$$u_{\mathrm{cl}} \sim k \left[N - N_c\right]^m \quad \text{for} \quad N \geq N_c \tag{6.44}$$

where N_c is the critical torque required for the droplet to move and the phenomenological constants k and m can be found using the finite element simulations. Using the boundary condition,
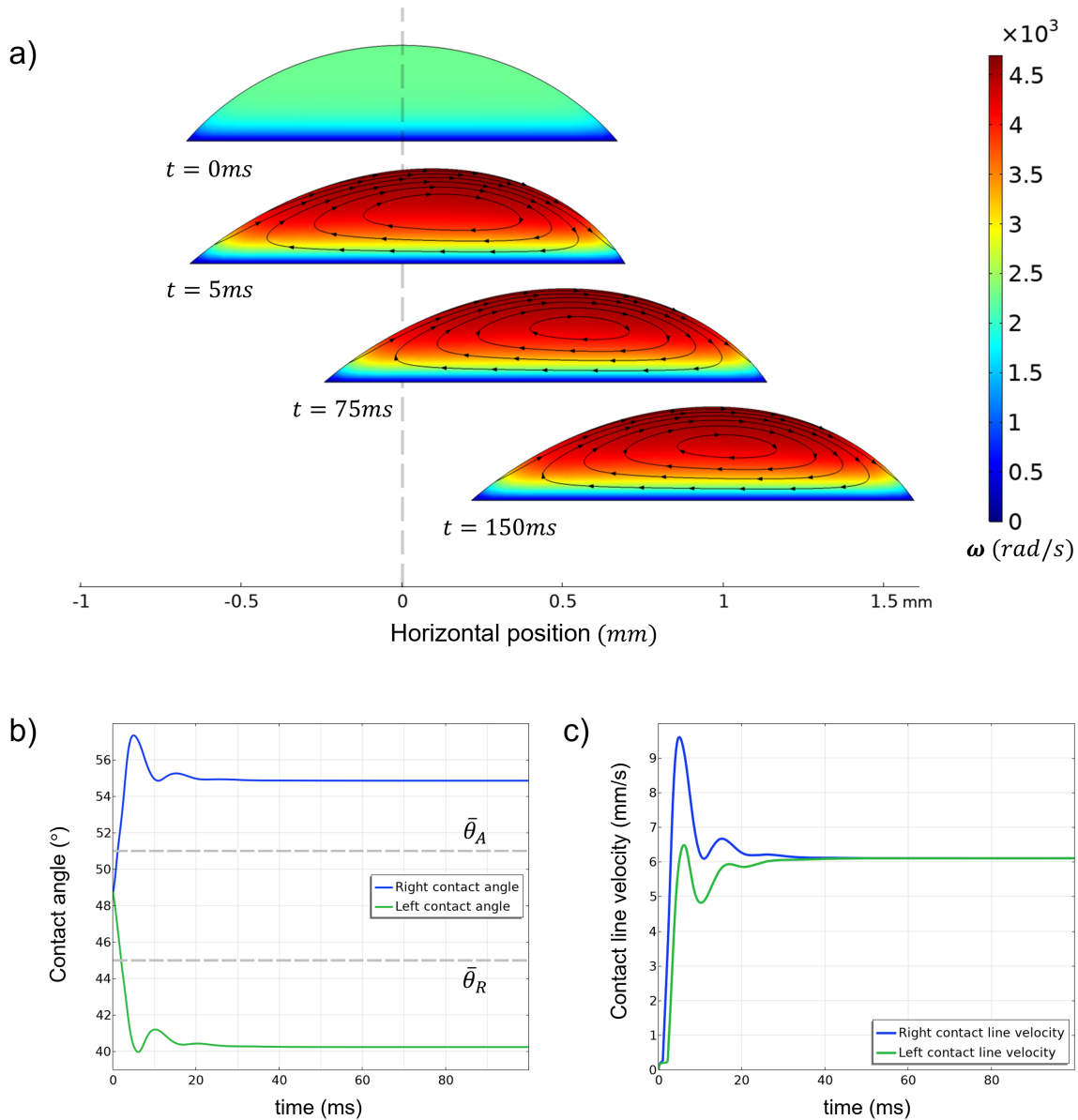
Figure 6.3: Droplet migrating on a horizontal substrate. a) Finite element plots showing snapshots of a migrating droplet at different times demonstrating the horizontal movement of the droplet. The arrows on the streamlines point in the direction of fluid motion. The color plot represents the particle angular velocity $\omega(rad/s)$. b) Plot of the time evolution of the left and the right contact angles (°) of the droplet depicted in (a). c) Corresponding plot of the velocities (mm/s) of the left and the right contact points as a function of time. The value of N used here is $10N/m^2(-\hat{y})$.
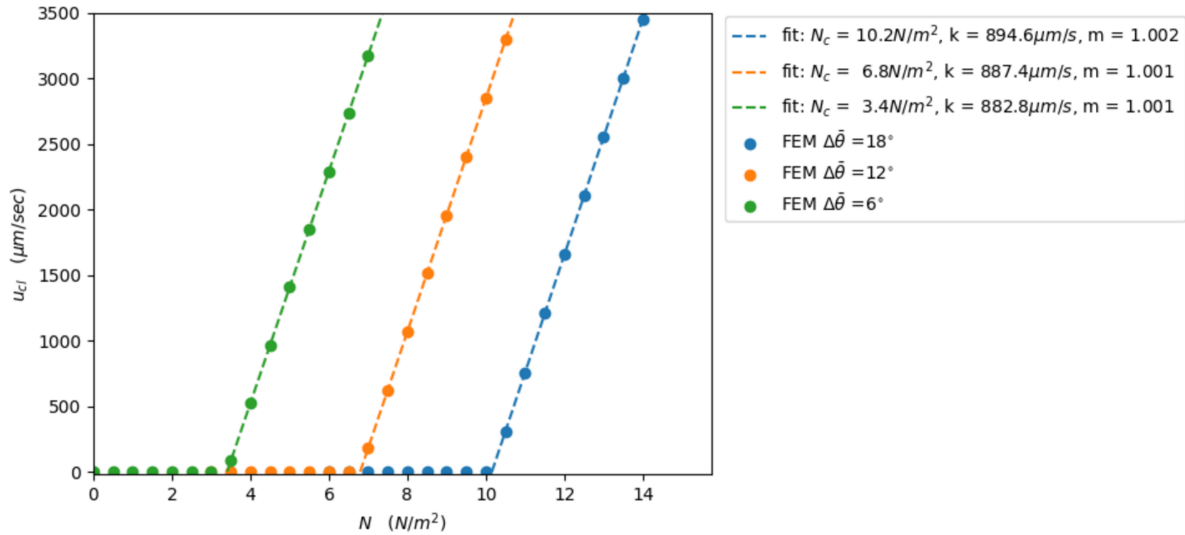
Figure 6.4: Plot of droplet velocity $u_{cl}(\mu m/sec)$ as a function of applied magnetic torque density $N(N/m^2)$. The fits represent the power law fits given by the eq. 6.44 of the non-zero velocity points.

$\omega = 0$ at $z = 0$ (see equation 6.27) we calculated the motion of a droplet as a function of increasing magnetic torque density N for three different sets of $\bar{\theta}_A$ and $\bar{\theta}_R$ i.e. $[\bar{\theta}_R, \bar{\theta}_A]$ = [45, 51], [42, 54] and [39, 57]. The plot in fig. 6.4 shows the velocity of the droplet as a function of the applied torque. The data points in the plot represent the data generated by the finite element calculations and we can see the existence of a critical N_c below which the droplet doesn't not move. This is because of the contact angle hysteresis as some torque density is 'used' to overcome the static contact angles. The dotted lines represent the non-zero data points fitted with the power law curves given by the equation $u_{cl} = k\left[N - N_c\right]^m$ where the constants k, m and N_c are used as the fitting parameters and we can see from the fits that the exponent $m \approx 1$. We also find that the critical torque $N_c \propto (\bar{\theta}_A - \bar{\theta}_R)$.

Quantity	Value	Definition
ρ (kg m^{-3})	1.5×10^3	fluid density
η (Pa s)	6×10^{-3}	viscosity eq. 6.4
ζ (Pa s)	6×10^{-4}	vortex viscosity eq. 6.4
η' (N s)	1×10^{-12}	spin viscosity eq. 6.6
γ (N/m)	29×10^{-3}	surface tension eq. 6.12
a_0 (m)	6.7×10^{-4}	characteristic droplet radius
h (m)	3×10^{-4}	droplet maximum thickness
λ (m)	0	rotational slip length eq. 6.16
k (°/m)	10^7	contact angle hysteresis penalty term eq. 6.43
$\bar{\theta}_R, \bar{\theta}_A$ (°)	$45°, 51°$	static contact angles eq. 6.36

Table 6.2: Parameter values used in finite element analysis. Some of the values are taken from [158]–[160] (EFH1 oil-based ferrofluid, Ferrotec Corp. Bedford NH, USA).

6.7 Droplet migration against fields: the inclined substrate

The mechanism described in the present article, can be employed to drive droplets against external fields and forces. For instance, we used the model to drive droplets against the gravitational field as the droplets climb a plane inclined at an angle ψ (cf. Fig.6.1, middle). Fig. 6.5a shows the case of a droplet climbing an inclined plane with an angle $\psi = 20°$ and $[\bar{\theta}_R, \bar{\theta}_A] = [45, 51]$ i.e. $\Delta\bar{\theta} = 6°$. The value of the magnetic torque density N used here is $10 N/m^2(-\hat{y})$. Due to the contact angle hysteresis we again see a critical N_c required for the droplet to move, similar to the droplet moving on a horizontal plane. However, for this case, N_c should change with the inclination angle of the substrate as the droplet now has to move against the gravity. Fig. 6.5b shows the plot of N_c as a function of changing inclination angles demonstrating an increase in its value as expected. Here we kept $\Delta\bar{\theta}$ constant at $6°$.
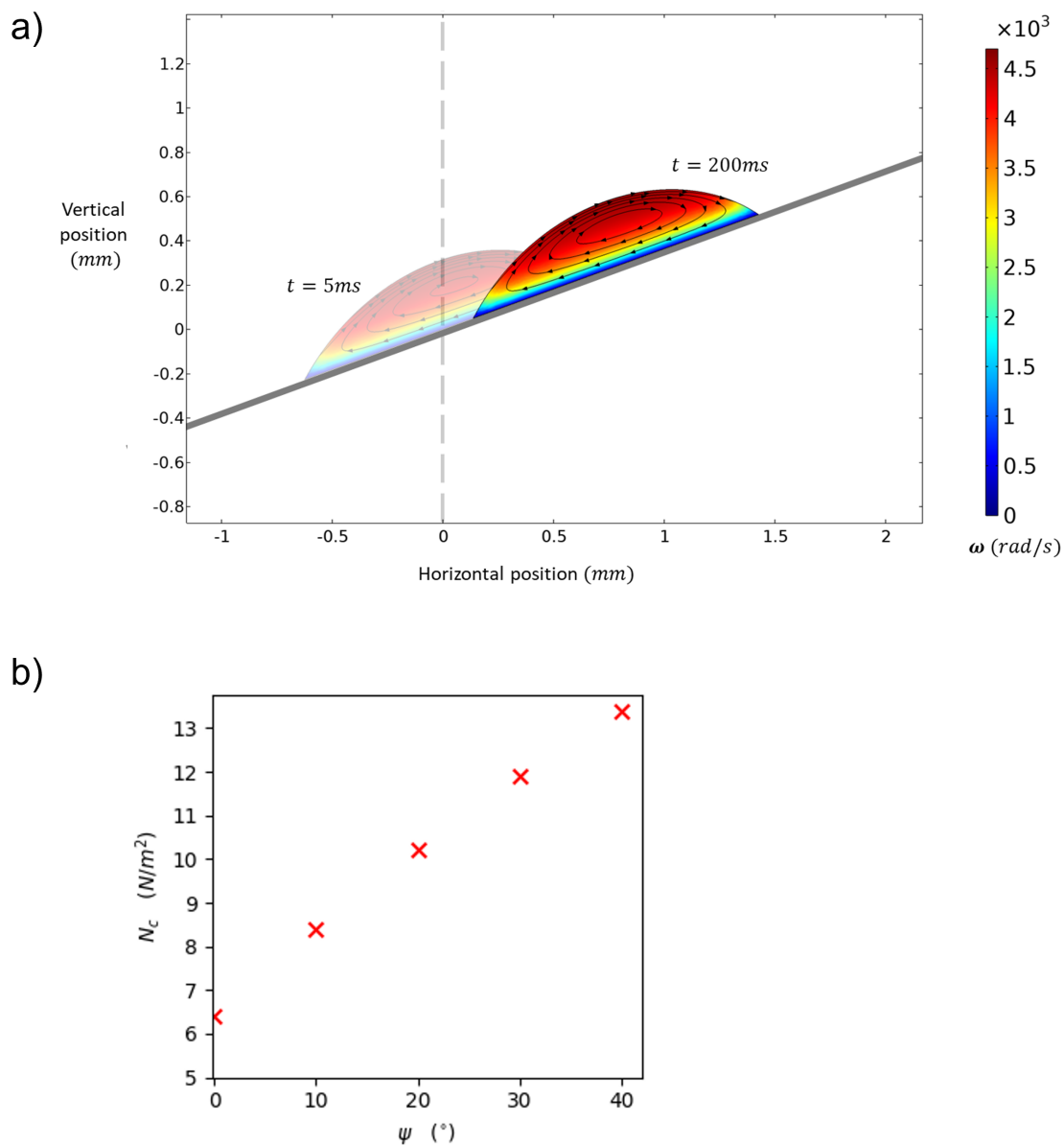
Figure 6.5: Droplet moving up an inclined plane a) Finite element simulation of a droplet climbing an inclined plane ($\psi = 20°$) moving against the gravity at two different times. The colors plot the particle angular velocity in rad/s. b) Plot of the critical magnetic torque density N_c as a function of increasing inclination angle ψ of the substrate. The contact angle hysteresis used here is $\Delta \bar{\theta} = 6°$.

6.8 Discussion

In this article we demonstrated the effectiveness of a magnetic torque in a liquid endowed with rotational degrees of freedom to drive the migration of liquid droplets: the collective particle rotation at the droplet free surface acting as a surface shear, can overcome droplet hysteresis effects and lead to their migration even in the presence of opposing external fields. A three-dimensional counterpart of the present framework could in principle be employed to capture the essence of these effects. This is beyond the scope of the present article however.

Although the effect discussed in the present article has definite possible applications in industry (cf Fig. 6.1) its inspiration originates from medicine. In particular, it is based on the observation that, targeting malignant cells with nanoparticles has proven elusive: recent research showed that only 1% of these particles reach their target [165]. The ramifications of this failure include poor translation of nanotechnology to humans, increased costs and toxicity, and declining therapeutic efficacy. To digress away from the 1% targeting threshold it is imperative that new and unconventional mechanisms of locomotion are invented. Thus, our work in the present article should be considered as a precursor to the development of future targeting-specific locomotion strategies.

CHAPTER 7

CONCLUDING REMARKS

Living organisms are complex systems that actively take energy from the environment and use it to perform a magnitude of complex functions such as sensing, navigation, transport, self healing, reproduction etc. Design of materials that mimic such remarkable properties of biological matter remains an important scientific challenge. Active soft materials that mimic properties of living matter can inspire the creation of 'smart' materials that can sense their environment and respond to them. The aim of this research is to study, design and model such responsive materials.

In this work, we looked at systems that respond to various external signals and fields. We modeled spiropyran-NIPAM hydrogel system that is *photo-responsive* and using the elastic properties of these gels, we designed photo-responsive two-dimensional sheets that can fold into three-dimensional structure upon light radiation (chapter 2). The work presented here can be expanded upon by looking into the design of composite structures formed using different types of photo-responsive gels. For instance, in order to create both mountain and valley folds in the structures presented in chapter 2, we need to have separate light sources on each side of the material that can limit their applications considerably. Using different types of photo-responsive hydrogels can remove such limitations. For example, Spiropyran-NIPAM gel which shrinks in response to light can be replaced with 'swelling' photo-responsive hydrogels [3] and the structure made with the 'swelling' gels will fold away from the light instead of folding towards the light source. Exploring design options with different types of photo-responsive hydrogels can lead to some interesting possibilities.

In chapter 3, we modeled the dynamic behaviour of *chemo-responsive* hydrogel shells that

undergo morphological changes induced by chemical reactions. The chemical reactions trigger changes in the material's hydrophilicity causing the surrounding water to diffuse in and out of the shell's surface. This leads to the changes in its morphology. In the work presented in chapter 3, we modelled this process of water diffusion by means of a damping coefficient in the time evolution equations of the shell. The damping models the time delay between the reaction processes and the morphological changes induced by water diffusion. A possible extension of this work would be to explicitly model the process of water diffusion and derive the 'damping coefficient' from more basic principles.

In chapters 4 and 5, we modeled two different soft robotic systems i.e. a walking robot and a swimming robot respectively. These robots were created using a material that is both *photo* and *magneto-responsive*. These chapters truly highlight the importance of 'smart' materials as we show that the motion in these magnetically actuated robots can change in response to light. These robots alter their dynamic behavior such as speed and direction of motion as their hydrogel bodies sense and respond to external light. Such systems could be used as standalone robotic systems with possible applications discussed in the respective chapters or in conjunction with a more complex system where these dual responsive hydrogels play their respective roles as smart actuators.

In chapter 6, we studied another class of active matter system which exists in a liquid phase as opposed to the elastic hydrogels. The microscopic magnetic particles inside a ferrofluid droplet respond to external magnetic fields and their coupled motion with the surrounding fluid causes these droplets to migrate. The understanding of the motion of these ferrofluid droplets and their dependence on the external magnetic fields can allow us to program their motion and explore applications in the future where specific targeting is required.

The continuum models and the finite element techniques developed in this work allow for a deeper understanding of these active systems. This can help us design and engineer more advanced

and versatile materials that can perform complex functions by actively altering their internal properties. Such materials will be play a key role in the development of smart and intelligent devices in the future and our theoretical understanding of their underlying physics can help drive their development.

REFERENCES

[1] Y. Zhao, C. Xuan, X. Qian, Y. Alsaid, M. Hua, L. Jin, and X. He, "Soft phototactic swimmer based on self-sustained hydrogel oscillator," *Science robotics*, vol. 4, no. 33, eaax7112, 2019.

[2] W. Francis, A. Dunne, C. Delaney, L. Florea, and D. Diamond, "Spiropyran based hydrogels actuators—walking in the light," *Sensors and Actuators B: Chemical*, vol. 250, pp. 608–616, 2017.

[3] C. Li, A. Iscen, L. C. Palmer, G. C. Schatz, and S. I. Stupp, "Light-driven expansion of spiropyran hydrogels," *Journal of the American Chemical Society*, vol. 142, no. 18, pp. 8447–8453, 2020.

[4] Y. S. Kim, M. Liu, Y. Ishida, Y. Ebina, M. Osada, T. Sasaki, T. Hikima, M. Takata, and T. Aida, "Thermoresponsive actuation enabled by permittivity switching in an electrostatically anisotropic hydrogel," *Nature materials*, vol. 14, no. 10, pp. 1002–1007, 2015.

[5] W. Hu, G. Z. Lum, M. Mastrangeli, and M. Sitti, "Small-scale soft-bodied robot with multimodal locomotion," *Nature*, vol. 554, no. 7690, pp. 81–85, 2018.

[6] C. Li, G. C. Lau, H. Yuan, A. Aggarwal, V. L. Dominguez, S. Liu, H. Sai, L. C. Palmer, N. A. Sather, T. J. Pearson, *et al.*, "Fast and programmable locomotion of hydrogel-metal hybrids under light and magnetic fields," *Science robotics*, vol. 5, no. 49, eabb9822, 2020.

[7] S. Li, D. A. Matoz-Fernandez, A. Aggarwal, and M. O. de la Cruz, "Chemically controlled pattern formation in self-oscillating elastic shells," *Proceedings of the National Academy of Sciences*, vol. 118, no. 10, 2021.

[8] S. Maeda, Y. Hara, T. Sakai, R. Yoshida, and S. Hashimoto, "Self-walking gel," *Advanced Materials*, vol. 19, no. 21, pp. 3480–3484, 2007.

[9] W. M. Lai, D. Rubin, and E. Krempl, in *Introduction to Continuum Mechanics (Fourth Edition)*, W. M. Lai, D. Rubin, and E. Krempl, Eds., Fourth Edition, Boston: Butterworth-Heinemann, 2010, ISBN: 978-0-7506-8560-3.

[10] E. M. Lifshitz, A. M. Kosevich, and L. P. Pitaevskii, in *Theory of Elasticity (Third Edition)*, E. M. Lifshitz, A. M. Kosevich, and L. P. Pitaevskii, Eds., Third Edition, Oxford: Butterworth-Heinemann, 1986, ISBN: 978-0-08-057069-3.

[11] M. Rubinstein and R. Colby, *Polymer Physics*. Oxford University Press, 2003.

[12] M. Doi, "Gel dynamics," *Journal of the Physical Society of Japan*, vol. 78, no. 5, p. 052 001, 2009.

[13] M. Doi, *Introduction to polymer physics*. Oxford university press, 1996.

[14] *Comsol multiphysics*, version 5.6, COMSOL AB, Stockholm, Sweden.

[15] *Structural mechanics module user's guide*, v. 5.3, COMSOL Multiphysics®, COMSOL AB, Stockholm, Sweden, 2017.

[16] A. Aggarwal, C. Li, S. I. Stupp, and M. Olvera de la Cruz, "Controlling the shape morphology of origami-inspired photoresponsive hydrogels," *Soft Matter*, vol. 18, pp. 2193–2202, 11 2022.

[17] J. Bae, J. Park, S. Kim, H. Cho, H. J. Kim, S. Park, and D.-S. Shin, "Tailored hydrogels for biosensor applications," *Journal of Industrial and Engineering Chemistry*, vol. 89, pp. 1–12, 2020.

[18] J. Li and D. J. Mooney, "Designing hydrogels for controlled drug delivery," *Nature Reviews Materials*, vol. 1, no. 12, pp. 1–17, 2016.

[19] C. L. Bayer and N. A. Peppas, "Advances in recognitive, conductive and responsive delivery systems," *Journal of Controlled Release*, vol. 132, no. 3, pp. 216–221, 2008.

[20] Y.-C. Cheng, H.-C. Lu, X. Lee, H. Zeng, and A. Priimagi, "Kirigami-based light-induced shape-morphing and locomotion," *Advanced Materials*, vol. 32, no. 7, p. 1 906 233, 2020.

[21] Y. Kim, H. Yuk, R. Zhao, S. A. Chester, and X. Zhao, "Printing ferromagnetic domains for untethered fast-transforming soft materials," *Nature*, vol. 558, no. 7709, pp. 274–279, 2018.

[22] A. H. Gelebart, D. Jan Mulder, M. Varga, A. Konya, G. Vantomme, E. Meijer, R. L. Selinger, and D. J. Broer, "Making waves in a photoactive polymer film," *Nature*, vol. 546, no. 7660, pp. 632–636, 2017.

[23] R. Klajn, "Spiropyran-based dynamic materials," *Chemical Society Reviews*, vol. 43, no. 1, pp. 148–184, 2014.

[24] J. Chen, F. K.-C. Leung, M. C. Stuart, T. Kajitani, T. Fukushima, E. van der Giessen, and B. L. Feringa, "Artificial muscle-like function from hierarchical supramolecular assembly of photoresponsive molecular motors," *Nature chemistry*, vol. 10, no. 2, pp. 132–138, 2018.

[25] F. K.-C. Leung, T. Kajitani, M. C. Stuart, T. Fukushima, and B. L. Feringa, "Dual-controlled macroscopic motions in a supramolecular hierarchical assembly of motor amphiphiles," *Angewandte Chemie International Edition*, vol. 58, no. 32, pp. 10 985–10 989, 2019.

[26] K. Miura, "Method of packaging and deployment of large membranes in space," *The Institute of Space and Astronautical Science report*, no. 618, pp. 1–9, 1985.

[27] K. Kuribayashi, K. Tsuchiya, Z. You, D. Tomus, M. Umemoto, T. Ito, and M. Sasaki, "Self-deployable origami stent grafts as a biomedical application of ni-rich tini shape memory alloy foil," *Materials Science and Engineering: A*, vol. 419, no. 1-2, pp. 131–137, 2006.

[28] S. Li, D. M. Vogt, D. Rus, and R. J. Wood, "Fluid-driven origami-inspired artificial muscles," *Proceedings of the National academy of Sciences*, vol. 114, no. 50, pp. 13 132–13 137, 2017.

[29] M. Schenk and S. D. Guest, "Geometry of miura-folded metamaterials," *Proceedings of the National Academy of Sciences*, vol. 110, no. 9, pp. 3276–3281, 2013.

[30] Z. Y. Wei, Z. V. Guo, L. Dudte, H. Y. Liang, and L. Mahadevan, "Geometric mechanics of periodic pleated origami," *Physical review letters*, vol. 110, no. 21, p. 215 501, 2013.

[31] S. Mueller, B. Kruck, and P. Baudisch, "Laserorigami: Laser-cutting 3d objects," in *Proceedings of the SIGCHI Conference on Human Factors in Computing Systems*, 2013, pp. 2585–2592.

[32] S. Miyashita, S. Guitron, S. Li, and D. Rus, "Robotic metamorphosis by origami exoskeletons," *Science Robotics*, vol. 2, no. 10, eaao4369, 2017.

[33] E. Hawkes, B. An, N. M. Benbernou, H. Tanaka, S. Kim, E. D. Demaine, D. Rus, and R. J. Wood, "Programmable matter by folding," *Proceedings of the National Academy of Sciences*, vol. 107, no. 28, pp. 12 441–12 445, 2010.

[34] J. Li, H. Godaba, Z. Zhang, C. Foo, and J. Zhu, "A soft active origami robot," *Extreme Mechanics Letters*, vol. 24, pp. 30–37, 2018.

[35] J.-H. Na, A. A. Evans, J. Bae, M. C. Chiappelli, C. D. Santangelo, R. J. Lang, T. C. Hull, and R. C. Hayward, "Programming reversibly self-folding origami with micropatterned photo-crosslinkable polymer trilayers," *Advanced Materials*, vol. 27, no. 1, pp. 79–85, 2015.

[36] Y. Chen, J. Yang, X. Zhang, Y. Feng, H. Zeng, L. Wang, and W. Feng, "Light-driven bimorph soft actuators: Design, fabrication, and properties," *Materials Horizons*, vol. 8, no. 3, pp. 728–757, 2021.

[37] N. Bassik, G. M. Stern, and D. H. Gracias, "Microassembly based on hands free origami with bidirectional curvature," *Applied physics letters*, vol. 95, no. 9, p. 091 901, 2009.

[38] C. Li, Y. Xue, M. Han, L. C. Palmer, J. A. Rogers, Y. Huang, and S. I. Stupp, "Synergistic photoactuation of bilayered spiropyran hydrogels for predictable origami-like shape change," *Matter*, vol. 4, no. 4, pp. 1377–1390, 2021.

[39] C. Li, A. Iscen, H. Sai, K. Sato, N. A. Sather, S. M. Chin, Z. Álvarez, L. C. Palmer, G. C. Schatz, and S. I. Stupp, "Supramolecular–covalent hybrid polymers for light-activated mechanical actuation," *Nature materials*, vol. 19, no. 8, pp. 900–909, 2020.

[40] M. Dehghany, H. Zhang, R. Naghdabadi, and Y. Hu, "A thermodynamically-consistent large deformation theory coupling photochemical reaction and electrochemistry for light-responsive gels," *Journal of the Mechanics and Physics of Solids*, vol. 116, pp. 239–266, 2018.

[41] O. Kuksenok and A. C. Balazs, "Modeling the photoinduced reconfiguration and directed motion of polymer gels," *Advanced Functional Materials*, vol. 23, no. 36, pp. 4601–4610, 2013.

[42] Y. Xiong and O. Kuksenok, "Mechanical adaptability of patterns in constrained hydrogel membranes," *Langmuir*, vol. 37, no. 16, pp. 4900–4912, 2021.

[43] G. V. Kolmakov, K. Matyjaszewski, and A. C. Balazs, "Harnessing labile bonds between nanogel particles to create self-healing materials," *ACS nano*, vol. 3, no. 4, pp. 885–892, 2009.

[44] E. B. Stukalin, L.-H. Cai, N. A. Kumar, L. Leibler, and M. Rubinstein, "Self-healing of unentangled polymer networks with reversible bonds," *Macromolecules*, vol. 46, no. 18, pp. 7525–7541, 2013.

[45] A. Chortos, J. Liu, and Z. Bao, "Pursuing prosthetic electronic skin," *Nature materials*, vol. 15, no. 9, pp. 937–950, 2016.

[46] O. Kuksenok, P. Dayal, A. Bhattacharya, V. V. Yashin, D. Deb, I. C. Chen, K. J. Van Vliet, and A. C. Balazs, "Chemo-responsive, self-oscillating gels that undergo biomimetic communication," *Chemical Society Reviews*, vol. 42, no. 17, pp. 7257–7277, 2013.

[47] V. V. Yashin and A. C. Balazs, "Pattern formation and shape changes in self-oscillating polymer gels," *Science*, vol. 314, no. 5800, pp. 798–801, 2006.

[48] V. V. Yashin and A. C. Balazs, "Theoretical and computational modeling of self-oscillating polymer gels," *The Journal of chemical physics*, vol. 126, no. 12, p. 124 707, 2007.

[49] O. Kuksenok, V. V. Yashin, and A. C. Balazs, "Three-dimensional model for chemoresponsive polymer gels undergoing the belousov-zhabotinsky reaction," *Physical Review E*, vol. 78, no. 4, p. 041 406, 2008.

[50] R. Yoshida, E. Kokufuta, and T. Yamaguchi, "Beating polymer gels coupled with a nonlinear chemical reaction," *Chaos: An Interdisciplinary Journal of Nonlinear Science*, vol. 9, no. 2, pp. 260–266, 1999.

[51] K. Miyakawa, F. Sakamoto, R. Yoshida, E. Kokufuta, and T. Yamaguchi, "Chemical waves in self-oscillating gels," *Physical Review E*, vol. 62, no. 1, p. 793, 2000.

[52] P. Techawanitchai, M. Ebara, N. Idota, T.-A. Asoh, A. Kikuchi, and T. Aoyagi, "Photoswitchable control of ph-responsive actuators via ph jump reaction," *Soft Matter*, vol. 8, pp. 2844–2851, 10 2012.

[53] M. Wehner, R. L. Truby, D. J. Fitzgerald, B. Mosadegh, G. M. Whitesides, J. A. Lewis, and R. J. Wood, "An integrated design and fabrication strategy for entirely soft, autonomous robots," *Nature*, vol. 536, no. 7617, pp. 451–455, 2016.

[54] J. Duan, X. Liang, K. Zhu, J. Guo, and L. Zhang, "Bilayer hydrogel actuators with tight interfacial adhesion fully constructed from natural polysaccharides," *Soft Matter*, vol. 13, pp. 345–354, 2 2017.

[55] R. Yoshida, T. Takahashi, T. Yamaguchi, and H. Ichijo, "Self-oscillating gel," *Journal of the American Chemical Society*, vol. 118, no. 21, pp. 5134–5135, 1996.

[56] R. Tamate, T. Ueki, and R. Yoshida, "Self-beating artificial cells: Design of cross-linked polymersomes showing self-oscillating motion," *Advanced Materials*, vol. 27, no. 5, pp. 837–842, 2015.

[57] C. J. Crook, A. Smith, R. A. Jones, and A. J. Ryan, "Chemically induced oscillations in a ph-responsive hydrogel," *Physical Chemistry Chemical Physics*, vol. 4, no. 8, pp. 1367–1369, 2002.

[58] V. Labrot, P. De Kepper, J. Boissonade, I. Szalai, and F. Gauffre, "Wave patterns driven by chemomechanical instabilities in responsive gels," *The Journal of Physical Chemistry B*, vol. 109, no. 46, pp. 21 476–21 480, 2005.

[59] Y. Zhang, N. Zhou, S. Akella, Y. Kuang, D. Kim, A. Schwartz, M. Bezpalko, B. M. Foxman, S. Fraden, I. R. Epstein, *et al.*, "Active cross-linkers that lead to active gels," *Angewandte Chemie*, vol. 125, no. 44, pp. 11 708–11 712, 2013.

[60] K. Huang and I. Szleifer, "Design of multifunctional nanogate in response to multiple external stimuli using amphiphilic diblock copolymer," *Journal of the American Chemical Society*, vol. 139, no. 18, pp. 6422–6430, 2017.

[61] M. Mercker, F. Brinkmann, A. Marciniak-Czochra, and T. Richter, "Beyond turing: Mechanochemical pattern formation in biological tissues," *Biology direct*, vol. 11, no. 1, pp. 1–15, 2016.

[62] A. Mietke, F. Jülicher, and I. F. Sbalzarini, "Self-organized shape dynamics of active surfaces," *Proceedings of the National Academy of Sciences*, vol. 116, no. 1, pp. 29–34, 2019.

[63] A. Sampathkumar, "Mechanical feedback-loop regulation of morphogenesis in plants," *Development*, vol. 147, no. 16, 2020.

[64] G. Vernizzi, R. Sknepnek, and M. O. de la Cruz, "Platonic and archimedean geometries in multicomponent elastic membranes," *Proceedings of the National Academy of Sciences*, vol. 108, no. 11, pp. 4292–4296, 2011.

[65] Y. Klein, E. Efrati, and E. Sharon, "Shaping of elastic sheets by prescription of non-euclidean metrics," *Science*, vol. 315, no. 5815, pp. 1116–1120, 2007. eprint: `https://science.sciencemag.org/content/315/5815/1116.full.pdf`.

[66] D. Matoz-Fernandez, F. A. Davidson, N. R. Stanley-Wall, and R. Sknepnek, "Wrinkle patterns in active viscoelastic thin sheets," *Physical Review Research*, vol. 2, no. 1, p. 013 165, 2020.

[67] W. Koiter, "On the nonlinear theory of thin elastic shells. i- introductory sections. ii- basic shell equations. iii- simplified shell equations(nonlinear theory of thin elastic shells, discussing surface geometry and deformation, equations of equilibrium and boundary conditions and stress functions)," *Koninklijke Nederlandse Akademie van Wetenschappen, Proceedings, Series B*, vol. 69, no. 1, pp. 1–54, 1966.

[68] E. Sharon and E. Efrati, "The mechanics of non-Euclidean plates," *Soft Matter*, vol. 6, no. 22, pp. 5693–5704, 2010.

[69] B. Audoly and Y. Pomeau, *Elasticity and Geometry - From Hair Curls to the Non-linear Response of Shells*. Oxford University Press, Oxford, UK, 2010.

[70] G. R. Argento, S. Gabriele, L. Teresi, and V. Varano, "Target metric and shell shaping," *Curved and Layered Structures*, vol. 8, no. 1, pp. 13–25, 2021.

[71] E. Efrati, E. Sharon, and R. Kupferman, "Elastic theory of unconstrained non-euclidean plates," *J. Mech. Phys. Solids*, vol. 57, no. 4, pp. 762–775, 2009.

[72] P. Ball and N. R. Borley, *The self-made tapestry: pattern formation in nature*. Oxford University Press Oxford, 1999, vol. 198.

[73] S. Kondo and T. Miura, "Reaction-diffusion model as a framework for understanding biological pattern formation," *science*, vol. 329, no. 5999, pp. 1616–1620, 2010.

[74] J. Alonso-Mora, A. Breitenmoser, M. Rufli, R. Siegwart, and P. Beardsley, "Multi-robot system for artistic pattern formation," in *2011 IEEE international conference on robotics and automation*, IEEE, 2011, pp. 4512–4517.

[75] Y.-Y. Xiao, Z.-C. Jiang, X. Tong, and Y. Zhao, "Biomimetic locomotion of electrically powered "janus" soft robots using a liquid crystal polymer," *Advanced Materials*, vol. 31, no. 36, p. 1 903 452, 2019.

[76] A. N. Landge, B. M. Jordan, X. Diego, and P. Müller, "Pattern formation mechanisms of self-organizing reaction-diffusion systems," *Developmental Biology*, vol. 460, no. 1, pp. 2–11, 2020.

[77] L. Wolpert, "Positional information and the spatial pattern of cellular differentiation," *Journal of Theoretical Biology*, vol. 25, no. 1, pp. 1–47, 1969.

[78] A. Zaikin and A. Zhabotinsky, "Concentration wave propagation in two-dimensional liquid-phase self-oscillating system," *Nature*, vol. 225, no. 5232, pp. 535–537, 1970.

[79] R. J. Field and R. M. Noyes, "Oscillations in chemical systems. iv. limit cycle behavior in a model of a real chemical reaction," *The Journal of Chemical Physics*, vol. 60, no. 5, pp. 1877–1884, 1974.

[80] J. J. Tyson and P. C. Fife, "Target patterns in a realistic model of the belousov–zhabotinskii reaction," *The Journal of Chemical Physics*, vol. 73, no. 5, pp. 2224–2237, 1980.

[81] R. Yoshida, S. Onodera, T. Yamaguchi, and E. Kokufuta, "Aspects of the belousov- zhabotinsky reaction in polymer gels," *The Journal of Physical Chemistry A*, vol. 103, no. 43, pp. 8573–8578, 1999.

[82] C. Quilliet, "Numerical deflation of beach balls with various poisson's ratios: From sphere to bowl's shape," *The European Physical Journal E*, vol. 35, no. 6, pp. 1–9, 2012.

[83] I. Nitsan, S. Drori, Y. E. Lewis, S. Cohen, and S. Tzlil, "Mechanical communication in cardiac cell synchronized beating," *Nature Physics*, vol. 12, no. 5, pp. 472–477, 2016.

[84] O. Cohen and S. A. Safran, "Cardiomyocyte calcium ion oscillations—lessons from physics," *Frontiers in Physiology*, vol. 11, 2020.

[85] R. Tamate, T. Ueki, and R. Yoshida, "Evolved colloidosomes undergoing cell-like autonomous shape oscillations with buckling," *Angewandte Chemie*, vol. 128, no. 17, pp. 5265–5269, 2016.

[86] M. Gage, R. S. Hamilton, *et al.*, "The heat equation shrinking convex plane curves," *Journal of Differential Geometry*, vol. 23, no. 1, pp. 69–96, 1986.

[87] Y. Zhang, N. Li, J. Delgado, N. Zhou, R. Yoshida, S. Fraden, I. R. Epstein, and B. Xu, "Structural modulation of self-oscillating gels: Changing the proximity of the catalyst to the polymer backbone to tailor chemomechanical oscillation," *Soft Matter*, vol. 8, no. 26, pp. 7056–7061, 2012.

[88] J. Herterich, I. Griffiths, and D. Vella, "Reproducing the pressure–time signature of membrane filtration: The interplay between fouling, caking, and elasticity," *Journal of Membrane Science*, vol. 577, pp. 235–248, 2019.

[89] P. W. Miller, N. Stoop, and J. Dunkel, "Geometry of wave propagation on active deformable surfaces," *Physical review letters*, vol. 120, no. 26, p. 268 001, 2018.

[90] I. Levin, R. Deegan, and E. Sharon, "Self-oscillating membranes: Chemomechanical sheets show autonomous periodic shape transformation," *Physical Review Letters*, vol. 125, no. 17, p. 178 001, 2020.

[91] O. Kuksenok, V. V. Yashin, and A. C. Balazs, "Global signaling of localized impact in chemo-responsive gels," *Soft Matter*, vol. 5, no. 9, pp. 1835–1839, 2009.

[92] O. Kuksenok, V. V. Yashin, and A. C. Balazs, "Mechanically induced chemical oscillations and motion in responsive gels," *Soft Matter*, vol. 3, no. 9, pp. 1138–1144, 2007.

[93] I. C. Chen, O. Kuksenok, V. V. Yashin, A. C. Balazs, and K. J. Van Vliet, "Mechanical resuscitation of chemical oscillations in belousov–zhabotinsky gels," *Advanced Functional Materials*, vol. 22, no. 12, pp. 2535–2541, 2012.

[94] K. Suzuki, T. Yoshinobu, and H. Iwasaki, "Induction of chemical waves by mechanical stimulation in elastic belousov-zhabotinsky media," *Chemical Physics Letters*, vol. 349, no. 5, pp. 437–441, 2001.

[95] R. Sknepnek, G. Vernizzi, and M. O. de La Cruz, "Shape change of nanocontainers via a reversible ionic buckling," *Physical review letters*, vol. 106, no. 21, p. 215 504, 2011.

[96] C.-Y. Leung, L. C. Palmer, B. F. Qiao, S. Kewalramani, R. Sknepnek, C. J. Newcomb, M. A. Greenfield, G. Vernizzi, S. I. Stupp, M. J. Bedzyk, *et al.*, "Molecular crystallization controlled by ph regulates mesoscopic membrane morphology," *ACS nano*, vol. 6, no. 12, pp. 10 901–10 909, 2012.

[97] R. J. Field, E. Koros, and R. M. Noyes, "Oscillations in chemical systems. ii. thorough analysis of temporal oscillation in the bromate-cerium-malonic acid system," *Journal of the American Chemical Society*, vol. 94, no. 25, pp. 8649–8664, 1972.

[98] R. J. Field and H. D. Foersterling, "On the oxybromine chemistry rate constants with cerium ions in the field-koeroes-noyes mechanism of the belousov-zhabotinskii reaction:

The equilibrium hbro2+ bro3-+ h+. dblharw. 2bro. ovrhdot. 2+ h2o," *The Journal of Physical Chemistry*, vol. 90, no. 21, pp. 5400–5407, 1986.

[99] C. Gray, "An analysis of the belousov-zhabotinskii reaction," *Rose-Hulman Undergraduate Mathematics Journal*, vol. 3, no. 1, p. 1, 2002.

[100] T. Kohyama, D. Kroll, and G. Gompper, "Budding of crystalline domains in fluid membranes," *Physical Review E*, vol. 68, no. 6, p. 061 905, 2003.

[101] I. Nitschke, S. Reuther, and A. Voigt, "Discrete exterior calculus (dec) for the surface navier-stokes equation," in *Transport Processes at Fluidic Interfaces*, D. Bothe and A. Reusken, Eds. Cham: Springer International Publishing, 2017, pp. 177–197, ISBN: 978-3-319-56602-3.

[102] J. Lefèvre and J.-F. Mangin, "A reaction-diffusion model of human brain development," *PLoS Comput Biol*, vol. 6, no. 4, e1000749, 2010.

[103] S.-J. Park, M. Gazzola, K. S. Park, S. Park, V. Di Santo, E. L. Blevins, J. U. Lind, P. H. Campbell, S. Dauth, A. K. Capulli, *et al.*, "Phototactic guidance of a tissue-engineered soft-robotic ray," *Science*, vol. 353, no. 6295, pp. 158–162, 2016.

[104] A. S. Weingarten, R. V. Kazantsev, L. C. Palmer, M. McClendon, A. R. Koltonow, A. P. Samuel, D. J. Kiebala, M. R. Wasielewski, and S. I. Stupp, "Self-assembling hydrogel scaffolds for photocatalytic hydrogen production," *Nature chemistry*, vol. 6, no. 11, pp. 964–970, 2014.

[105] H. Yang, B. S. Yeow, Z. Li, K. Li, T.-H. Chang, L. Jing, Y. Li, J. S. Ho, H. Ren, and P.-Y. Chen, "Multifunctional metallic backbones for origami robotics with strain sensing and wireless communication capabilities," *Science Robotics*, vol. 4, no. 33, eaax7020, 2019.

[106] R. Dreyfus, J. Baudry, M. L. Roper, M. Fermigier, H. A. Stone, and J. Bibette, "Microscopic artificial swimmers," *Nature*, vol. 437, no. 7060, pp. 862–865, 2005.

[107] J. M. Dempster, P. Vázquez-Montejo, and M. O. De La Cruz, "Contractile actuation and dynamical gel assembly of paramagnetic filaments in fast precessing fields," *Physical Review E*, vol. 95, no. 5, p. 052 606, 2017.

[108] J. Cui, T.-Y. Huang, Z. Luo, P. Testa, H. Gu, X.-Z. Chen, B. J. Nelson, and L. J. Heyderman, "Nanomagnetic encoding of shape-morphing micromachines," *Nature*, vol. 575, no. 7781, pp. 164–168, 2019.

[109] Y. Kim, G. A. Parada, S. Liu, and X. Zhao, "Ferromagnetic soft continuum robots," *Science Robotics*, vol. 4, no. 33, eaax7329, 2019.

[110] T. Xu, J. Zhang, M. Salehizadeh, O. Onaizah, and E. Diller, "Millimeter-scale flexible robots with programmable three-dimensional magnetization and motions," *Science Robotics*, vol. 4, no. 29, eaav4494, 2019.

[111] J. A.-C. Liu, J. H. Gillen, S. R. Mishra, B. A. Evans, and J. B. Tracy, "Photothermally and magnetically controlled reconfiguration of polymer composites for soft robotics," *Science advances*, vol. 5, no. 8, eaaw2897, 2019.

[112] L. Ionov, "Hydrogel-based actuators: Possibilities and limitations," *Materials Today*, vol. 17, no. 10, pp. 494–503, 2014.

[113] D. Han, C. Farino, C. Yang, T. Scott, D. Browe, W. Choi, J. W. Freeman, and H. Lee, "Soft robotic manipulation and locomotion with a 3d printed electroactive hydrogel," *ACS applied materials & interfaces*, vol. 10, no. 21, pp. 17 512–17 518, 2018.

[114] A. Mourran, H. Zhang, R. Vinokur, and M. Möller, "Soft microrobots employing nonequilibrium actuation via plasmonic heating," *Advanced Materials*, vol. 29, no. 2, p. 1 604 825, 2017.

[115] I. K. Han, T. Chung, J. Han, and Y. S. Kim, "Nanocomposite hydrogel actuators hybridized with various dimensional nanomaterials for stimuli responsiveness enhancement," *Nano Convergence*, vol. 6, no. 1, pp. 1–21, 2019.

[116] T. Caykara, D. Yörük, and S. Demirci, "Preparation and characterization of poly (n-tert-butylacrylamide-co-acrylamide) ferrogel," *Journal of Applied Polymer Science*, vol. 112, no. 2, pp. 800–804, 2009.

[117] J. Tang, Z. Tong, Y. Xia, M. Liu, Z. Lv, Y. Gao, T. Lu, S. Xie, Y. Pei, D. Fang, *et al.*, "Super tough magnetic hydrogels for remotely triggered shape morphing," *Journal of Materials Chemistry B*, vol. 6, no. 18, pp. 2713–2722, 2018.

[118] Q. Li, A. P. Schenning, and T. J. Bunning, *Light-responsive smart soft matter technologies*, 2019.

[119] M.-M. Russew and S. Hecht, "Photoswitches: From molecules to materials," *Advanced Materials*, vol. 22, no. 31, pp. 3348–3360, 2010.

[120] B. Gao, L. Qiao, J. Wang, Q. Liu, F. Li, J. Feng, and D. Xue, "Microwave absorption properties of the ni nanowires composite," *Journal of Physics D: Applied Physics*, vol. 41, no. 23, p. 235 005, 2008.

[121] L. Dorfmann and R. W. Ogden, *Nonlinear theory of electroelastic and magnetoelastic interactions*. Springer, 2014, vol. 1.

[122] G. Qiu and T. Pence, "Remarks on the behavior of simple directionally reinforced incompressible nonlinearly elastic solids," *Journal of Elasticity*, vol. 49, no. 1, pp. 1–30, 1997.

[123] F. Lancia, A. Ryabchun, and N. Katsonis, "Life-like motion driven by artificial molecular machines," *Nature Reviews Chemistry*, vol. 3, no. 9, pp. 536–551, 2019.

[124] E. Wang, M. S. Desai, and S.-W. Lee, "Light-controlled graphene-elastin composite hydrogel actuators," *Nano letters*, vol. 13, no. 6, pp. 2826–2830, 2013.

[125] H. Shahsavan, A. Aghakhani, H. Zeng, Y. Guo, Z. S. Davidson, A. Priimagi, and M. Sitti, "Bioinspired underwater locomotion of light-driven liquid crystal gels," *Proceedings of the National Academy of Sciences*, vol. 117, no. 10, pp. 5125–5133, 2020.

[126] B. Behkam and M. Sitti, "Design Methodology for Biomimetic Propulsion of Miniature Swimming Robots," *Journal of Dynamic Systems, Measurement, and Control*, vol. 128, no. 1, pp. 36–43, Sep. 2005.

[127] I. Rehor, C. Maslen, P. G. Moerman, B. G. Van Ravensteijn, R. Van Alst, J. Groenewold, H. B. Eral, and W. K. Kegel, "Photoresponsive hydrogel microcrawlers exploit friction hysteresis to crawl by reciprocal actuation," *Soft Robotics*, vol. 8, no. 1, pp. 10–18, 2021.

[128] O. Sul, M. Falvo, R. Taylor, S. Washburn, and R. Superfine, "Thermally actuated untethered impact-driven locomotive microdevices," *Applied physics letters*, vol. 89, no. 20, p. 203 512, 2006.

[129] D. Morales, E. Palleau, M. D. Dickey, and O. D. Velev, "Electro-actuated hydrogel walkers with dual responsive legs," *Soft matter*, vol. 10, no. 9, pp. 1337–1348, 2014.

[130] B. R. Donald, C. G. Levey, C. D. McGray, I. Paprotny, and D. Rus, "An untethered, electrostatic, globally controllable mems micro-robot," *Journal of microelectromechanical systems*, vol. 15, no. 1, pp. 1–15, 2006.

[131] H. Zeng, P. Wasylczyk, C. Parmeggiani, D. Martella, M. Burresi, and D. S. Wiersma, "Light-fueled microscopic walkers," *Advanced Materials*, vol. 27, no. 26, pp. 3883–3887, 2015.

[132] J. Donea, A. Huerta, J.-P. Ponthot, and A. Rodríguez-Ferran, "Arbitrary lagrangian–eulerian methods," in *Encyclopedia of Computational Mechanics*. John Wiley & Sons, Ltd, 2004, ch. 14.

[133] *Comsol multiphysics reference manual*, v. 5.5, COMSOL Multiphysics®, COMSOL AB, Stockholm, Sweden, 2019.

[134] U. K. Muller, J. G. van den Boogaart, and J. L. van Leeuwen, "Flow patterns of larval fish: Undulatory swimming in the intermediate flow regime," *Journal of Experimental Biology*, vol. 211, no. 2, pp. 196–205, 2008.

[135] S. M. Chin, C. V. Synatschke, S. Liu, R. J. Nap, N. A. Sather, Q. Wang, Z. Álvarez, A. N. Edelbrock, T. Fyrner, L. C. Palmer, *et al.*, "Covalent-supramolecular hybrid polymers as muscle-inspired anisotropic actuators," *Nature communications*, vol. 9, no. 1, pp. 1–11, 2018.

[136] M. Driscoll and B. Delmotte, "Leveraging collective effects in externally driven colloidal suspensions: Experiments and simulations," *Current opinion in colloid & interface science*, vol. 40, pp. 42–57, 2019.

[137] T. Yang, B. Sprinkle, Y. Guo, J. Qian, D. Hua, A. Donev, D. W. Marr, and N. Wu, "Reconfigurable microbots folded from simple colloidal chains," *Proceedings of the National Academy of Sciences*, vol. 117, no. 31, pp. 18 186–18 193, 2020.

[138] I. Torres-Díaz and C. Rinaldi, "Recent progress in ferrofluids research: Novel applications of magnetically controllable and tunable fluids," *Soft matter*, vol. 10, no. 43, pp. 8584–8602, 2014.

[139] W. Wang, J. V. Timonen, A. Carlson, D.-M. Drotlef, C. T. Zhang, S. Kolle, A. Grinthal, T.-S. Wong, B. Hatton, S. H. Kang, *et al.*, "Multifunctional ferrofluid-infused surfaces with reconfigurable multiscale topography," *Nature*, vol. 559, no. 7712, pp. 77–82, 2018.

[140] E. B. Dussan, "On the spreading of liquids on solid surfaces: Static and dynamic contact lines," *Annual Review of Fluid Mechanics*, vol. 11, no. 1, pp. 371–400, 1979.

[141] A. M. Schwartz and S. B. Tejada, "Studies of dynamic contact angles on solids," *Journal of Colloid and Interface Science*, vol. 38, no. 2, pp. 359–375, 1972.

[142] R. L. Hoffman, "A study of the advancing interface. i. interface shape in liquid—gas systems," *Journal of colloid and interface science*, vol. 50, no. 2, pp. 228–241, 1975.

[143] L. Tanner, "The spreading of silicone oil drops on horizontal surfaces," *Journal of Physics D: Applied Physics*, vol. 12, no. 9, p. 1473, 1979.

[144] P. Ehrhard, "Experiments on isothermal and non-isothermal spreading," *Journal of Fluid Mechanics*, vol. 257, pp. 463–483, 1993.

[145] P. Ehrhard and S. H. Davis, "Non-isothermal spreading of liquid drops on horizontal plates," *Journal of Fluid Mechanics*, vol. 229, pp. 365–388, 1991.

[146] C. Ngan *et al.*, "On the dynamics of liquid spreading on solid surfaces," *Journal of Fluid Mechanics*, vol. 209, pp. 191–226, 1989.

[147] P.-G. De Gennes, "Wetting: Statics and dynamics," *Reviews of modern physics*, vol. 57, no. 3, p. 827, 1985.

[148] H. P. Greenspan, "On the motion of a small viscous droplet that wets a surface," *Journal of Fluid Mechanics*, vol. 84, no. 1, pp. 125–143, 1978.

[149] M. K. Smith, "Thermocapillary migration of a two-dimensional liquid droplet on a solid surface," *Journal of Fluid Mechanics*, vol. 294, pp. 209–230, 1995.

[150] M. Davis, M. Gratton, and S. Davis, "Suppressing van der waals driven rupture through shear," *Journal of fluid mechanics*, vol. 661, pp. 522–539, 2010.

[151] J. S. Dahler and L. E. Scriven, "Angular momentum of continua," *Nature*, vol. 192, no. 4797, pp. 36–37, 1961.

[152] D. W. Condiff and J. S. Dahler, "Fluid mechanical aspects of antisymmetric stress," *The Physics of Fluids*, vol. 7, no. 6, pp. 842–854, 1964.

[153] C. Rinaldi, "Continuum modeling of polarizable systems," Ph.D. dissertation, Massachusetts Institute of Technology, 2002.

[154] A. Oron, S. H. Davis, and S. G. Bankoff, "Long-scale evolution of thin liquid films," *Reviews of modern physics*, vol. 69, no. 3, pp. 931–980, 1997.

[155] A. Chaves and C. Rinaldi, "Interfacial stress balances in structured continua and free surface flows in ferrofluids," *Physics of Fluids*, vol. 26, no. 4, p. 042 101, 2014.

[156] E. Kirkinis and S. H. Davis, "Hydrodynamic theory of liquid slippage on a solid substrate near a moving contact line," *Physical Review Letters*, vol. 110, no. 23, p. 234 503, 2013.

[157] E. Kirkinis and S. Davis, "Moffatt vortices induced by the motion of a contact line," *Journal of Fluid Mechanics*, vol. 746, 2014.

[158] C. Rinaldi and M. Zahn, "Effects of spin viscosity on ferrofluid flow profiles in alternating and rotating magnetic fields," *Physics of Fluids*, vol. 14, no. 8, pp. 2847–2870, 2002.

[159] A. Chaves, C. Rinaldi, S. Elborai, X. He, and M. Zahn, "Bulk flow in ferrofluids in a uniform rotating magnetic field," *Physical Review Letters*, vol. 96, no. 19, p. 194 501, 2006.

[160] A. Chaves, M. Zahn, and C. Rinaldi, "Spin-up flow of ferrofluids: Asymptotic theory and experimental measurements," *Physics of Fluids*, vol. 20, no. 5, p. 053 102, 2008.

[161] E. Aero, A. Bulygin, and E. Kuvshinskii, "Asymmetric hydromechanics," *Journal of Applied Mathematics and Mechanics*, vol. 29, no. 2, pp. 333–346, 1965.

[162] E. Lauga, M. Brenner, and H. Stone, "Microfluidics: The no-slip boundary condition," in *Springer Handbook of Experimental Fluid Mechanics*, C. Tropea, A. L. Yarin, and J. F. Foss, Eds. Berlin, Heidelberg: Springer Berlin Heidelberg, 2007, pp. 1219–1240, ISBN: 978-3-540-30299-5.

[163] E. Kirkinis, "Magnetic torque-induced suppression of van-der-waals-driven thin liquid film rupture," *Journal of Fluid Mechanics*, vol. 813, pp. 991–1006, 2017.

[164] Z. Cai and Y. Song, "Implementing contact angle hysteresis in moving mesh-based two-phase flow numerical simulations," *ACS Omega*, vol. 6, no. 51, pp. 35 711–35 717, 2021.

[165] S. Wilhelm, A. J. Tavares, Q. Dai, S. Ohta, J. Audet, H. F. Dvorak, and W. C. Chan, "Analysis of nanoparticle delivery to tumours," *Nature reviews materials*, vol. 1, no. 5, pp. 1–12, 2016.

[166] T. Belytschko, W. K. Liu, B. Moran, and K. Elkhodary, *Nonlinear finite elements for continua and structures*. John wiley & sons, 2014.

APPENDIX A

MAGNETIC SIMULATIONS

We discussed the hyperelastic material model (constitutive relation) of the magneto-elastic materials in chapter 4 section 4.4 i.e.

$$U_{mag} = -\left(\mathbf{FM}\right) \cdot \mathbf{B} \tag{A.1}$$

This results in a magnetically induced stress given by

$$\boldsymbol{\sigma}_{mag} = \frac{1}{J} \frac{\partial U_{mag}}{\partial \mathbf{F}} \mathbf{F}^T \tag{A.2}$$

Solving this equation in index notion we get

$$
\begin{aligned}
(\sigma_{mag})_{ij} &= -J^{-1} \frac{\partial \left(F_{nK} M_K B_n\right)}{\partial F_{iL}} F_{jL} \\
&= -J^{-1} \delta_{in} \delta_{LK} M_K B_n F_{jL} \\
&= -J^{-1} M_K F_{jK} B_i \quad \left(= -\mathbf{B} \otimes \mathbf{FM}/J\right)
\end{aligned} \tag{A.3}
$$

where $\otimes$ is the dyadic/outer product. We can see here that the magnetic stress tensor is not symmetric. Therefore the total stress (elastic stress + magnetic stress) on the material will become asymmetric. This is a problem since we used COMSOL for simulating the hyperelastic solid and COMSOL internally assumes the stress tensor to be symmetric. Therefore in order to simulate this material we used COMSOL's inbuilt hyperelastic module to input the elastic part of the free energy

density (symmetric stress tensor) and used the *weak contribution* functionality to add the magnetic stress as an extra contribution.

Here I will show the derivation of the equation of motion in the weak form. From that, we can separate the weak form of the magnetic stress and input into COMSOL using the weak contribution functionality.

We start by writing the strong form of the equation of motion (eq. 1.17) in index notion

$$\rho_0 \frac{\partial^2 u_i}{\partial t^2} = (f_V)_i + \frac{\partial P_{iJ}}{\partial X_J} \tag{A.4}$$

We use the variation in the functional **u** i.e. δ**u** to write the corresponding weak form as

$$\delta \mathcal{W} = \int_V \left(-\rho_0 \frac{\partial^2 u_i}{\partial t^2} + (f_V)_i + \frac{\partial P_{iJ}}{\partial X_J} \right) \delta u_i dV \tag{A.5}$$

Here, $\delta \mathcal{W}$ is the variation in the virtual work done by the system [166]. Solving the right hand side

$$= \int_V \left(-\rho_0 \frac{\partial^2 u_i}{\partial t^2} \delta u_i + (f_V)_i \delta u_i + \frac{\partial P_{iJ}}{\partial X_J} \delta u_i \right) dV$$

$$= \int_V \left(-\rho_0 \frac{\partial^2 u_i}{\partial t^2} \delta u_i + (f_V)_i \delta u_i + \frac{\partial (P_{iJ} \delta u_i)}{\partial X_J} - P_{iJ} \frac{\partial (\delta u_i)}{\partial X_J} \right) dV$$

$$= \int_V \left(-\rho_0 \frac{\partial^2 u_i}{\partial t^2} \delta u_i + (f_V)_i \delta u_i - P_{iJ} \frac{\partial (\delta u_i)}{\partial X_J} \right) dV + \int_{\partial V} (P_{iJ} \delta u_i) N_J dS$$

$$= \int_V \left(-\rho_0 \frac{\partial^2 u_i}{\partial t^2} \delta u_i + (f_V)_i \delta u_i - P_{iJ} \delta F_{iJ} \right) dV + \int_{\partial V} (f_S)_i \delta u_i dS \tag{A.6}$$

where δF_{iJ} is the variation in the deformation gradient tensor. This derivation does not assume the symmetry of the stress tensor and therefore can be used for any general case. Looking at the

stress term in the weak form eq. A.6 i.e.

$$- \int_V P_{iJ} \delta F_{iJ} dV$$

we can separate out the magnetic stress and therefore write the *weak contribution* due to it as

$$\delta \mathcal{W}_{mag} = - \int_V \delta \mathbf{F} : \mathbf{P}_{mag} dV \tag{A.7}$$

where the symbol ':' denotes contraction over two indices. We can now write the 1st Piola-Kirchhoff stress tensor as

$$\mathbf{P}_{mag} = \frac{\partial U_{mag}}{\partial \mathbf{F}}$$
$$(P_{mag})_{iJ} = -\frac{\partial \left(F_{nK} M_K B_n \right)}{\partial F_{iJ}}$$
$$(P_{mag})_{iJ} = -\delta_{in} \delta_{JK} M_K B_n$$
$$(P_{mag})_{iJ} = -B_i M_J \quad (= -\mathbf{B} \otimes \mathbf{M}) \tag{A.8}$$

Therefore using eqs. A.7 and A.8 we can input the following expression as a weak contribution to the stress for our hyperelastic model.

$$\delta \mathcal{W}_{mag} = - \int_V \sum_{i=x,y,z} \sum_{J=X,Y,Z} test(F_{iJ})(P_{mag})_{iJ} dV \tag{A.9}$$

where the '*test()*' function is COMSOL's inbuilt functional variation operator.